

High Speed Stereovision *in situ* Monitoring of Spatter During Laser Powder Bed Fusion

by

Christopher Barrett

Submitted in Partial Fulfillment of the Requirements

for the Degree of

Doctor of Philosophy

in the

Materials Science & Engineering

Program

YOUNGSTOWN STATE UNIVERSITY

December, 2019

High Speed Stereovision *in situ* Monitoring of Spatter During Laser Powder Bed Fusion

Christopher Barrett

I hereby release this dissertation to the public. I understand that this dissertation will be made available from the OhioLINK ETD Center and the Maag Library Circulation Desk for public access. I also authorize the University or other individuals to make copies of this thesis as needed for scholarly research.

Signature:

Christopher Barrett, Student Date

Approvals:

Brett Conner, Dissertation Advisor Date

Michael Crescimanno, Committee Member Date

Eric Macdonald, Committee Member Date

Virgil Solomon, Committee Member Date

Jason Walker, Committee Member Date

Dr. Salvatore A. Sanders, Dean of Graduate Studies Date

ABSTRACT

Metal laser powder bed fusion (LPBF) Additive Manufacturing (AM) affords new design freedoms for metallic structures with complex geometries. The aerospace industry has identified the inherent benefits of AM not just in terms of shape creation but also with regard to producing replacement parts for an aging fleet of aircraft. However, for these parts to be deployed, the quality must be well established given the lack of heritage for this manufacturing process. As additive manufacturing is executed layerwise, opportunities exist to non-destructively verify the fabrication *in situ* with a qualify-as-you-go methodology. A proposed solution is presented, which utilizes a pair of low cost, high speed cameras that are integrated and synchronized together to provide stereovision in order to identify the size, speed, direction and age of spatter ejected from the laser melt pool. The driving hypothesis of the effort is that the behavior of spatter can be reliably measured in order to determine the health of the laser process and ensure that spatter is not contaminating the build.

Acknowledgement

To my family for their support throughout this process, and the many sacrifices that were made throughout my education over the years. Without that support this pinnacle work would not have been achieved.

I would like to thank the many YSU staff and faculty which have contributed to this work. My sincerest gratitude to my dissertation advisor Dr. Brett Conner. Working under you has provided me significant career opportunities which I am extremely grateful for and eager to expand upon. Thank you for all your time and guidance throughout my doctoral education.

Next, I would like to thank the members of my dissertation committee, Dr. Michael Crescimanno, Dr. Eric Macdonald, Dr. Virgil Solomon, and Dr. Jason Walker. Thank you for your assistance with my dissertation, the publications listed herein, and the time you all spent with me on numerous occasions.

I acknowledge the help received by the Center of Innovation in Additive Manufacturing, the Center for Excellence in Materials Science and Engineering, and the Department of Geological and Environmental Sciences at YSU. I would like to express my gratitude toward Mr. Jeremy McKnight for his continual support with the various LPBF machines and part support issues. Additionally, I would like to thank Dr. Virgil Solomon for his help with the scanning electron microscopy experiments performed during this work and for the many occasions he provided guidance and advice. Furthermore, I would like to thank Dr. Jeffrey Dick for his help with the particle size distribution analysis.

Additionally, I would like to express my appreciation to Griffin Jones at Penn State University for his help with the CT scanning of my samples, and to Westmoreland for the tensile testing.

I would like to thank the Friedman Endowment for Manufacturing at Youngstown State University. This effort was performed in part through the National Center for Defense Manufacturing and Machining under the America Makes Program entitled “Maturation of Advanced Manufacturing for Low Cost Sustainment (MAMLS)” and is based on research sponsored by Air Force Research Laboratory under agreement number FA8650-16-2-5700. The U.S. Government is authorized to reproduce and distribute reprints for Governmental purposes notwithstanding any copyright notation thereon.

List of Acronyms

CAD – Computer Aided Design

PBF – Powder Bed Fusion

LPBF – Laser Powder Bed Fusion

AM – Additive Manufacturing

SEM – Scanning Electron Microscope

EDS – Electron Dispersive Spectroscopy

BSE – Back Scatter Electron

FPS – Frames Per Second

NDE – Nondestructive Examination

AlSi10Mg – Aluminum 10 Silicon Magnesium

SS 316L – Stainless Steel 316 L

IN 718 – Inconel 718

HIP – Hot Isostatic Press

μm – Micron

FWHM – Full Width Half Maximum

mm – Millimeter

Table of Contents

ABSTRACT	iii
Acknowledgement	iv
List of Acronyms	vi
List of Figures	x
List of Tables	xii
1.0 Introductory	1
1.1 Powder Bed Fusion	1
1.2 Laser Powder Bed Fusion	2
1.2.1 M-LPBF Build Parameters	2
1.2.1 M-LPBF Melt Pool Characteristics	7
1.2.2 M-LPBF Microstructure Characteristics	10
1.2.3 M-LPBF Defects	13
1.2.4 Spatter Generation and Defect Causation	14
1.2.5 Post Processing	16
1.3 <i>In Situ</i> Monitoring	17
1.3.1 High Speed Monitoring	18
1.4 Research Questions and Hypothesis	19
2.0 Background Studies	21
2.1 Spatter Impact Experiment	21
2.1.1 Particle Size Distribution Determination	22
2.1.2 Scanning Electron Microscope Analysis of Spatter	24
2.1.3 Optical Microscopy and CT Analysis	27
2.1.4 Mechanical Testing Results	29
2.2 High Speed Camera Requirements Experiment	30
3.0 Publication One: Micron-level Layerwise Surface Profilometry	34
Abstract	34
1.0 Introduction	35
1.1 Previous Work of Others	36
2.0 Methods and Materials	39
2.1 Laser Scan Profilometry and Recoating Carriage Mechanism	40

2.2 Benchmark Design with Inserted Intentional Defects	41
3.0 Results and Discussion	42
3.1 Carriage Location and Scan Map Repeatability	42
3.2 Optical Verification of the Intentional Defects	45
3.3 Detection of Lack of Fusion Defects	47
3.3 Detection of Spatter Contamination on the Powder Bed and other Melted Surfaces	48
3.4 3D Visualization and Detection of recoater flaws	49
4.0 Conclusions	50
Acknowledgments	51
4.0 Publication Two: Low Cost, High Speed Stereovision	52
Abstract	52
1.0 Introduction	53
1.1 Previous Work of Others	54
2.0 Methods and Materials	57
2.1 High speed stereovision camera system	57
2.2 Stereovision and Epipolar Geometry to identify position and direction of spatter	58
3.0 Results and Discussion	60
3.1 Sequential versus single image spatter tracking	61
3.2 Stereo imaging of spatter and determination of velocity and direction	63
3.3 Spatter calving and implications on melt pool location and contour determination	66
4.0 Conclusions	67
Acknowledgments	68
5.0 Publication Three: Statistical Analysis of Spatter Velocity	69
Abstract	69
1.0 Results and Discussion	70
1.1 Velocity Subset Validation of Stereovision Tracking	70
1.2 Stereo imaging of spatter and determination of bulk statistical velocity	72
2.0 Conclusion	75
Acknowledgments	76

6.0 Publication Four: Computer Vision for Spatter Motion Analysis	77
Abstract	77
1.0 Introduction	78
2.0 Methods and Materials	80
3.0 Results and Discussion	82
4.0 Conclusion	90
Acknowledgments	91
7.0 Conclusion	92
8.0 Future Work	93
8.0 References	94
9.0 Publications & Conferences	100
Appendix A: Single Camera Rectification Code	102
Appendix B: Stereo Calibration Code	109
Appendix C: Spatter Tracking Code .cpp	123
Appendix D: Spatter Tracking Code .hpp	128
Appendix E: Matlab Code For Analyzing .cpp Output	132

List of Figures

Figure 1: Layer View of Laser Scanning Process.....	5
Figure 2: 3DSystems ProX 320 Setup	21
Figure 3: Build Direction Shown of Microscopy Samples.....	22
Figure 4: Powder Sample Collection Regions.....	22
Figure 5: Particle Size Distribution Results for Virgin Powder and Zone 3 Powder Using Inconel 718.....	24
Figure 6: SEM Images from Virgin, Zone 2, and Zone 3 Powder	25
Figure 7: SEM EDS Analysis of Virgin Inconel 718 Powder	26
Figure 8: Optical Microscopy Images from Inconel 718 Samples Taken from the Respective Corners of the Build Plate at 50x Magnification.....	28
Figure 9: CT Analysis Images of Inconel 718 Samples Taken from Respective Corners of the Build Plate	29
Figure 10: Tensile Specimen Results for Inconel 718 Built in the Optimized Order.....	30
Figure 11: Camera Variables to Optimize Image	30
Figure 12: Image of Video Taken at 1000 fps and 200 μ s Shutter Speed.....	31
Figure 13: Image of Video Taken at 5000 fps and 129 μ s Shutter Speed.....	32
Figure 14: Laser Scan Profilometer Bracketed on ProX 320 Recoating Arm.....	41
Figure 15: Experimental Design: Intentional Negative and Positive Defects with Ruler Bar.....	42
Figure 16: Repeatability Analysis Study with Variance.....	44
Figure 17: Optical Verification of the Defect Simulations in Inconel 718.....	46
Figure 18: Optical Verification of Defect Simulations in AlSi10Mg (note poor numbering resolution due to printer).	46
Figure 19: Single Scan of the top surface directly after the 9th layer, high elevation in red and depression in blue.....	48
Figure 20: A 5 x 5 Pixel sliding window variance of the scan in Figure 19 . Note the low variance in the lower powder region.....	48
Figure 21: Increased height donated by red coloring, shows increased likely hood of spatter contamination at the top of the scan.....	49
Figure 22: 3D Isometric view of surface layer, showing both positive and negative defects, and possible recoater flaws.....	50
Figure 23: EOS M290 with Front Port Window (Left) and Stereovision Schematic (Right).....	57
Figure 24: Stereo Calibration between two coincident images from different perspectives	59
Figure 25: Stereovision quality assurance using a caliper (50.01 mm top, and 9.99 mm bottom).....	60
Figure 26: Sequential imaging of the right camera to demonstrate that tracked spatter measurements (frame to frame with an overlay) can be obtained in a single image.	63

Figure 27: Stereovision imaging of spatter of varying directions and speeds (+Z into plane).....	65
Figure 28: Spatter calving where new spatter particles have been formed and are being ejected.....	67
Figure 33: Spatter detected on edge of part as laser path is changing direction, laser direction indicated showing path during spatter formation	71
Figure 34: 10,447 Spatter magnitude vectors plotted centering each spatter to the same origin point, detected over a seven second imaging period.....	73
Figure 35: 10,447 Spatter detected graphed with velocity vs frequency.....	74
Figure 36: Laser Parameter Design of Experiments shaded from white to black with calculated energy density.....	81
Figure 37: Quantity of spatter detected verse spatter velocity for the laser parameters 370 watts laser power, 1400 mm/s scanning speed, at 60 μm layer thickness	83
Figure 38: Histograms laid out as shown in Figure 36 and Figure 37 . All Populations normalized to 1100 spatter and analyzed verse spatter velocity in 1.0 m/s increments. ..	84
Figure 39: Quantity of spatter for the 60 μm layer series vs 3D Energy Density.....	85
Figure 40: Quantity of spatter less than 1.0 m/s detected verse energy density with constant 60 μm layer thickness.....	86
Figure 41: Quantity of spatter greater than 1.0 m/s detected verse energy density with constant 60 μm layer thickness.....	86
Figure 42: <i>Energy Density vs Quantity detected above 1.0 m/s and below 4.0 m/s for 60 μm layers with the population normalized at 1100 total spatter</i>	87
Figure 43: Histogram results showing spatter detected above and below 1.0 m/s for various laser parameter settings all at 60 μm layers	87
Figure 44: Diagram showing vertical angle with respect to raster direction and x, y, z coordinates	88
Figure 45: Average vertical angle compared to spatter velocity range for varying laser parameter sets all recorded at 60 μm layers.....	89

List of Tables

Table 1: Surface Oxidation Analysis of Virgin, Zone 2, and Zone 3 Powder	27
Table 2: High Speed Analysis Results Showing Chosen fps/Shutter Speed	33
Table 3: Spatter from Figure 27 described in direction and velocity	65
Table 4: Spatter detected on edge of part with laser turning to head in opposite direction, first ten results shown with bulk statistics below, exposure of 500 μ s	71
Table 5: Measured beginning and end points for first 10 spatter from Figure 34 , their calculated magnitudes and velocities, and bulk statistical results.	74
Table 6: Average Vertical Angle for various laser powers and scanning speeds	88

1.0 Introductory

Additive manufacturing (AM) is a “process of joining materials to make parts... from 3D model data, usually layer... upon layer, as opposed to subtractive manufacturing and formative manufacturing methodologies” [1]. This allows for the creation of complex parts with internal geometries not possible by normal subtractive methods and finds its history in welding [2]. Lattice structures are a prime example of a geometry not possible through normal manufacturing means, as drilling the internal structure or creating a mold to cast the product is not possible [3]. Due to this innovation, numerous industries have been looking to AM as a method to create tooling and/or directly create parts [4].

1.1 Powder Bed Fusion

Powder bed fusion, PBF [1,5,6] shows promise in the aerospace industry for providing complex structures fabricated with high performance metal alloys that are spatially tailored for both effectiveness and low weight. Additionally, the geometric freedom has allowed for improvements in the medical field both with surgery implants and other devices[7–9]. The PBF process is done in a layer-by-layer fashion whereby a layer of powder is spread and then a laser, electron beam, or other irradiation method will sinter/melt the desired sections. This is then repeated until the desired part is completed. This process is limited by the ability of the material to be fused together using the designated heat source, and the spot size interacting with the powder particles of a given diameter. Powder bed fusion layer thickness ranges from 20 μm to 200 μm , with the average particle diameter being at or below the layer thickness to enable accurate spreading of the next layer [10].

1.2 Laser Powder Bed Fusion

Within the taxonomy of PBF, laser powder bed fusion (LPBF) and more specifically, metal LPBF (M-LPBF) has been optimized to create complex with high performance geometries in a range of metal alloys [1,11]. Due to the nature of metal laser melting, rapid heating and cooling processes can create internal stresses and defects in a part. Laser parameters are chosen to increase the density of the part, decrease the build time, decrease the internal stress, decrease the surface roughness, and optimize the microstructure [12–18].

1.2.1 M-LPBF Build Parameters

Build files for M-LPBF contain all of the build parameters needed to create the part. These parameters are layer thickness, laser power, scanning speed, hatch spacing, contour parameters, stripe width, hatching strategy, recoater direction, build part order, and part orientation. Some of these parameters are machine specific as there can only be one choice, for example, the EOS M290 and M280 systems can only have a recoater go from right to left; however, the 3DSYSTEMS ProX series printers have a bidirectional recoater, which can be down selected to recoat in only one direction. Most of these parameters have multiple options and are optimized for the material and desired outcome. Optimization considers to parts, printing speed and quality. A smooth surface finish might be less desirable than speed in which case a 60 μm layer could be used instead of a 30 μm layer and thereby a print could be done in half of the needed time [19,20].

Layer Thickness in M-LPBF is often chosen between 20 μm and 60 μm layers. There are some cases where a smaller or larger layer thickness will be utilized, but this is not the norm. The layer thickness is chosen to optimize the build time, with comparison

to the machine laser wattage capabilities, the material properties, and the desired outcome of the part parameters. For example, a 30 μm layer build may take one to two weeks of machine time, whereas a 60 μm build will be approximately half of that time. However, increasing the layer thickness makes it significantly harder to control the surface finish, thereby resulting in a rougher Ra value for the part [20]. Additionally, each material will have an envelope of optimal energy input for a designated layer thickness. The calculation of the overall energy density input is given by the three-dimensional energy density equation:

$$Q = \frac{P}{V * T * H} \quad (eq.1)$$

where Q is energy density, P is laser power (Watts), V is scan speed (mm/s), T is layer thickness (μm), and H is hatch spacing (μm) [19].

Laser Power in M-LPBF is given in units of Watts. The most common laser type is a fiber laser with approximately a 1070 nm wavelength with a maximum power between 100 and 500 W. For a given material, a laser power will be selected in combination with the desired layer thickness and scan speed. These inputs directly affect the speed of the build and therefore are optimized. Certain materials require a much higher energy density due to the reflective nature of the material, heat conductance, or increased melting temperature of the material. Due to this, a more costly machine with a higher max laser power may be required. Green lasers have been used to print copper, but due to the drastically increased cost of the laser are not the preferred approach [21]. Laser spot size is also typically set for each machine type, and while this does influence the energy density it will be addressed more fully during the hatch spacing section.

Scan Speed is how quickly the laser spot rasters across the build plate. This is often given in millimeters per second (mm/s) and can range from 100 mm/s to 1800 mm/s. When combined with the laser power it creates an envelope of acceptable range that can be identified for each material type. Laser power and scan speed are the most commonly adjusted parameters for each layer thickness, as additional variables such as the hatch spacing are dependent upon the laser spot size which is usually a constant for each machine [22].

Hatch Spacing is the gap between each raster (see **Figure 1**) [23]. The hatch spacing is often a set value based on the laser spot size for the machine. For example, a machine with a laser spot size of 80 μm will often utilize a hatch spacing of 100 - 120 μm . The melt pool being rastered across the layer is often larger than the laser spot size due to the large input of energy into the material. The hatch spacing is based on the melt pool for the material with an appropriate overlap hatch to hatch. Slowing down the scan speed will also increase the melt pool tracks and will give more overlap between each hatch.

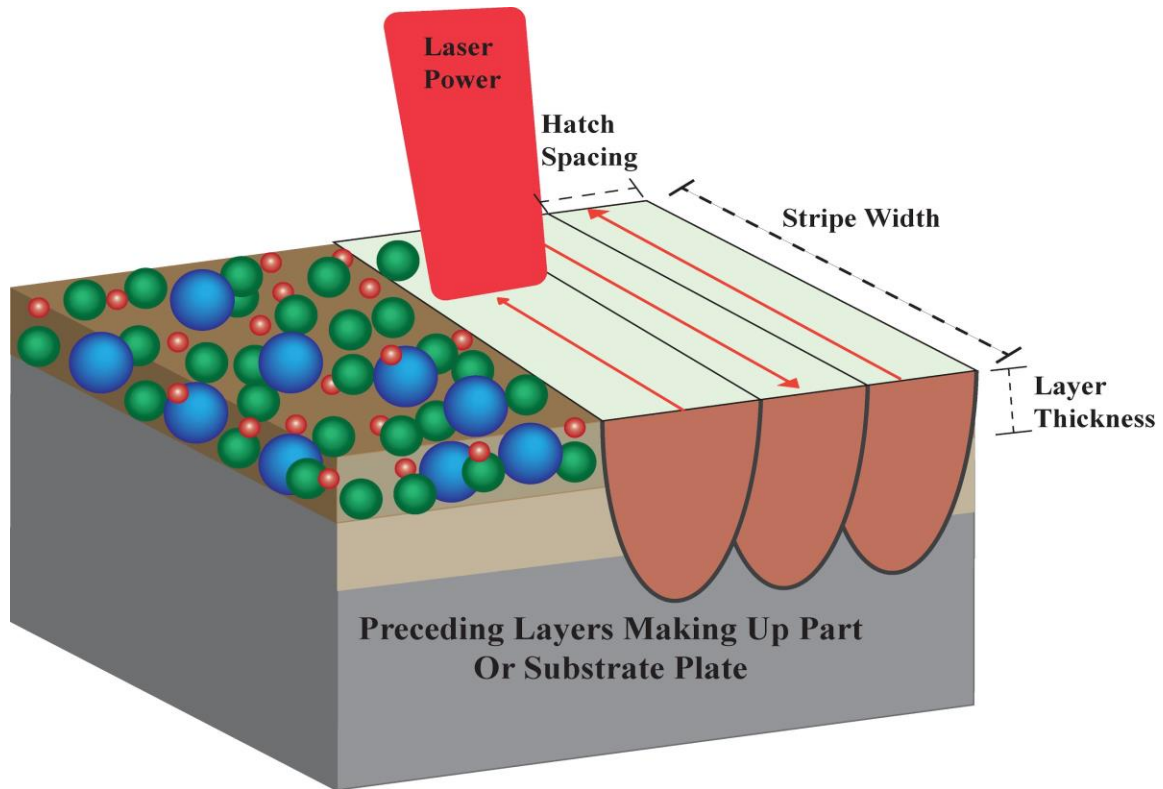


Figure 1: Layer View of Laser Scanning Process

Scanning Strategy is the pattern created by multiple rasters and usually has a designated geometric name for each type. The goal is to create raster paths that are close together and control the amount of heat lost between each pass [23,24].

Recoater Parameters include the recoater direction and speed. Most machines have a single set recoater direction and is therefore not a variable. Certain machines like the 3D Systems ProX line have a bidirectional recoater which can be set to recoat from both directions, or from a single direction. The recoating from each direction can aid in the elimination of short feed issues, however, certain errors can occur with only one direction of the recoat during the build, and this additional variable needs monitoring to ensure quality assurance. The goal of proper recoat speed is to form a tumbling motion with the powder and allow for a uniform spread across the layer. The density, sphericity,

humidity, and layer thickness of the powder all effect this motion. Additionally, various recoater blade types which can vary from soft silicone to hard ceramic influence this motion as well. Hard recoaters can be effective in creating a tumbling motion especially for a high density material such as Inconel 718, however, when lattice features are being lasered, it is known that the spreader can impact these features when they are raised above the subsequent layer thickness due to laser parameters. This particularly happens during the creation of a lattice support feature. Soft recoaters, are malleable and will deform rather than impacting the part, however, this can result in the flinging of powder onto the build surface or the damaging of the soft recoater. Soft recoaters are typically damaged by the formation of slits where the metal cuts them as it is dragged over the top, which leads to streaks in the powder layer and thereby subsequent layers of the part. In extreme circumstances a chunk can be removed which creates a large defect spread over the subsequent layers and will ultimately lead to a catastrophic failure of the build. Metal brush recoaters and rollers (similar to a rolling pin motion) are also utilized to try to effectively spread each layer. All can be utilized effectively with appropriate laser and speed settings and have various nuance issues with different materials.

Build Part Order is the order in which the parts are melted. This is often selected considering the flow of the argon within the chamber. As the layer undergoes the laser melting process molten metal ejecta (spatter) are often formed which are redirected by the flow of the argon across the build surface. Argon flow serves multiple purposes, it redirects soot which keeps the laser optics clean, it redirects spatter toward the back of the plate, it provides an inert environment for the welding process, and it will cycle through a filter to keep the chamber cleaner. Due to this a larger the normal collection of spatter is directed

with the argon flow and can have a negative impact on the parts where it falls. Therefore, the sintering order is chosen to reduce this impact [23,25,26].

1.2.1 M-LPBF Melt Pool Characteristics

During LPBF, the melt pool is moved back and forth due to the laser hatching strategy. Since the melt pool is responsible for the layerwise bonding to each previous layer(s), the melt pool characteristics play a crucial role in the eventual resulting microstructure. Therefore, a clear understanding of the melt pool is key.

Previous work has extensively examined the melt pool shape, temperature, and influence during the LPBF process. Two types of melt pools were identified by Criaes *et al*, with type 1 being when the laser first reverses direction and the melt pool is significantly larger due to the heat-affected zone of the previous raster, and type 2 being smaller after the laser is rastering down its designated path and the previous raster has cooled. Since the previous raster has had time to reduce its temperature from the high initial melting point, the heat affected zone is less influential, this second type is more “nominal” conditions until the end of the raster is reached and the direction is reversed again. It was noted that due to this process the melt pool was skewed in the direction of the previous raster (or heat-affected zone). Additionally, smaller rasters have are more influenced by the previous raster has there is less time for heat dissipation [27].

Laser energy density (defined by laser beam power divided by scanning speed), was examined with its impact on melt pool geometry using Hastelloy X provided by EOS Gmbh on an EOS M290. It was identified that decreasing laser power while holding scanning speed resulted in a large decrease in the melt pool (65% in depth and 30% in width); however, increasing scanning speed resulted in a smaller decrease in the melt pool

(38% in depth and 13% in width). Due to this phenomenon holding the laser energy density constant with an increased laser power resulted in an increased melt pool depth [18].

An example of the potential uses of melt pool tracking from *in situ* monitoring is when it is used to improve laser parameter development. Currently, the development of new parameters for new materials is iterative and time consuming. This approach was examined by Hooper where he reported the examined predicted temperature fields [28]. His approach was to use a two wavelength high-speed imaging thermography method to map the melt pool in Ti6AlV4. Of note, it was demonstrated that when the laser hatch changes direction the temperature often exceeds the boiling point of the material, and there is an increase in plume ejection (spatter). This work was done on a Renishaw AM 250 with a pulsed instead of continuous laser so the specific physics involved may be slightly different than on a continuous laser system like an EOS, Open Additive, or 3DSystems machine. A reference to the physics based modeling done by Khairallah *et al* [25]. was made to which a liquid build should be formed through the hatch and therefore a larger temperature should be measured at the end of the hatch. This was predicted by the modeling of Khairallah *et al.* [25] and validated by the measurements taken by Hooper [28].

Khairallah *et al.* [25], examined the melt pool through physics based modeling and showed several interesting phenomenon in regards to the melt pool track formation, and the groups work is noted in several different journal publications [25,29–31]. Their work resulted in the melt pool track being differentiated into three distinct regions: at the laser spot they had a depression region, then a transient region, and finally a tail end region. The driving recoil force at the depression region would resolve into a surface tension in the tail end region. This work demonstrated that Marangoni forces and recoil pressure shape the

melt pool flow. When the hatch changes direction, a splashing effect can also take place which can further lead to spatter formation. This provides an explanation for the formation of spatter, denudation zones, and pores. Deep narrow depression regions were advised to be avoided as they could lead to pore formation [25,29,30]. This shows that a commonly held belief in the LPBF community that too high of laser power leads to key holing pores and too low of laser power leads to lack of fusion pores. This process could also explain the increase amount of keyholing noted when the laser changes direction, as it is essentially using too much laser power over a region as it has not cooled when compared to the region in the middle of a hatch [29]. Martin *et al.* [29] showed that this would also could be from the initial laser depression region collapsing on itself. The conclusion from this groups work seems to be that laser power and scanning speed are the main parameters in spatter and pore production.

Masoomi *et al.* [32] has worked on similar physics based models which additionally examined multiple laser systems and varying scanning strategies. This work concluded that peak melt pool temperatures were found to be almost independent of scan strategy and number of laser used. The employment of island division schemes allowed for shorter hatch track lengths which was noted to reduce residual stress magnitudes as it decreased the thermal gradient of the region being lasered. Therefore it was advised to maintain shorter tracks and rotate angles of the hatching strategy for proper layer overlap [32].

Heeling *et al.* [10] also developed a model for melt pool simulation and noted the importance of the Marangoni convection and the recoil pressure which were driven by the laser parameters. Compared to the titanium work previously noted, Heeling *et al.* focused on stainless steel 316L and Inconel 738LC. This work showed the previous layer as having

a large amount of residual heat which increased the depth of the melt pool. Controlling melt pool depth and width seemed key and it was believed that this model could assist in the development of laser parameters for new materials.

With this foundation of melt pool characteristics, advancement can now be made to identify and eventually prevent adverse conditions. Wave emission modes have been analyzed to stabilize the melt pool [33], correlation between melt pool events and tensile properties were examined [34], as well as the development of machine learning to identify *in situ* melt pool signatures [35]. These advancements will all aid in the qualification and standardization of LPBF.

1.2.2 M-LPBF Microstructure Characteristics

In order to explain how LPBF microstructure is unique, a casting microstructure of AlSi10Mg will be used as a reference. AlSi10Mg is a hypoeutectic aluminum alloy commonly used in the LPBF and casting realms. The properties are particularly useful for the aerospace and automotive industries [36,37]. The aluminum silicon eutectic is at 12.2% silicon dissolved in aluminum. In AlSi10Mg the addition of the 10% silicon is to decrease the melting temperature, decrease quench cracking, and increase the fluidity of the alloy for casting; while the addition of magnesium is to create a heat treatable Al-Si metal through precipitation hardening [38]. The commonly used AlSi10Mg alloy provided by EOS for M-LPBF has 0.2-0.45% Magnesium[39]. The microstructure of AlSi10Mg when cast has large α -Al regions with Al-Si eutectic regions and magnesium precipitates mixed throughout [40–43]. In casting, a mixture of columnar grains along the casting wall and equiaxed grains in the center with the amount varying based on the cooling rates are

common. However, with the rapid heating and cooling, as well as the repeat heating of the subsequent layer with the laser in LPBF, the grain structure is smaller [44].

The microstructure of M-LPBF AlSi10Mg often has columnar grains along the z-axis of the build orientation. This is due to the repeat melting from each layer, and so grains can travel through multiple layers [36,42,44]. Looking at the XY plane on the top surface the melt pool often presents with curved columnar grains along the sides of the laser track and equiaxed grains in the center of the laser track [45]. Additionally, coarse zones tend to be present at the border of the melt pool containing α -Al in a more equiaxed state with fine zones being present in the center of the melt pool (center of a hatch laser track). As the laser beam is rastering across the layer (see **Figure 1**), the melt pool often extends down two to three previous layers. Examining the melt pool in the z-direction, the fine zones were shown to be in the melt pool, the coarse zones were in the semi-solid region where the laser has stopped heating the metal to the melting temperature, and below that region there is a heat affected zone [44]. This remelting and heat treating subsequent regions layer after layer results in a complex microstructure for LPBF as-built parts, where cell spacing in the microstructure strongly depends on the cooling rate at the solid-liquid interface during solidification [18].

Three dimensional multi-layer grain structures have been examined for M-LPBF and resulted in interesting findings. Koepf *et al.* analyzed and simulated the grain structure and preferred orientations for growth [46]. While the outcome will be material specific (Inconel 718 was used) as to the preferred orientations, the simulation showed a strong tendency for the grains to keep growing in a vertical direction along the z-axis of the part orientation. Additionally, the work showed that unfavorable grain orientations were

overtaken and drastically reduced after the first millimeter of the build. Therefore, there was more uniformity throughout the center and upper regions of the part.

Thijs *et al.* [47] examined rotating scanning strategies by 90° in AlSi10Mg to examine the crystal orientation. The primary $\langle 1\ 0\ 0 \rangle$ crystal direction was preferred, and it was noted that the diamond-like silicon phase positioned around the face centered cubic aluminum cells. The favorable $\langle 1\ 0\ 0 \rangle$ crystal direction was shown to grow in columnar grains between multiple layers; however, when the angle for the next layer was rotated 90° less favorable competitive grains could be shown growing. These competitive grains were noted to only grow in a single layer and were not noted to be favorable through multiple layers. Decreasing the layer thickness and/or hatch spacing was believed to intensify the crystal structure [47].

Building from this work, Qin *et al.* [48] analyzed the texture and grain size evolution for AlSi10Mg with a 67° rotating hatching strategy for each layer. It was noted that larger grains often formed in the center of the melt-pool along the z-axis of the build which was contributed to the successive remelting of the previous layers as well as the direction of the heat removal from the part going down the z-axis into the build plate. Similar to the work presented by Thijs *et al.*, the primary $\langle 1\ 0\ 0 \rangle$ orientation was favorable along the build direction. However, it was noted that the weaker $\langle 1\ 1\ 0 \rangle$ and $\langle 1\ 1\ 1 \rangle$ orientations were present on the rotated hatch angles from around $20^{\circ} - 70^{\circ}$. The crystallographic structure texture was reduced with this improved hatching rotation and resulted in a much more randomized pattern. It is therefore believed that increasing this randomization allows for decrease in build part orientation weaknesses and an increase in part strength [48].

1.2.3 M-LPBF Defects

Due to the uniqueness of the LPBF manufacturing process, it is affected by several unique types of defects such as lack of fusion [19], keyholing [49], balling [25], spatter [27], residual gas porosity [50], hatching strategy defects [51] and recoater defects [51]. These issues can range from a small anomaly which does not negatively impact the quality of the part to a catastrophic failure which crashes the build in process. Brown [52] focused on the lack of quality assurance which results from these defects and the inconsistency of additively manufactured parts build to build, during a recent conference presentation.

[53] provides an overview of *in situ* and nondestructive evaluation. The most common defects monitored in the LPBF realm are those of key holing and lack of fusion [23,25,54,55]. Key holing is often associated with the creation of a small micropore below the surface due to the vaporization of metal during the lasing process. This is commonly believed to be a result of elevated of an energy density (i.e. too high of a laser wattage and/or too slow of a laser scanning speed) [54]. In contrast, lack of fusion defects are created by unfused (unsintered) powder which was created from an incomplete sintering process [19,23,56]. This often leaves a void and/or weak point in the part resulting in a pore. Laser parameters which do not transmit the required energy into the part thereby not properly sintering often cause these defects. Another method for the creation of these defects is powder particles which are too large to be sintered and spread evenly can inhibit the proper lasing. Spatter has been identified as a method which forms these large particles during the build and can cause these defects [57].

1.2.4 Spatter Generation and Defect Causation

Spatter is defined by Merriam Webster dictionary as a verb which is “to spurt forth in scattered droplets” [58]. Particles are formed during the cooling and resolidification of these ejected droplets (spatter) from the sintering process. Yadroitsev *et al.* [59], discussed melt pool instabilities in LPBF and vapor pressure formation on top of the melt pool. Wang *et al.* [60] described the formation by classifying them in three main types: type one is spatter ejecting vertically and is included in the metallic jet (attributed to a recoil pressure zone); type two was spatter forming from melt pool surface instability and are typically ejected backwards; and type three are non-melted particles in front of the melt pool. Keyhole formation was mentioned as a possible contributor to spatter formation.

Khairallah *et al.* [25] attributed the creation of these ejecta particles to marangoni forces that build up due to the rapid heating and vaporization of certain elements. Ly *et al.* [30] continued on this work, by performing hydrodynamic finite element modeling studies and ultra-high speed experimentation to analyze micro-droplet spatter ejection. Their work utilized a custom LPBF setup with a 100,000 frames per second (100 kfps) and analyzed single track scans on the powder bed. The work which analyzed SS 316L, examined two laser parameter conditions (150W at 500 m/s, and 200W at 1500 mm/s). The angle of the spatter and the velocity of the spatter was significantly different for the two laser parameters. The increased angle of ejection was attributed to the increased depth in cavity formation from the greater laser energy. The recoil pressure ejected the particle with greater force and the deeper cavity forced the spatter in a more vertical direction. Therefore, it is expected that spatter velocity and angle would both be increased with increased laser energy density. The simulation work corresponded well with the experimental work and

three types of spatter resulted from their study. The first, was noted to create 60% of the spatter and was identified as hot entrainment ejections with velocities of 6-20 m/s, the second was 25% of the created spatter and were cold entrainment ejections with velocities of 2-4 m/s, and final type was droplet breakup ejections due to recoil pressure with velocities of 3-8 m/s [30].

Gunenthiram *et al.* [61] analyzed spatter formation with SS 316L and cross compared it to Al4047 using the single track method with a 70 μm thick layer. This work linked increased three dimensional energy density to increased spatter formation. Vaporization and recoil pressure were attributed to the formation of spatter with vaporization being attributed to the main role. The SS 316L produced on the order of three times more particles than the Al4047. Also of importance was that most of the spatter identified in this study were formed in the powder bed near the melt pool, then attracted to the melt pool surface by Bernoulli like effects, and ejected upwards as Wang *et al.* had identified in type 3 spatter [60]. However, this work disagreed with the analysis by Wang *et al.* in that observations showed the formation of spatter at the melt pool and powder bed interface rather than the melt pool surface. It was noted that this could be a unique feature of the CoCr that Wang *et al.* had used, but opened the door for further study being needed.

Nassar *et al.* [57] examined the formation of large spatter and provided high speed evidence that three main methodologies can exist. Type one, collision and coalescence of spatter from distant or non-adjacent locations; type two, collision and coalescence of spatter from adjacent or neighboring locations; and type three, the vapor plume causing coalescence of partially sintered agglomerates. This work is crucial as it brings a viable

explanation for large rogue spatter formation not present in the physics based models thus far; although Ly *et al.* [30], did show the neighboring collision and coalescence.

Particles are generally considered to be larger than feedstock powder, which can directly affect the quality of the manufacturing process by obstructed the laser melting at that point. Spatter particles ejected from the melt pool can land on the melted section and these particles can be much larger than the D90 size of the powder size distribution and negatively impact the subsequent layers [25,27,61–66]. This then results in the formation of a lack of fusion defect because, even though the surrounding powder can melt, the large spatter can give rise to either unfused regions or create a cavity around the particle. Spatter can lead to other negative effects such as increasing surface roughness of a part [12] or even increasing the local layer thickness [64], large spatter particles can cause damage to the recoater blade, and spatter can also land in unfused powder changing the local powder packing density and chemistry - either of which can affect melting behavior due to particle size differences.

Traditional arc welding and laser welding also create spatter and the spatter is studied to gain insight into the quality of the structure under development [64,67–69]. Additionally, since the final destination of the spatter after ejection can have a negative impact on the part under fabrication, understanding the processes involved might assist in determining the overall quality of a build.

1.2.5 Post Processing

Post processing of M-LPBF parts often include stress relieving the part before removal from the base substrate to avoid distortion, and hot isostatic pressing (HIP) the part to reduce the size of any defects present and their likely cause of failure in the part.

Process feedback is generally absent in production systems and is understood to remain as an eventual requirement for full qualification of these processes [70].

In order to broaden industrial adoption, evidence of the reliability of the fabricated structures will need to be collected *in situ* for each and every fabrication [11]. Given the layer-by-layer processing with an unobstructed view of the top surface of the structure during fabrication, crucial aspects of the manufacturing process can be monitored in an unprecedented manner including the melt pool, ejecta, and surface topology [53,61,70–74]. By characterizing this process and understanding the implications on process quality, a *qualify-as-you-go* methodology can be adopted as is required for manufacturing of critical hardware [75]. The key to this advancement is in the understanding of the melt pool and microstructure characteristics which provide a fuller understanding of the effect of each type of defect.

1.3 *In Situ* Monitoring

Nondestructive evaluation/testing (NDE) methods were created to qualify and certify parts produced by traditional methods such as machining and casting; however, due to the complex internal features often associated with LPBF parts, these methods are often inadequate and/or not fully developed in identifying defects [55]. Additionally, the advancement of technology such as CT scanning has allowed for the identification of smaller defects than could be seen when traditional standards (such as those for casting) were developed [76,77]. Therefore, the combination of new standards needing to be developed and the new identification of defects has led to a search and development of new quality control measures. Because of the unique layerwise process in additive

manufacturing *in situ* monitoring seems a logical option as it would enable the current qualification of parts and possibly allow for the development of feedback loop system in the future to resolve these defects in real time.

In situ monitoring with the ultimate goal of providing feedback control has been researched in a variety of methods. [65,66,78–80] all have explored the implications and behaviors of spatter in M-LPBF but none explored the use of high speed stereovision at the macro level to track the travel trends of spatter in the build chamber. Spatter in welding has also been explored and provides insights into AM spatter, but is fundamentally different as the processes are not the same. [71–73,81–85]; all investigated monitoring the process at the melt pool by measuring the melt pool shape and temperature, and although the melt pool is the origin of spatter, this subject is outside of the scope of this work. The melt pool is essential to the outcomes of the M-LPBF process and clearly is critical to understanding the quality of a fabrication; [84,86–89]; monitored and tracked the scan path which anecdotally has a significant impact on the amount and direction of spatter.

1.3.1 High Speed Monitoring

High speed digital photography has been utilized to characterize spatter in several studies. Frame rates used include 1,000 fps [78], 2000 fps [67], 6000 fps [66] for laser additive processes. High speed thermal cameras have also been leveraged with frame rates of 1800 fps [27]. High speed photography (3000 and 6000 fps) has also been used to characterize the behavior of interacting spatter for a multi-laser SLM 280 HL system [65].

The use of ultra-high speed imaging (100,000 frames per second) has uncovered that the mechanism causing spatter is from vapor driven entrainment of micro-particles by

an ambient gas flow [30]. Previously, it was believed that spatter was caused by laser induced recoil pressure (which is still true for laser welding processes, see [67]). Ly *et al.* identified three distinct types of particles. The first involve particles with low vertical momentum that are carried into the melt pool. The second category of spatter particles have higher vertical momentum but originating more than two melt pool widths away from the beam and are carried into the trailing portion of the vapor jet. These are then ejected as cold particles. The three categories of spatter particles are closer to the laser beam than the second category. These spatter particles are carried into the laser beam which heats the particles to the point of becoming incandescent, hot particles. With a scan speed of 1.5 m/s and laser of 200W and fusing stainless steel 316 powder, Ly *et al.* found that 60% of spatter particles observed are the third category (hot particle ejections) with velocities of 6–20 m/s and observed particle full width at half maximum (FWHM) diameters of 10 to 30 microns, another 25% are the second category (cold entrainment ejections) with velocities of 2–4 m/s and FWHM diameters of 20 to 30 microns, and the remaining 15% are recoil pressure induced droplet breakup ejections with velocities of 3–8 m/s and FWHM diameters of 15 to 70 microns. It should be noted that this work did not occur in a chamber with flowing inert gas (i.e. argon) over the powder bed as is common in most production systems. This inert gas flow could influence the flight path of the spatter particles [30].

1.4 Research Questions and Hypothesis

This work is focusing on the effect of spatter on the M-LPBF process, and will seek to determine some of the following:

1. Does spatter influence the part quality and if so, does lasering order reduce this effect?

It is believed and the machine manufacturer recommendations coincide suggest that the order in which the parts are lasered on a build can influence the part quality. The suggested pattern is to laser parts in the order against the flow of argon so that spatter is directed on already lasered sections of the build area.

2. What type of high speed stereovision is sufficient to properly analyze spatter?

An initial study into the optics of high speed video and what would be sufficient quality of cameras to properly capture and analyze spatter will be performed. This question will drive the purchase of the high speed equipment utilized in this dissertation.

3. How do laser parameters affect the quantity and velocity of spatter?

It is believed that laser parameters, specifically those that influence energy density will have a direct effect on the quantity and velocity of the spatter produced. Initial belief is that an increase in energy density will increase the velocity of the spatter; however, an attempt will be made to determine if laser power or scanning speed has a greater influence.

2.0 Background Studies

The following studies were performed to lay the foundation for the work done during the publications (Chapters 3-6) and were presented at various conferences. These include verifying spatter impact on build density (Section 2.1), and identification of high speed camera requirements needed for the research performed (Section 2.2).

2.1 Spatter Impact Experiment

Spatter size determination is a central variable in the lack of fusion by spatter hypothesis. Therefore, initial experiments to validate the size distribution of spatter particles and the link to its effect on defect. The 3D Systems ProX 320 commercial system at YSU has a recirculating argon flow (argon knife) to blow spatter created off the build plate as well as filter the atmosphere present in the build chamber, **Figure 2**.

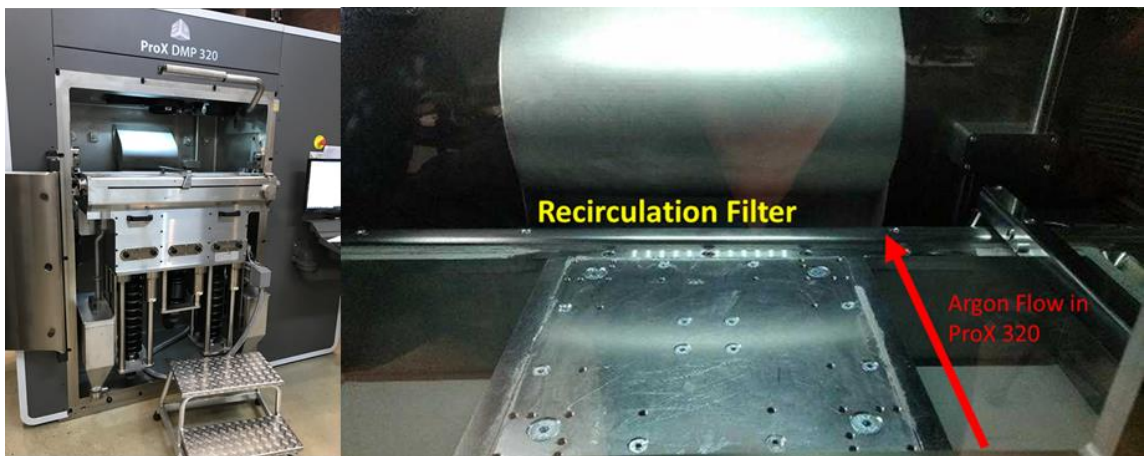


Figure 2: 3DSystems ProX 320 Setup

Due to this, an experiment was designed which consisted of multiple metallography cylinders built in array, with the left side being built in the order from the front of the chamber to the back and the right side being built in the order from the back to the front, **Figure 3**. The flow of the argon is from the front of the build chamber to the back.

Therefore, the cylinders in the front of the build chamber should be relatively unaffected by spatter (labeled zone 1), and the cylinders in the back of the build chamber should be affected by the spatter (labeled zone 2). Furthermore, the back ledges of the build chamber often collect spatter during the build process and can be analyzed to determine the spatter size distribution (labeled zone 3), **Figure 4**.

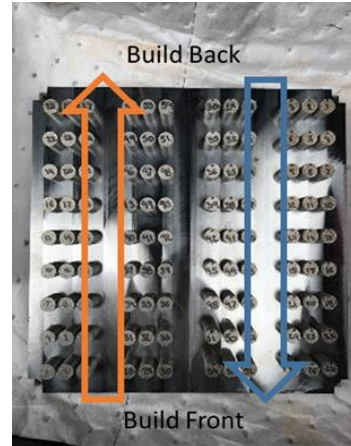


Figure 3: Build Direction Shown of Microscopy Samples

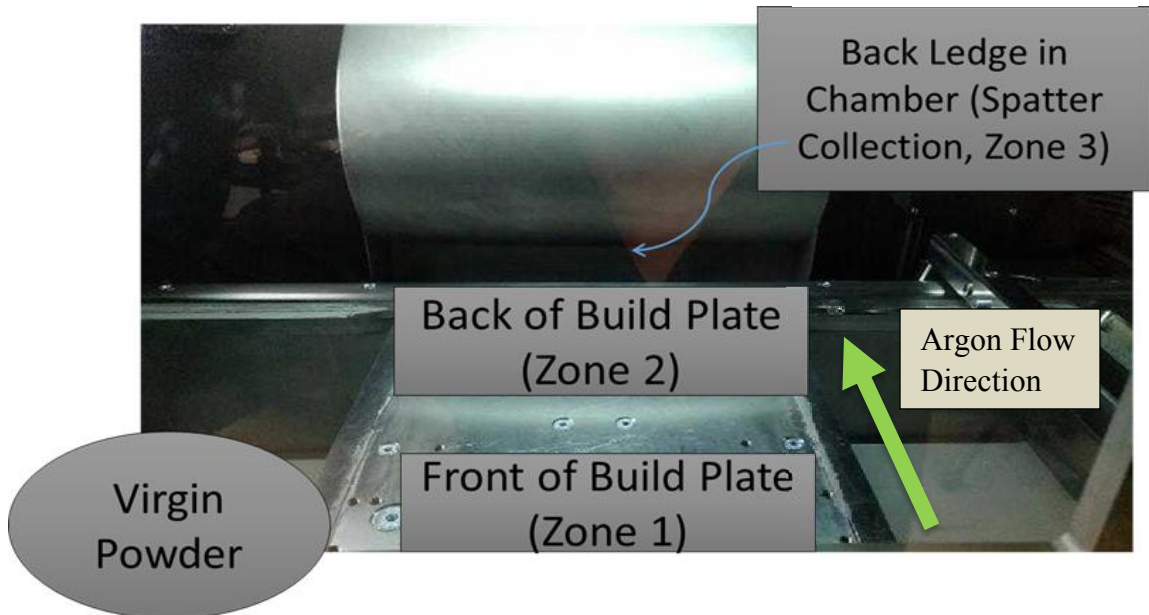


Figure 4: Powder Sample Collection Regions

2.1.1 Particle Size Distribution Determination

Powder samples were taken from each of these zones and analyzed for their average particle size distribution using a Cilas 1190L liquid laser particle size analyzer. The machine works using the Fraunhofer diffraction theory, which states the particle size is proportional to the intensity of the light scattered [90]. Additionally, there is an inverse

relationship between the angle of the lasers (the Cilas 1190L uses a patented tri-laser design) and the particle size such that the diffracted angle increases as the particle size decreases [91]. These results were used to determine the histogram spreads of the particle sizes for the different powders and thereby find the difference between the virgin powder particles and the presumed spatter particles. Samples were run with water as the medium after three trials of blank water to normalize the system. Inconel powder was then measured by weight and added to the system. Several trials were performed before measurements were recorded as to determine the correct weight of powder needed to provide the optimal feedback with the laser system. The optimal amount was determined to be around 5.0 grams for this machine under these settings. **Figure 5** shows the difference between virgin powder and the spatter collected in zone 3. The measured distribution for the virgin powder was $d_{10} = 18.6 \mu\text{m}$, $d_{50} = 32.1 \mu\text{m}$ and $d_{90} = 79.2 \mu\text{m}$; and for the zone three group was $d_{10} = 40.3 \mu\text{m}$, $d_{50} = 68.8 \mu\text{m}$, $d_{90} = 106.6 \mu\text{m}$. These results clearly show the particles collected in zone 3 as much larger; and follow the trend of Gunenthiram *et al.* which had results of $20 \mu\text{m} - 200 \mu\text{m}$ [61].

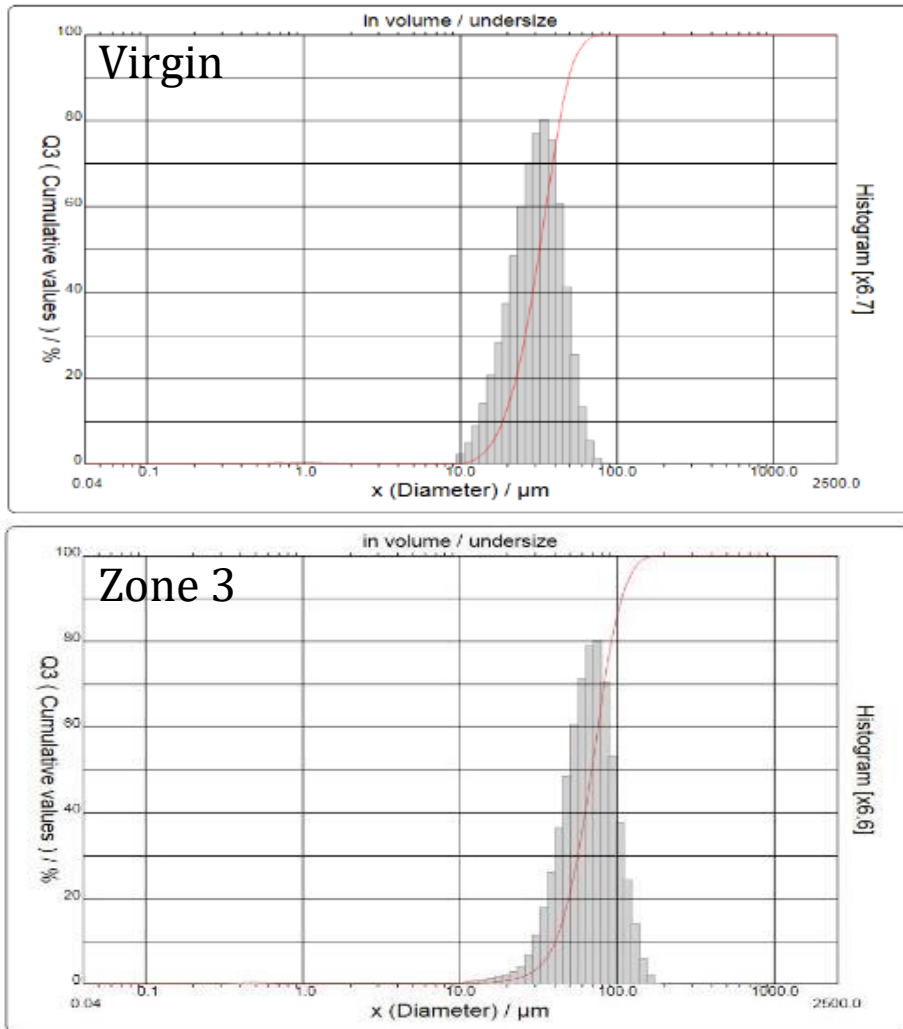


Figure 5: Particle Size Distribution Results for Virgin Powder and Zone 3 Powder Using Inconel 718

2.1.2 Scanning Electron Microscope Analysis of Spatter

Scanning electron microscopy (SEM) was used to analyze the spatter to gain more insight into their characteristics. A JOEL JSM-7600F SEM with a 0.1 to 30kV accelerating voltage was used which was further equipped with an EDAX Octane silicon drift detector X-ray energy dispersive spectrometer (EDS). This EDS detector collected the characteristic X-rays for chemical analysis and was calibrated using virgin Inconel 718 powder as the reference sample.

The JSM-7600F electron gun source uses field emission (Schottky emitter) to produce electrons. These electrons are then guided down the electromagnetic column by a series of electromagnets that focus and direct the beam towards the sample. The electrons then interact with the intended sample producing multiple signals which can be collected and analyzed by examining the secondary electrons or the back-scatter electrons.

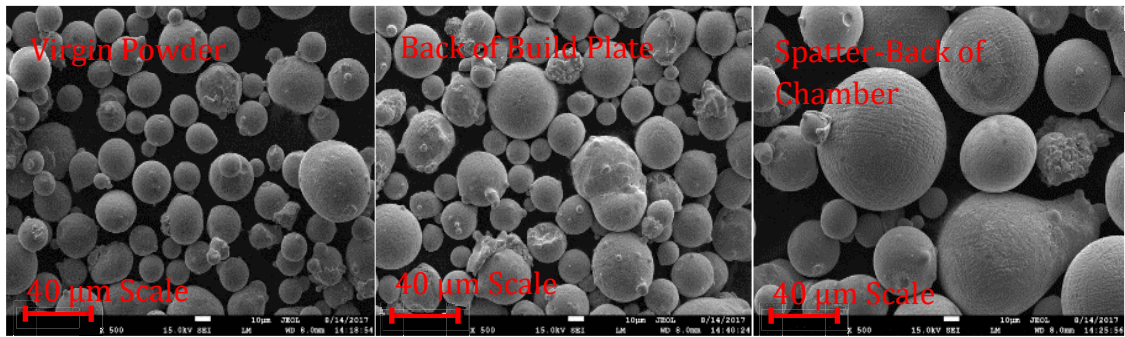


Figure 6: SEM Images from Virgin, Zone 2, and Zone 3 Powder

Figure 6 shows the corresponding SEM images taken utilizing secondary electron imaging with 15.0 kV at 500x. The results from the virgin powder (left), zone 2 powder (center) and powder collected from zone 3 (right) are shown. Of note is that in zone two, while the particles are similar in size a significant amount of abnormal non-spherical features are present which are likely due to “splashing” of molten metal landing on them during the lasing process. This increase could result in powder not spreading uniformly on reuse in subsequent builds but is beyond the scope of this study. Additionally, zone 3 powder appears to be significantly larger and a very spherical nature. This could be due to the solidification that happens while the particles are in flight and the decrease in aerodynamic drag during this process.

During the JOEL JSM-7600F SEM imaging process, an Octane silicon drift detector X-ray energy dispersive spectrometer (EDS) was used to gain an initial insight into the oxidation

of the particles. This was believed to be relatively low due to the material being Inconel 718 and the chamber atmosphere being held at or below 0.01% oxygen. A sample analysis of the virgin powder is shown in **Figure 7**, with all of the oxygen analysis results being shown in **Table 1**. This powder was used to gather a baseline for the spatter particles. It is understood that this was a surface measurement and was intended to only gain a superficial understanding as to whether there was a drastic change. Surface oxidation of the sample could also take place if the sample was exposed to normal atmospheric conditions for extended periods of time. Samples were treated similarly for this experiment and therefore a cursory relative comparison was performed. These results showed an increase in surface oxidation by 3% in the spatter (zone 3) group verse the virgin powder and zone 2 (back of build) groups. One hypothesis for this could be due to the increased interaction with atmosphere due to a longer time of flight but further analysis with more accuracy would need to be performed and is outside the scope of this analysis.

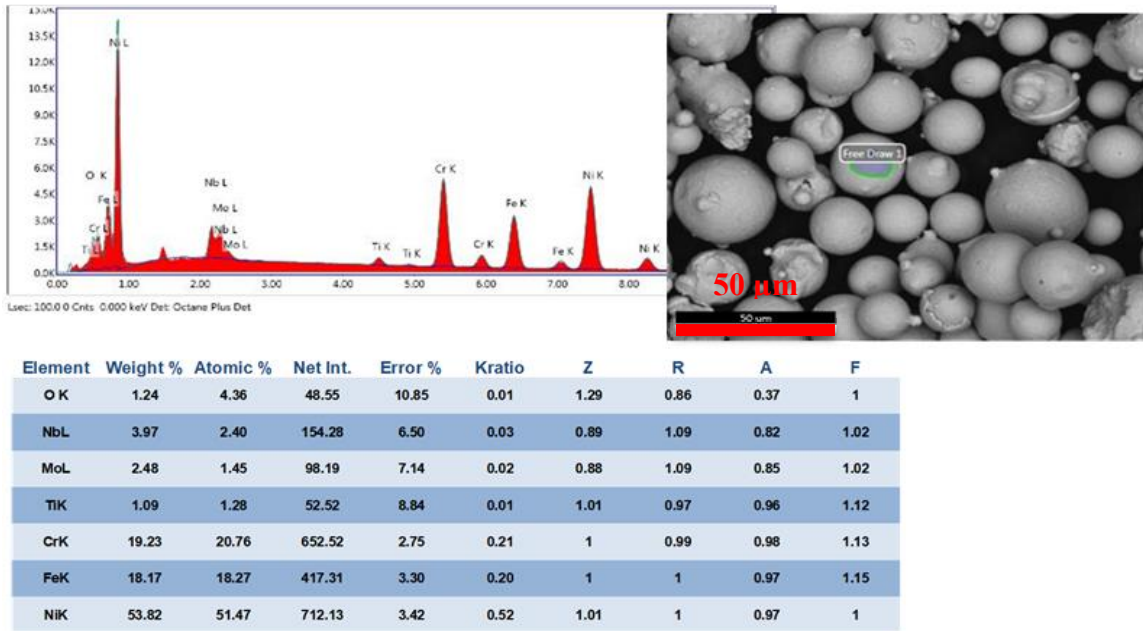


Figure 7: SEM EDS Analysis of Virgin Inconel 718 Powder

Table 1: Surface Oxidation Analysis of Virgin, Zone 2, and Zone 3 Powder

Weight Percent Oxygen in Samples			
Sample	Virgin	Back Ledge of Chamber	Back of Build Plate
#1	1.24%	6.20%	1.32%
#2	1.36%	3.22%	1.14%
#3	1.32%	1.11%	0.99%
#4		5.88%	
Avg	1.31%	4.10%	1.15%
StDev	0.0499%	2.0792%	0.1349%

2.1.3 Optical Microscopy and CT Analysis

The metal cylinders from each of the corners of the build were sent to be analyzed by CT scanning to determine overall porosity, while the adjacent samples were ground and polished to be analyzed by optical microscopy. CT analysis was performed by Penn State University with a voxel size of 20 μm which translates into a minimum feature resolution of 40 – 60 μm . Optical microscopy was done with a magnification of 50x as shown in **Figure 8**. As suspected, the samples created in the back of the build chamber, which had spatter impact it during the build process, showed an increase in porosity when compared to the samples created in the front of the build chamber. Also, clearly visible was a difference in porosity with samples lasered before spatter impacted the layer (left side of the build) versus the samples which were lasered after spatter impacted the layer (right side), **Figure 8** and **Figure 9**. One hypothesis is that the large particles can be brushed off the samples during the recoating process and drastically reduce the porosity.

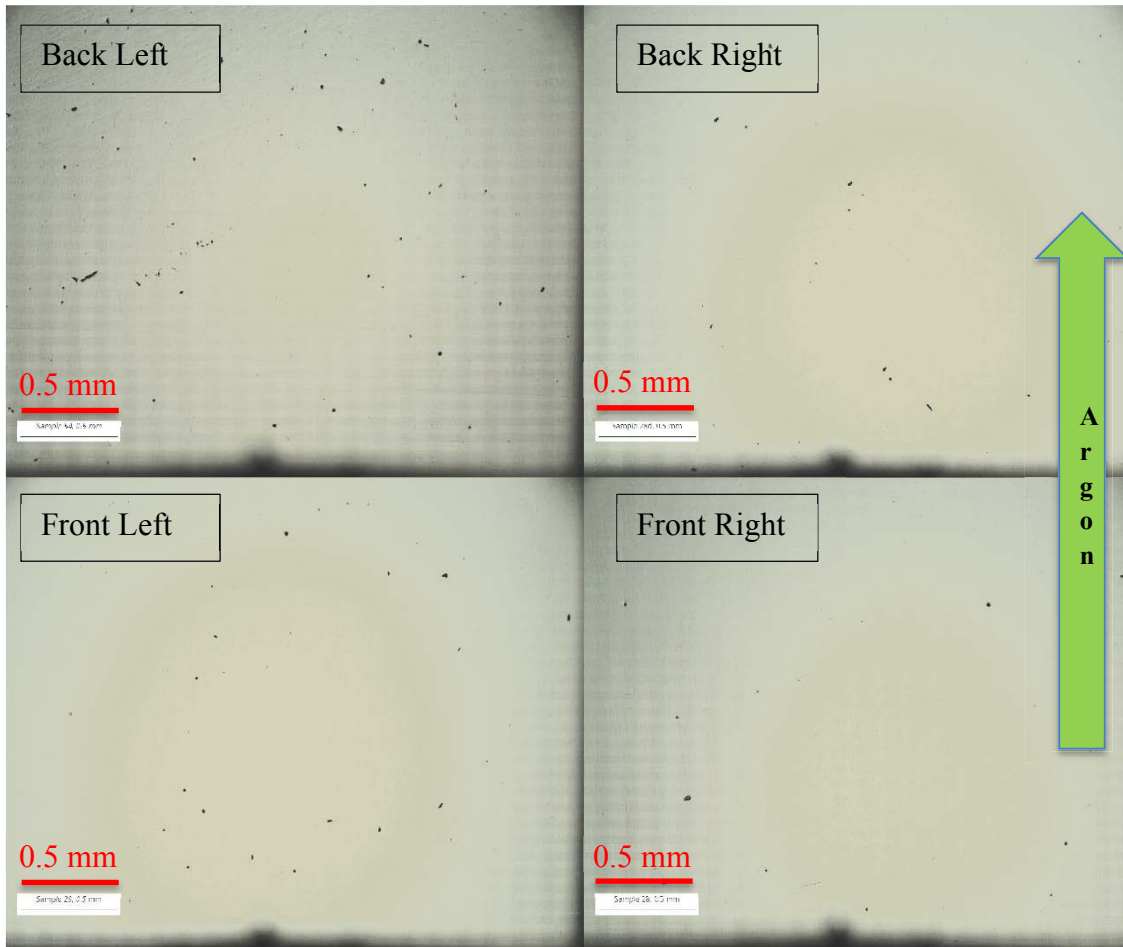


Figure 8: *Optical Microscopy Images from Inconel 718 Samples Taken from the Respective Corners of the Build Plate at 50x Magnification*

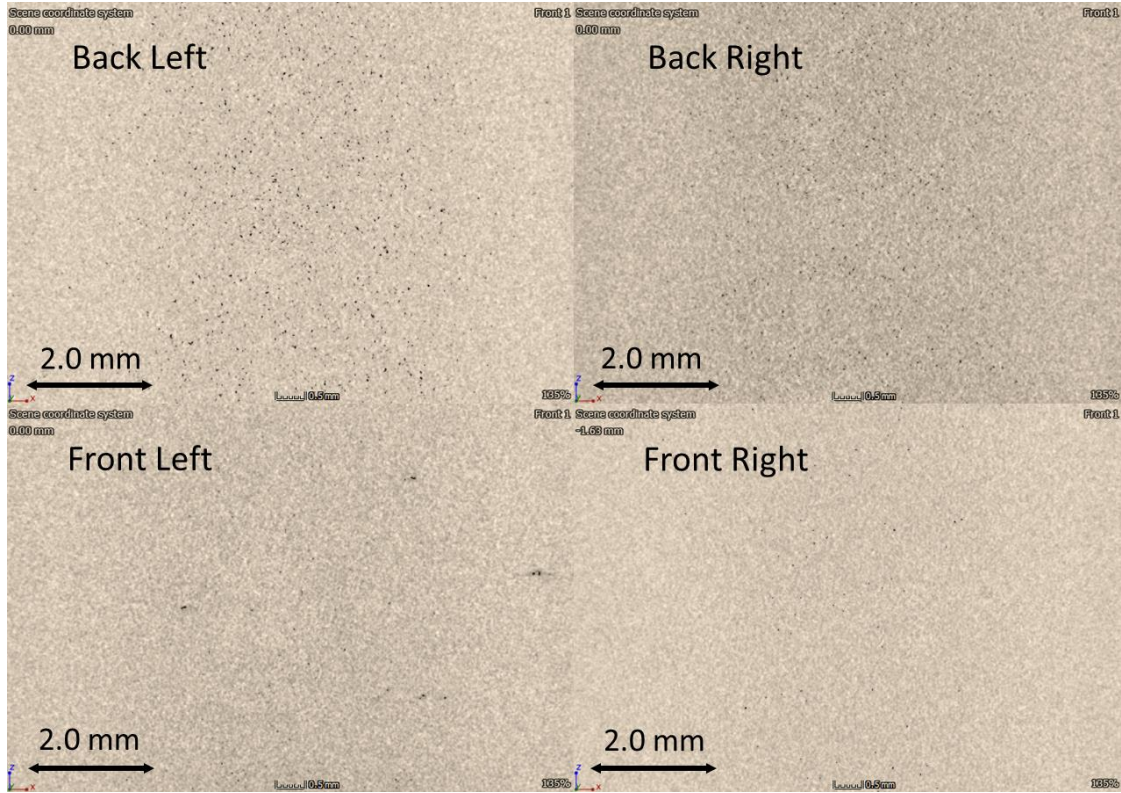


Figure 9: CT Analysis Images of Inconel 718 Samples Taken from Respective Corners of the Build Plate

2.1.4 Mechanical Testing Results

Tensile specimens were built using Inconel 718 according to ASTM E8-16a for a subsize specimen [92]. Specimens were printed in the ZX orientation and in the order of back of the build plate to front against the argon flow (optimal order). Testing (performed by Westmoreland Mechanical Testing & Research, Inc.) was done on the specimens as built without a post processing heat treatment and was done at room temperature with a speed of 0.005 mm/mm/min. The percent elongation was measured using the before and after gauge length measurements, results are shown in **Figure 10**. As can be seen the difference between the samples were negligible which corresponds well to the microscopy and CT images which should little difference. Further testing would be needed to fully analyze all

potential differences, specifically specimens built in the non-optimal order (front to back instead of back to front), and with various heat and HIP post processing steps.



Figure 10: Tensile Specimen Results for Inconel 718 Built in the Optimized Order

2.2 High Speed Camera Requirements Experiment

To determine the range of frame rates needed to appropriately track the spatter particles while limiting data requirements, a series of high speed videos were recorded utilizing various frame rates (frames per second, fps), shutter speeds (SS), and ISO values (a measure of

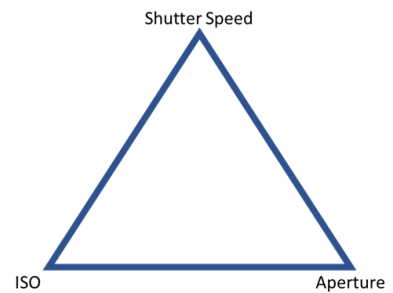


Figure 11: Camera Variables to Optimize Image

the camera's sensitivity to light), and aperture. The main variables which can be altered to gain a good image on a typical camera are SS, ISO, and aperture. The tradeoffs are

represented in a triangle, **Figure 11**, as each either restricts the amount of light capable of reaching the camera sensor or decreases the sensitivity of the camera sensor. Most photography is based on a careful balance of these three to gain the optimal resolution for the image desired. Additionally, in order to handle the increased speed rates, high speed cameras often using only small areas of the sensors when capturing the data in order to be able to save the frames fast enough, which further restricts the camera of resolution by only capturing the center of the field of view, thus resulting in a more pixelated reduced video area (more zoomed in). **Figure 12** and **Figure 13** show an image taken at 1000 FPS and one taken at 5000 FPS and highlights the difference in the area of focus and light allowed into the build. The 5000 FPS image also had a corresponding faster shutter speed which is why the spatter appear spherical instead of streaking as in **Figure 12**.

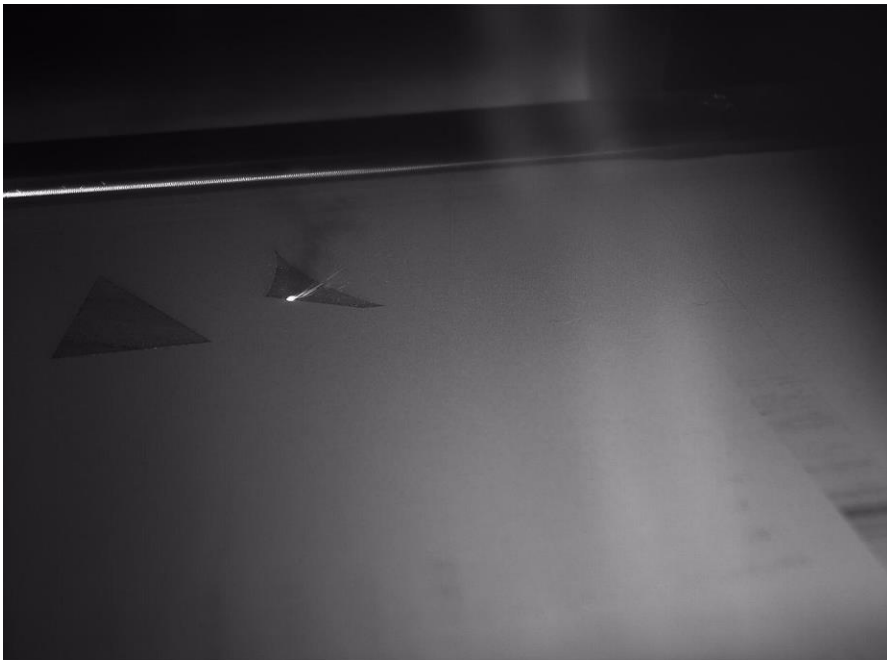


Figure 12: Image of Video Taken at 1000 fps and 200 μ s Shutter Speed



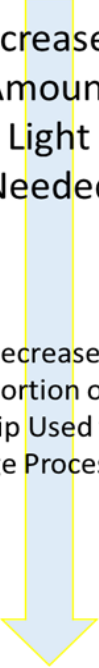
Figure 13: Image of Video Taken at 5000 fps and 129 μ s Shutter Speed

After taking video at various speeds with various shutter speed, a determination was made that a frame rate of 1000 to 2000 FPS would be sufficient, and a similar shutter speed would additionally be sufficient. Increasing the shutter speed allowed for the particles to appear as spheres in the frames; however, this limited the light entering the camera which resulted in a dark low-resolution video. Decreasing the shutter speed made the particles appear as streaks in the frames, **Table 2**. After further inspection, these streaks were determined to be beneficial as it allowed for greater ease in tracking and determining the spatter direction, velocity and age. Due to this added benefit, and the benefit of increased resolution, a slower shutter speed was determined as enough. Based on these results, two low cost, high speed cameras were purchased with a set 1000 fps frame rate and a 500 μ s shutter speed (50% of the frame rate).

Table 2: High Speed Analysis Results Showing Chosen fps/Shutter Speed

High Speed Video Trade Offs		
Frames Per Second	Shutter Speed	Observations
500 FPS	200 μ s	Large Gaps in frames (difficult to track spatter), Great Resolution, Small File Size
1000 FPS	200 μ s	Poor View of Individual Spatter Particles (Smearing), Good Resolution, Small File Size
2000 FPS	200 μ s	Decent View of Individual Spatter Particles (Minor Smearing), Good Resolution, Manageable File Size
3000 FPS	200 μ s	Decent View of Individual Spatter Particles, Decent Resolution, Large File Size
5000 FPS	129 μ s	Good View of Individual Spatter Particles, Poor Resolution, Large File Size
7500 FPS	100 μ s	Great View of Individual Spatter Particles, Poor Resolution, Very Large File Size

Increased Amount Light Needed



Decreased Portion of Chip Used for Image Processing

3.0 Publication One: Micron-level Layerwise Surface Profilometry

Micron-level Layerwise Surface Profilometry

to Detect Porosity Defects in Powder Bed Fusion of Inconel 718

Chris Barrett¹, Eric MacDonald^{1*}, Brett Conner¹, Fred Persi²

¹Youngstown State University, Youngstown, OH 44555

²Grale Technologies, Youngstown, OH 44510

Abstract

Additive Manufacturing enables a fabrication freedom and is transforming the manner in which high value and high performance structures are created. The aerospace industry stands to benefit from structures in which the weight is minimized, the materials provide good mechanical properties at extreme temperatures and a swarm of distinct parts can be consolidated into a single non-assembled complex structure. However, for additive manufactured parts to be used in flight-critical applications, the quality of the resulting fabricated parts must be well understood in light of the lack of flight heritage. As additive manufacturing is performed layer-by-layer, new opportunities exist to monitor the fabrication *in situ* and non-destructively and to provide a qualify-as-you-go paradigm. In this study, a high-resolution laser line scan profilometer is used just after a layer has been selectively melted and the sensor is mounted to the recoater arm to provide unobtrusive and inexpensive access to the top of the powder bed. The driving hypothesis of the effort was that fused and unfused powder would lie at different elevations as the fused powder volume would consolidate and therefore become depressed. Consequently, this

measurement could both verify the intended geometry and also identify any lack of fusion defects. Furthermore, some preliminary anecdotal evidence is shown that spatter can also be identified and thus profilometry can inform the minimization of contamination (build chamber argon flow, build layout strategies, etc.)

1.0 Introduction

Powder Bed Fusion (PBF) shows promise in the aerospace industry for providing complex structures spatially tailored for both performance and weight and fabricated with high performance metal alloys. Large groups of interrelated parts can now be consolidated into a single non-assembled structure, with geometries not possible previously. However, for this next generation of manufacturing technology to be more widely adopted, an *in situ* evaluation methodology is required to provide rigorous evidence of the reliability of the consequent structure - particularly in the context of the high standards of the aerospace industry. Given the layer-by-layer processing which provides access to the top surface of the structure during fabrication, a layerwise digital signature for each fabrication can be measured in an unprecedented manner. This signature per layer now enables a *qualify-as-you-go* paradigm in which the quality of a structure can be judged comprehensively in three dimensions.

Within the taxonomy of PBF, Selective Laser Melting (SLM) has been optimized to create complex, high performance geometries in a diversity of metal alloys; however, process monitoring is conspicuously absent in production systems and remains an open question. A need for highly accurate, real-time 3D metrology for layer-wise monitoring is necessary to increase the confidence in the fabricated structures - particularly in safety critical

applications. New metrology techniques exist including laser line profilometry, which can be integrated within AM systems unobtrusively - providing micron-level surface maps of the structure under fabrication layer by layer. A collection of 2D surface maps can provide new insights into the quality of a 3D fabricated structure, while the structure is otherwise obscured within the powder bed. The integration of the sensor mechanically on the recoating arm of a laser scanner allows for inexpensive access across the entire powder bed both before and after powder re-coating. The original hypothesis of this work is that *in situ* metrology using laser scan profilometry may provide geometry verification, and the necessary feedback to enable remediation in subsequent layers in order to subvert defects detected in an earlier or current layer.

1.1 Previous Work of Others

The premise of this effort is that a difference in elevation exists between fused and unfused powder, and the absence of fusion may be intentional (outside the volume of the printed structure) or unintentional (lack of fusion defect). In laser powder bed fusion processes, powder is added to the build volume one layer at a time through a recoating process usually involving spreading of powder by a recoater blade. Unless there is powder shorting, the powder is evenly spread and packed closely (with space existing between contacting powder particles). Once the laser melts the powder, the melted region will be fully dense and will therefore be depressed as compared to the surrounding unmelted powder. Experiments using digital fringe projection by Land *et al.* [93] on laser powder bed fusion of alloy IN625 have shown elevation reductions of the melted powder by 0.1 to 0.2 mm compared to the surrounding powder.

Laser powder bed fusion can produce several types of defects including lack of fusion [2], keyholing[49], balling[25], spatter[27], residual gas porosity [6], hatching strategy defects and recoater defects [7-8]. [53] provides a good overview of *in situ* and non-destructive evaluation. Several types of microdefects would produce higher elevation than the surrounding fused metal and would be detectable by a laser line scanner. Certain lack of fusion defects can impinge the surface of the melted solid and leave unmelted powder above the melted surface. Lack of fusion can result from combinations of absorbed power, laser travel velocity, powder layer thickness, and hatch spacing. Lack of fusion can also occur with inadequate overlap between hatching and contouring resulting in unfused region [7]. If lack of fusion is sufficiently large enough or if powder can fall into the porosity region then a depression may occur instead.

Spatter particles ejected from the melt pool can land on the melted part. These particles can be much larger than the D90 size of the powder size distribution [25,27,62]. As a result, the contaminate particles should be detectable by the laser line scanner. Large spatter particles are a concern because they can cause light damage to the recoater blade and the spatter particles might not melt during the subsequent laser pass (a process which is optimized for smaller powder size distribution). Even though the surrounding powder can melt, this can give rise either unfused regions or create a cavity around the particle. Spatter can also land in unfused powder and change the local powder packing density and chemistry - either of which can affect melting behavior due to particle size differences.

In the case of too much absorbed laser power and simultaneously too much travel velocity, balling of the melt pool can occur with an uneven swelling topology on the melted surface. The melt track can break up into “balls” due to the Plateau-Rayleigh instability (balling).

Changes in local powder conductivity and surface tension affect the onset of this phenomenology [4]. The authors hypothesize that this defect can be detected by surface profilometry. Several defects that would not be detected by the proposed approach include keyholing, lack of fusion at the overlap of melt pool roots, and trapped gas porosity - all of which would be embedded into the part below the top surface and therefore undetectable by the laser line scan technology.

In situ monitoring with the ultimate goal of providing feedback control has been researched in a variety of manners - but none published that included the direct use of laser scanning profilometry - capturing high resolution surface maps after each layer. [11-16] all investigated monitoring the process at the melt pool by monitoring the size, shape and temperature. The melt pool behavior is the essence of SLM and clearly is critical to understanding the quality of a fabrication; however, the work described here is differentiated by focusing on detailed surface maps between layers with micron-level resolution with the objective of identifying lack of fusion defects. The measurements are less direct but more global in nature and thus may provide insights overlooked otherwise. [17-20] monitored and tracked the scan path - again focusing on the melt pool process but across each layer. [7, 21-25] all considered layer-by-layer monitoring but did not include laser scanning and Foster included developing and using an open source protocol. [26-27] monitored the powder bed surface which is similar to the current effort; however, the current work maps the surface with higher resolution scanning and although the powder bed is monitored as a side effect, high definition monitoring of the selectively melted structure and comparison against the intended geometry is the key element. This effort is intended to inform the process by measuring actual geometry and surface finish, identifying

spatter contamination, and potentially locating areas of the surface that are intended to be melted and are not and vice versa - all of which will provide feedback for closed-loop control as well as provide a *qualify-as-you-go* quality assurance methodology.

Macro defects can also be detected by the laser line scanner. Super elevation of a part or part features results from inadequate support [51]. Residual stresses deform the inadequately supported part (even to the point of breaking supports away from the build plate) and regions of the part will stick out above the recoated powder layer. Features caused by a recoating error can also be discerned by the laser line scanner. Gouges or ridges in the powder can result from nicks blades or adhered particles on the blade. Some recoaters might bounce and flick powder if an elevated feature is struck.

On March 29th, 2018 a week before the submission of this article, the authors attended a presentation delivered by Adam Hicks from the University of Dayton Research Institute in which Hicks described a similar and independent research effort using *in situ* surface profilometry for detecting defects in powder bed fusion. After the presentation, Hicks mentioned to the authors that other groups were also independently investigating the concept. [28] describes a NASA-funded Small Business Innovation Research (SBIR) project executed by Flightware, Inc. (Guilford) in collaboration with EWI (Columbus). However, to date, no work has been published in open literature to the authors' knowledge.

2.0 Methods and Materials

A laser line scan profilometry system was bracketed on to the recoater blade of a 3D Systems (Rock Hill) ProX 320 selective laser melting system. The system scans the selectively melted top surface prior to new powder being deposited. This high resolution surface map for each layer of the fabricated structure captured *in situ* can enable a *qualify-*

as-you-go qualification paradigm. In this study, Inconel 718 powder was primarily used but the concept should apply to other material systems, AlSi10Mg was utilized in some initial testing. The main purpose is to identify lack of fusion defects in what would otherwise be melted regions. However, the concept could also verify intended geometries and capture excessive spatter contamination - hypothesized to include larger particles that would adversely affect subsequent layers.

2.1 Laser Scan Profilometry and Recoating Carriage Mechanism

A Keyence (Osaka) model LJ-V7060 profilometer was mounted to the top of the ProX 320 DMP printer's recoater arm to provide micron-level surface mapping either before or after the recoating of the next layer of powder. **Figure 14** shows the system (left), the build chamber (center) and the top of the powder bed with the scanner activated (right). The laser scanner spans only a small fraction of the powder with 15 mm scan width but a sufficient fraction to allow the evaluation of the technology for detecting of lack of fusion defects. Potential future work will include spanning the entire length of the recoater with sensors to provide full visibility, however, utility exists in just measuring a fraction of the bed to provide a representative view of the entire build. The design used for all experiments was within the reduced field of view of the scanner. An extension of the scanner is clearly unhindered mechanically in the ProX along the recoater blade but would result in additional expense of more line scanners or scanners optimized for wider scanning. For the purposes of this work, a single 15 mm of scan width was sufficient to test the effectiveness of the *in situ* process monitoring.

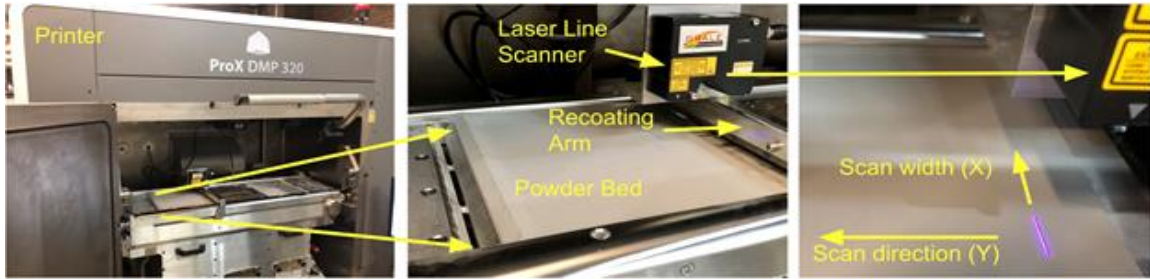


Figure 14: Laser Scan Profilometer Bracketed on ProX 320 Recoating Arm

2.2 Benchmark Design with Inserted Intentional Defects

A layer was designed that was repeated for 10 layers. The layer design included geometries that allowed for a design of experiments with inserted defects which explored defect size and orientation relative to the profilometry path (**Figure 15**) in part inspired by [29]. Intentional defects were inserted into the plate in two references: positive (fusion in a field of no fusion) and negative (absence of fusion in a field of full fusion - simulating lack of fusion defects). Additionally, a one-millimeter scale bar was integrated into the design to provide spatial context across the profilometry path. Although the Z axis precision provided by the scanner (measuring elevation along the scan width) maintained micron-level repeatability, one challenge for the proposed parasitic scanning approach was the imprecise knowledge of the location of the recoater blade (Y axis) as the scanner was bolted to the top of the recoating arm. Traditionally, recoating requires even pressure to be applied to the blade as each subsequent layer of powder is deposited on the existing powder bed and the knowledge of the recoater blade location is not necessary for maintaining even and effective recoating (the recoater displacement is generally meaningless to the recoating process as long as the blade fully traverses the entire powder bed surface).

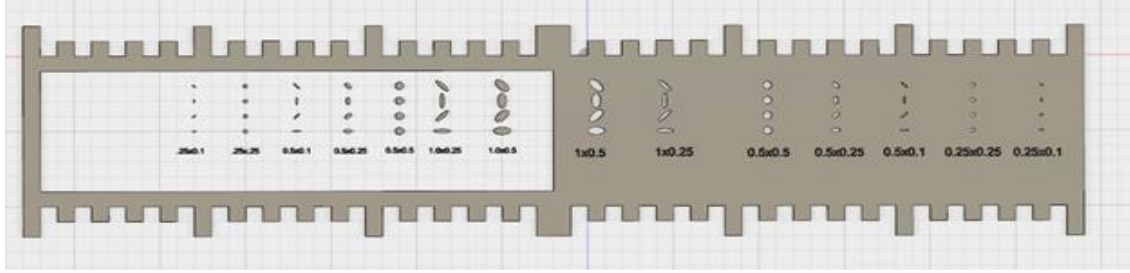


Figure 15: Experimental Design: Intentional Negative and Positive Defects with Ruler Bar

3.0 Results and Discussion

The reference design was built, and each layer was scanned just prior to the recoating action - before the previous layer was obscured with a new layer of powder. The part was built for 10 layers and at least one scan was captured per layer.

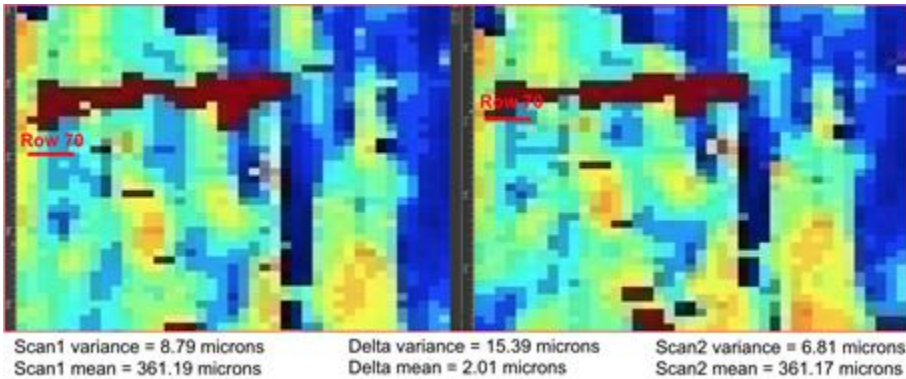
3.1 Carriage Location and Scan Map Repeatability

After collecting repeated layer data, inconsistency in the recoater speed was identified as a major problem for providing repeatable surface maps. The recoater blade traversed the powder bed with nonregular motion that rendered the exact location of the blade and sensor impossible in order to establish the correct location of capture line data. Scanning a surface map while piggybacking parasitically on the recoater requires precise knowledge of the location of the recoater and has a profound impact on the quality of the resulting surface data. Approximate positions were calculated assuming a uniform velocity of the recoater, but it is evident from the data that small variations are noticeable. For the purposes of this evaluation, a fiducial ruler was included in the design so that machine vision software (after the scan) could re-calibrate the location of the recoater arm during recoating. Future work will include additional location measurement (e.g. distance measured from the carriage to the side of the build chamber with a precision linear encoder) to identify the precise Y

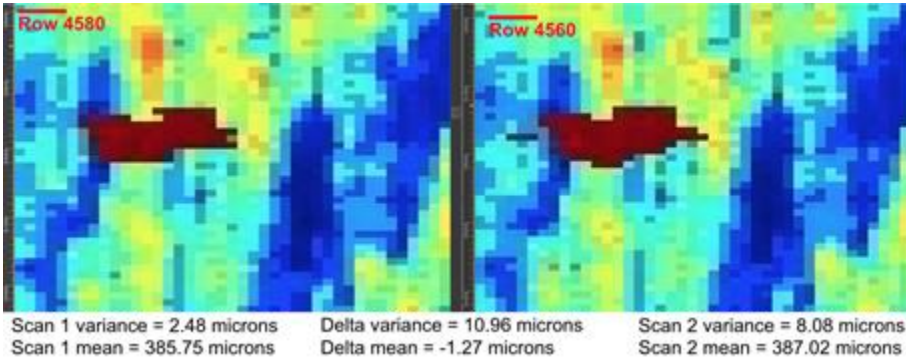
location of a laser line scan without the need for unnecessary fiducial features and to accommodate general designs.

To evaluate repeatability of the surface maps, local windows were compared in terms of pixel difference, variance and image correlation. When confining the comparison of data to small local regions (40 pixels by 40 pixels - approximately 0.8 mm per side), the data was repeatable and accurate for multiple scan runs on the same unmelted powder bed. Unmelted powder was used for this comparison as the variance is the lowest for uniform powder - the worst-case for repeatability. **Figure 16** shows a comparison of three different local windows of the powder bed (scanned twice) to evaluate the repeatability of the measurement. The powder bed appeared uniform and planer to the casual observer, but with high resolution surface maps, interesting features became obvious and were matched in the two separate scans. Three local regions were identified at the beginning, middle and end of the full scan extending a total of 300 mm. The local windows were manually registered with the aid of correlation analysis. Correlation analysis calculated a score of similarity as one window was slid across the other and the average pixel difference was calculated. The location of lowest score was considered the registered location. Once registered, the pixel differences of each of the pairs were performed and a mean and variance were calculated. For the pair A, the pixel difference average was 2.01 microns with a variance of 15.39 microns, for B, the values were 1.27 microns mean with 10.96 microns variance and finally for C the values were -0.23 and 2.76 microns. The three map pairs highlight the close resemblance and correlation across the scan albeit with the locations of each region at different row ranges (one reference row shown in red in each of the six scans) from the previous scan due to the accumulated error in recoater position. As

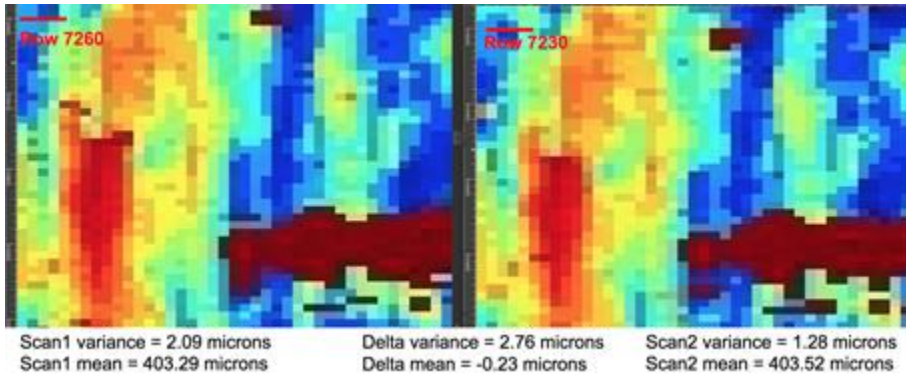
the defect detection algorithm is executed in a local context, global registration is not necessary; however, to eventually confirm with pixel-by-pixel comparisons that the powder fusion matches the expected design geometry, the global registration will need to be addressed and this is the focus of future work.



(a)



(b)



(c)

Figure 16: Repeatability Analysis Study with Variance

Figure 16 shows a repeatability analysis based on comparing pairs of local 40 x 40 pixel regions across two different scans of the same unmelted powder bed. **Figure 16** a, b, and c are pairs of measured maps which were registered based on obvious features and correlation analysis of the powder bed surface. The scale is normalized between the minimum and maximum values.

3.2 Optical Verification of the Intentional Defects

As defects were intentionally integrated into the design, these small features had to be verified optically to ensure that the intended geometries were as planned. These measured dimensions were then compared against scan data to evaluate the effectiveness of defect detection by the *in situ* surface mapping. The results of the optical microscopy showed good correlation with the 1.0-millimeter scale marks and the large features; images were taken absent of powder (**Figure 17**). However, smaller features like the numbering scheme were notably absent as they were beyond the resolution capabilities of the printer (**Figure 18**).

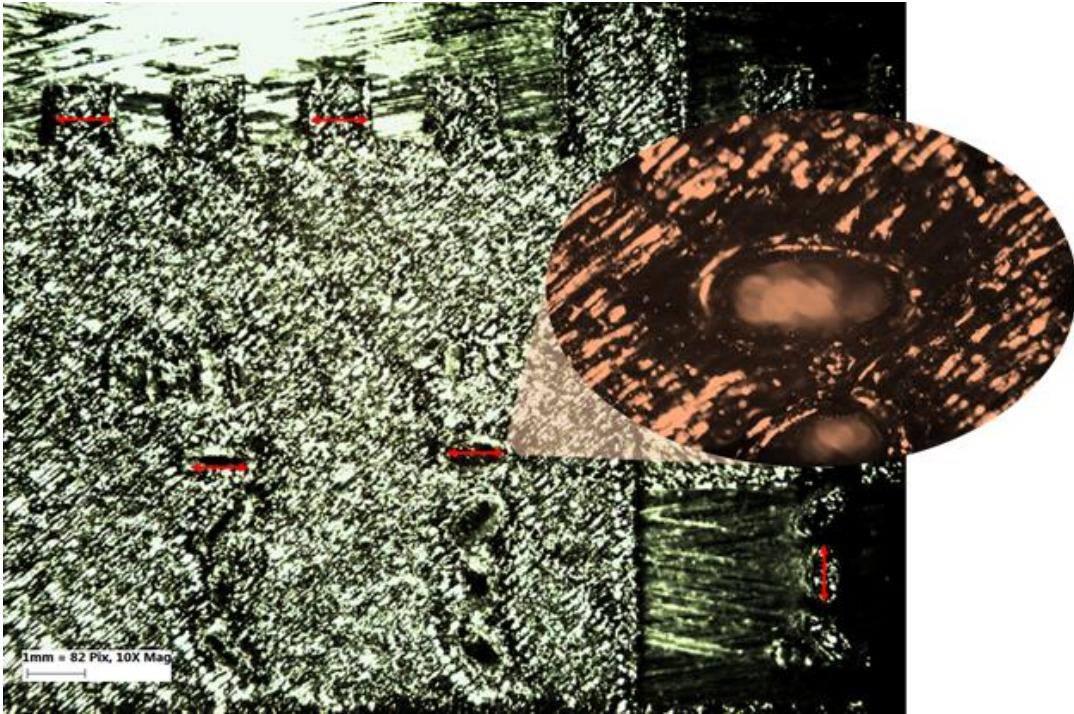


Figure 17: Optical Verification of the Defect Simulations in Inconel 718

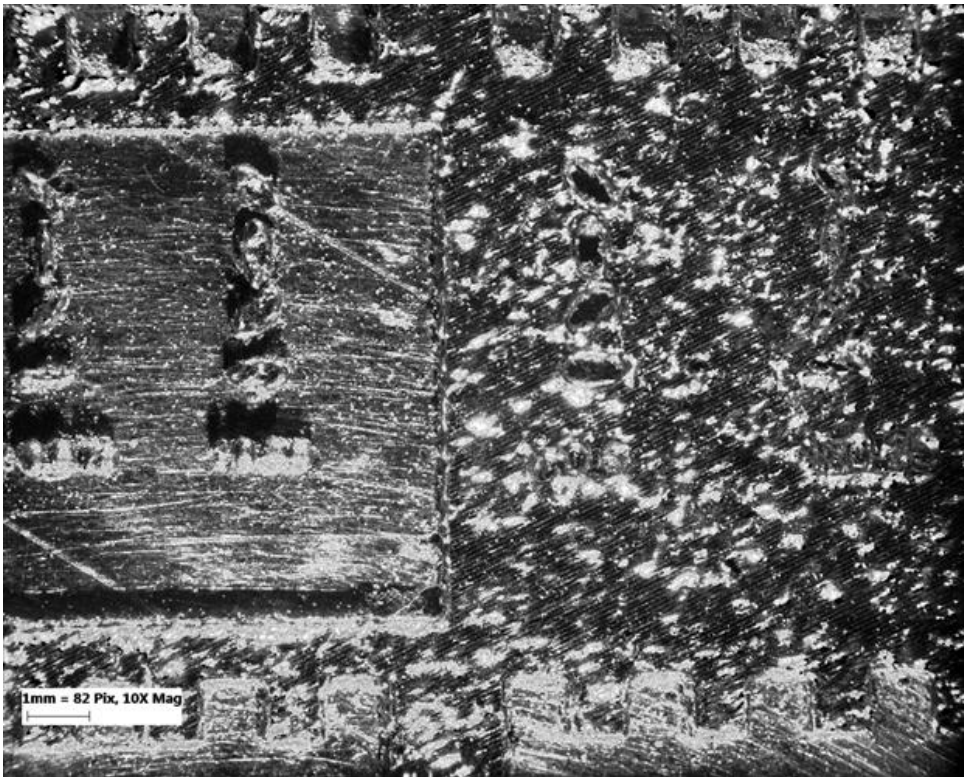


Figure 18: Optical Verification of Defect Simulations in AlSi10Mg (note poor numbering resolution due to printer).

3.3 Detection of Lack of Fusion Defects

As layers were built (each with the identical and repeated benchmark design), the basic depth data was collected with the driving hypothesis that unmelted powder would maintain a high Z-axis value (more elevated) and that melted sections would consolidate and shrink providing lower depth values. By monitoring the depth, lack of porosity defects should become manifest with the unfused powder providing higher surface values. Other mathematical algorithms were explored on each scan in hopes of improving the signal that could enable discrimination between fused and unfused powder. These algorithms included (a) the depth values directly, (b) the variance of the map with a five-by-five pixel sliding window and (c) the variance in both the X and Y direction for the same window. The raw elevation data appears to be the most promising. **Figure 19** illustrates the raw depth data representations of the surface map and although the surface maps were not perfectly aligned with the original benchmark surface (**Figure 15**), a signal became apparent and could be potentially optimized for geometry verification as well as for the eventual purpose of identifying lack of fusion porosity. In the case of the lack of fusion, the ultimate goal would be to identify regions in the design that may require additional selective laser melting energy (defect remediation) to ensure high mechanical performance of the final structure. **Figure 20** shows the windowed variance of the same scan.

The intentional defects were identified in the scan but as the actual size of the defects were larger than targeted, the defects were obvious; however, the general concept of differentiating between fused and unfused powder layer by layer was successfully demonstrated. Future work will continue investigating a wider range of sizes, shapes and

orientations of intentional defects as well as intentionally using bad build parameters to cause defects through the process itself.

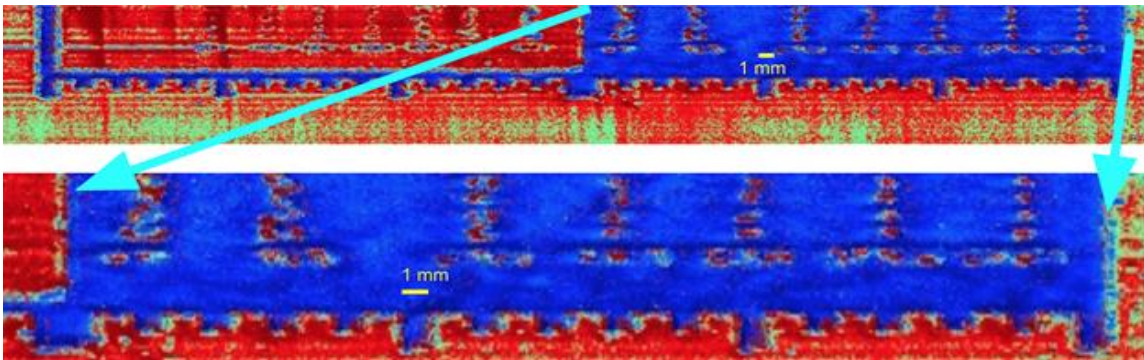


Figure 19: Single Scan of the top surface directly after the 9th layer, high elevation in red and depression in blue

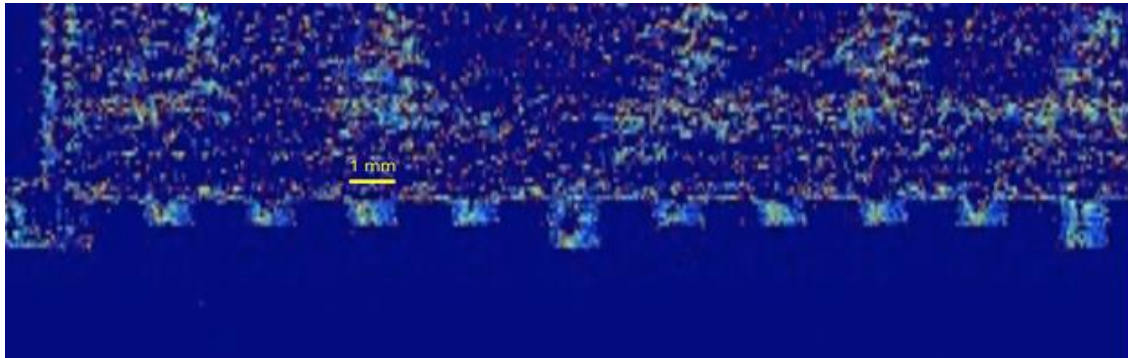
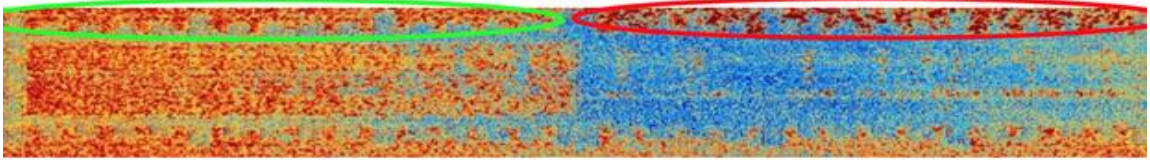


Figure 20: A 5 x 5 Pixel sliding window variance of the scan in **Figure 19**. Note the low variance in the lower powder region

3.3 Detection of Spatter Contamination on the Powder Bed and other Melted Surfaces

As a flow of Argon is pushed from the front of build chamber to the back, generated spatter from the melting was expected to be ejected and pushed behind the current build geometry. However, if many builds were packed into the bed, spatter from front-positioned structures could land and affect the quality of back-bed structures. The *in situ* surface profilometry could be used to detect excessive amounts of landed spatter on critical components. Although this work did not focus on collecting this data, anecdotal evidence was seen as

the powder bed behind areas with significant melting with negative defects (right side of **Figure 15**) appeared to have more variance and higher average elevation than behind the section of the experiment with positive defects in a field of unfused powder (left side of **Figure 15**). **Figure 21** shows some examples of this effect within the limited view that is provided behind the design.



***Figure 21:** Increased height donated by red coloring, shows increased likelihood of spatter contamination at the top of the scan.*

3.4 3D Visualization and Detection of recoater flaws

In addition to 2D imagery it is possible to view the scanned surface layer in three dimensions (**Figure 22**) by converting image pixels into 3D points and then constructing a rasterized mesh of triangles with these points as vertices. Red (blue) shows higher (lower) elevations. The largely powder area with positive defects is shown in the upper half, and the melted region of negative defects is in the lower half. The 3D mesh contains essentially the same information as the 2D image, but it is an additional visualization tool that aids in exploring algorithms for filtering, smoothing and ultimately discriminating between melted and unmelted regions. For example, evident in the isometric view is that the transition area between fused metal and powder appears rougher or slightly more varied in height. It is not known yet to what extent this is physically accurate or represents a measurement artifact induced by sharp changes in reflectance as the laser sensor passed between the two surfaces.

Note the presence of fine lines that traverse the build area longitudinally (most apparent in the flat region at the far top). These tracks likely represent small nicks in the plastic recoater wiper. One of the noticeable tracks (approximately a third the way in from the right) lines up with the labels for each set of induced defects and was probably created by repeated scraping across this highly irregular surface patch. As already pointed out, while the intention was to print labels to facilitate defect identification, the resolution of the ProX 320 was insufficient to preserve this fine detail, creating uncharacteristically rough features that likely led to premature wear of the recoater blade in this area. Irregularities in the recoating step that may lead to build defects should be detectable by profilometry.

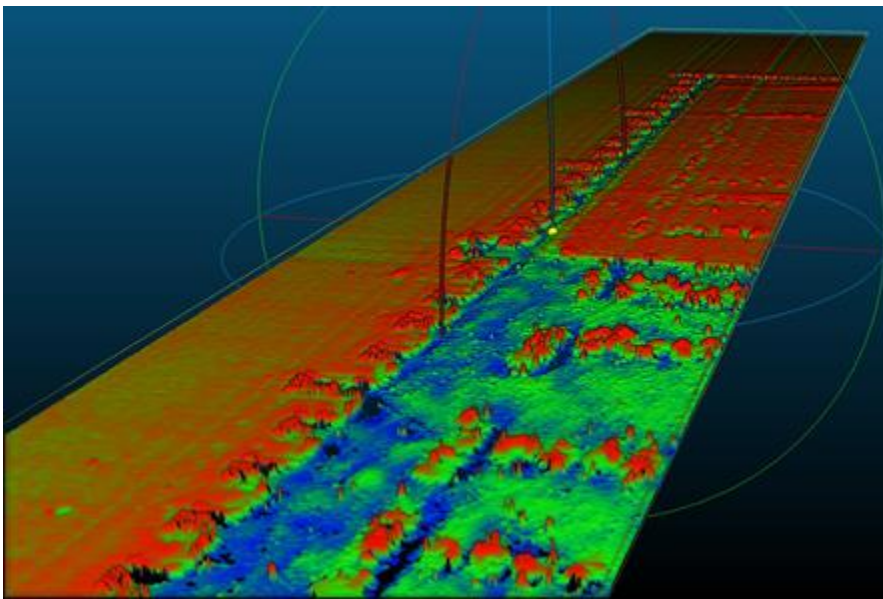


Figure 22: 3D Isometric view of surface layer, showing both positive and negative defects, and possible recoater flaws

4.0 Conclusions

The experiment described demonstrates that laser scan profilometry that is unobtrusively integrated into a ProX320 selective laser melting system can effectively improve quality of fabricated structures by providing a digital signature for each layer. The sensor rides

parasitically on the recoater blade, providing an economical solution for sensor integration. The sensorized system can provide many benefits including verifying intended geometries and detecting specific types of defects with the potential to provide subsequent defect remediation. This work focused on lack of fusion defects with an experiment that simulated a variety of these types of defects and the method made manifest the defects. Other defects were also posited--including spatter contamination, for which preliminary evidence was shown.

Acknowledgments

The work was supported by the US Army Aviation Applied Technology Directorate via grant W911W6-17-C-0048 and was made possible with the assistance and cooperation of M-7 Technologies (Youngstown).

4.0 Publication Two: Low Cost, High Speed Stereovision

Low Cost, High Speed Stereovision for

Spatter Tracking in Laser Powder Bed Fusion

Christopher Barrett, Carolyn Carradero, Evan Harris,

Jeremy McKnight, Jason Walker, Eric MacDonald, Brett Conner

Youngstown State University, Youngstown, OH 44555

Abstract

Powder Bed Fusion Additive Manufacturing affords new design freedoms for metallic structures with complex geometries in high performance materials. The aerospace industry has identified the inherent benefits of AM not just in terms of shape creation but also with regard to producing replacement parts for an aging fleet of aircraft. However, for these parts to be deployed in flight-critical applications, the quality must be well established given the lack of flight heritage for the manufacturing process. As additive manufacturing is executed layerwise, opportunities exist to non-destructively verify the fabrication *in situ* with a qualify-as-you-go methodology. In this study, a pair of low cost, high speed cameras are integrated and synchronized together to provide stereovision in order to identify the size, speed, direction and age of spatter ejected from the laser melt pool. The driving hypothesis of the effort is that behavior of spatter can be reliably measured in order to determine the health of the laser process and ensure that spatter is not contaminating the build. Feasibility demonstrations are shown that describe how the measurements are made and characteristics calculated from the image data and how the data were verified with alternative measurements. Opportunities, future work and challenges are discussed.

1.0 Introduction

Powder Bed Fusion (PBF) shows promise in the aerospace industry for providing complex structures fabricated with high performance metal alloys that are spatially tailored for both high performance and low weight. Interrelated assembly parts can now be consolidated into a single non-assembled structure with geometries not possible previously. However, in order to broaden industrial adoption in light of the high standards of the aerospace industry, evidence of the reliability of the fabricated structures will need to be collected *in situ* for each and every fabrication. Given the layer-by-layer processing with an unobstructed view of the top surface of the structure during fabrication, crucial aspects of the manufacturing process can be monitored in an unprecedented manner including the melt pool and ejecta. By characterizing this process and understanding the implications on process quality, a *qualify-as-you-go* methodology can be adopted as is required for insertion into manufacturing of flight critical hardware.

Within the taxonomy of PBF, Selective Laser Melting (SLM) has been optimized to create complex, high performance geometries in a diversity of metal alloys; however, process feedback is generally absent in production systems and is understood to remain as an eventual requirement for full qualification of these processes. Laser spatter is relatively well understood and can generally inform the process as to the quality of the structure under development. The final destination of the spatter after ejection can also have an impact on the fabrication through contamination or due to the introduction of irregular shaped and sized particles if the spatter returns back to either the melted section or open powder bed

in the build chamber. The hypothesis of this work is that *in situ* monitoring using relatively low-cost cameras at relatively high-speed frames per second can provide data on the position and velocity of individual spatter and thus enable statistical analysis of general spatter behavior to improve quality and yield.

1.1 Previous Work of Others

Laser powder bed fusion is affected by several types of defects such as lack of fusion [19], keyholing [49], balling [25], spatter [27], residual gas porosity [50], hatching strategy defects [51] and recoater defects [51]. Everton *et al.* [53] provides an overview of *in situ* and nondestructive evaluation. The premise of this effort is that spatter should be ejected to the margins of the powder bed or outer shelves of the build chamber to ensure no problems and the spatter should not return to impact on an active top surface of the device in fabrication as the spatter is considered a contaminant. The particles are generally considered to be larger than feedstock powder, which can directly affect the quality of the manufacturing process by obstructed the laser melting at that point. Spatter particles ejected from the melt pool can land on the melted section and these particles can be much larger than the D90 size of the powder size distribution and negatively impact the subsequent layers [25,27,62,63]. Spatter can lead to other negative effects such as increasing surface roughness of a part [12] or even increasing the layer thickness [64]. Large spatter particles can cause damage to the recoater blade and the spatter particles might not melt during the subsequent laser pass (a process which is optimized for the smaller powder size feedstock). Even though the surrounding powder can melt, the large spatter can give rise to either unfused regions or create a cavity around the particle. Spatter

can also land in unfused powder and change the local powder packing density and chemistry - either of which can affect melting behavior due to particle size differences.

In situ monitoring with the ultimate goal of providing feedback control has been researched in a variety of manners. [65,66,78–80] all have explored the implications and behaviors of spatter in powder bed fusion but none explored the use of high speed stereovision at the macro level to track the travel trends of spatter in the build chamber. Spatter in welding has also been explored and provides insights into AM spatter but it remains fundamentally different as the processes are not the same. [71, 72, 81–83, 85] all investigated monitoring the process at the melt pool by measuring the melt pool shape and temperature, and although the melt pool is the origin of spatter, this subject is outside of the scope of this work. The melt pool is the essence of SLM and clearly is critical to understanding the quality of a fabrication; [84, 86–89] monitored and tracked the scan path which anecdotally has a significant impact on the amount and direction of spatter. This effort is intended to inform the process by identifying spatter behavior to determine if a build is compromised with the eventual goal of providing feedback for closed-loop control and a *qualify-as-you-go* paradigm.

High speed digital photography has been utilized to characterize spatter in several studies. Frame rates used include 1,000 fps[78], 2000 fps[67], 6000 fps[66] for laser additive processes. High speed thermal cameras have also been leveraged with frame rates of 1800 fps [27]. High speed photography (3000 and 6000 fps) has also been used to characterize the behavior of interacting spatter for a multi-laser SLM 280 HL system [65].

The use of ultra-high speed imaging (100,000 frames per second) has uncovered that the mechanism causing spatter is from vapor driven entrainment of micro-particles by an ambient gas flow [30]. Previously, it was believed that spatter was caused by laser induced recoil pressure (which is still true for laser welding processes, see [67]). Ly *et al.* identified three distinct types of particles. The first involve particles with low vertical momentum that are carried into the melt pool. The second category of spatter particles have higher vertical momentum but originating more than 2 melt pool widths away from the beam and are carried into the trailing portion of the vapor jet. These are then ejected as cold particles. The third category of spatter particles are closer to the laser beam than the second category. These spatter particles are carried into the laser beam which heats the particles to the point of becoming incandescent, hot particles. With a scan speed of 1.5 m/s and laser of 200W and fusing stainless steel 316 powder, Ly *et al.* found that 60% of spatter particles observed are the third category (hot particle ejections) with velocities of 6–20 m/s and observed particle full width at half maximum (FWHM) diameters of 10 to 30 microns, another 25% are the second category (cold entrainment ejections) with velocities of 2–4 m/s and FWHM diameters of 20 to 30 microns, and the remaining 15% are recoil pressure induced droplet breakup ejections with velocities of 3–8 m/s and FWHM diameters of 15 to 70 microns. It should be noted that this work did not occur in a chamber with flowing inert gas (i.e. argon) over the powder bed as is common in most production systems. This inert gas flow could influence the flight path of the spatter particles.

2.0 Methods and Materials

The overarching goal of this effort is to statistically quantify the characteristics and behavior of spatter in order to identify strategies to mitigate any resulting reductions in quality. A secondary consideration is to implement a system that was less than 5% of the total cost of the manufacturing system to broaden the adoption of the proposed monitoring system. For stereo analysis, calibration and camera mount design are critical parameters for accuracy in measurements.

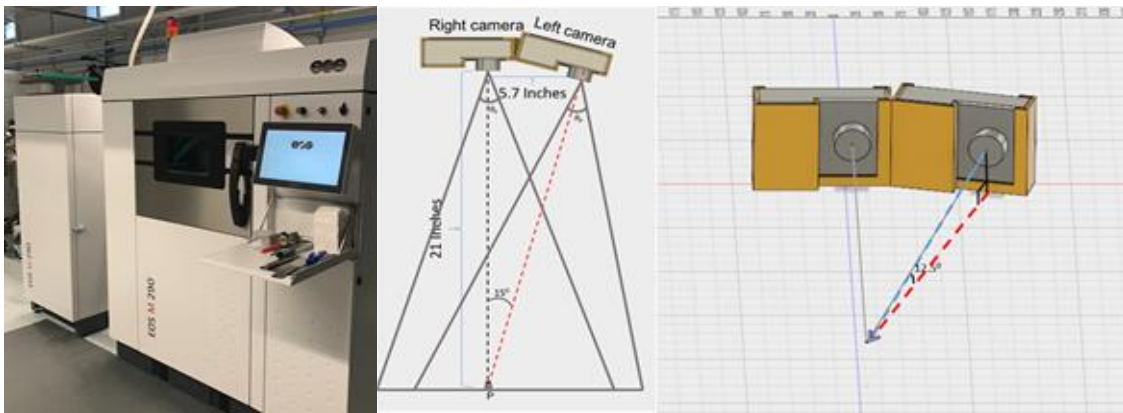


Figure 23: EOS M290 with Front Port Window (Left) and Stereovision Schematic (Right)

2.1 High speed stereovision camera system

Two low cost, high speed cameras (FPS1000 by The Slow Motion Camera Company) were purchased and integrated together in a stiff housing in order to minimize any movement relative between the cameras, and thereby allowing for standardization during calibration and live spatter measurements. An 18 mm lens was used with an aperture set to f-stop of f/4.5 (to increase depth of field). Images were taken in raw with a 1280x720 pixel count (maximum allowed for the camera). Calculating the spatial resolution for visible light (470 nm – 625 nm) gives a range of 18 $\mu\text{m}/\text{pixel}$ to 24 $\mu\text{m}/\text{pixel}$.

2.2 Stereovision and Epipolar Geometry to identify position and direction of spatter

For calibration, the intrinsic parameters include information on the camera calibration matrix (K) and distortion coefficients which are obtained through single camera calibration. The former is given by

$$K = \begin{bmatrix} f_x & 0 & c_x \\ 0 & f_y & c_y \\ 0 & 0 & 1 \end{bmatrix} \quad (eq.2)$$

$$K' = \begin{bmatrix} f'_x & 0 & c'_x \\ 0 & f'_y & c'_y \\ 0 & 0 & 1 \end{bmatrix} \quad (eq.3)$$

where K and K' are camera calibration matrices, f_x , f_x' , f_y , f_y' are focal length in pixel units, c_x , c_x' , c_y and c_y' are principal points, normally at the center of the image. The open source Computer Vision library was used to locate a checkerboard pattern in fifty different poses (**Figure 24**). The intrinsic parameters are then used during stereo calibration, where coincident images from a stereo pair determine the extrinsic parameters of the system. The extrinsic parameters correspond to the rotation (R) and translation (t) between the two cameras,

$$P = K[I|O] \quad (eq.4)$$

$$P' = K'[R|t] \quad (eq.5)$$

where P and P' are the projection matrices which are 3x4 matrices, I is the identity matrix, R is the rotation matrix and t is the translation matrix. The matrices returned from calibration are then used to rectify simultaneous frames using the OpenCV function stereoRectify. Rectification calculates the necessary values to apply a geometric transformation on both images, ideally resulting in near horizontal epipoles on the image

plane. The projection matrices were then used to triangulate two matched points between simultaneous frames. This method could then be applied to measure the length of light exposure caused by spatter between two sequential frames.

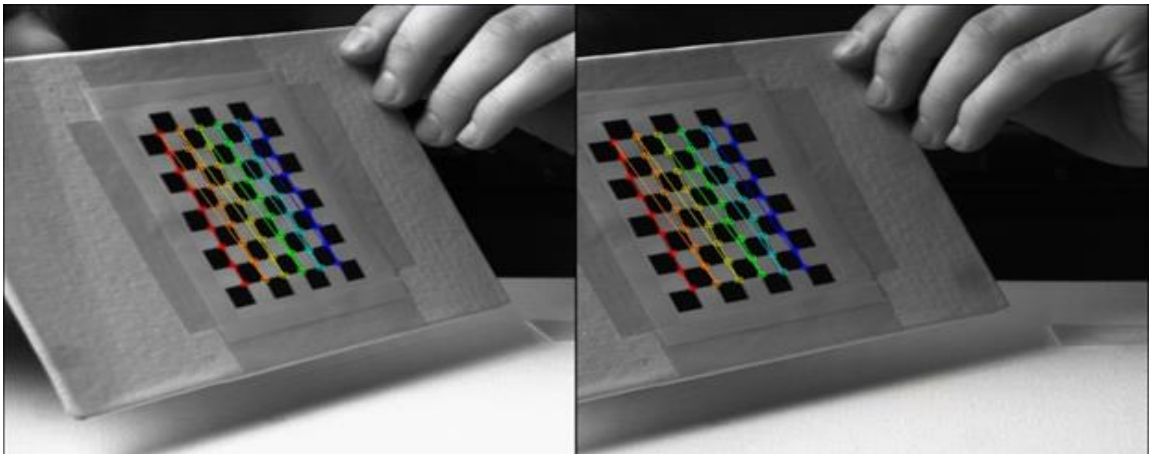


Figure 24: Stereo Calibration between two coincident images from different perspectives



Figure 25: Stereovision quality assurance using a caliper (50.01 mm top, and 9.99 mm bottom).

Two stereo images of a caliper were taken as a calibration check (**Figure 25**), two points were found, and the distance between them was measured. The distance of the first measurement between the two points in the caliper was 50.01 mm, while the distance measured with stereovision was 50.69 mm, producing an error of 1.34%. The second distance was 9.99 mm, while the measured stereovision distance was 9.986 mm producing an error of 0.04% (which is precise as it is below the accuracy of the caliper).

3.0 Results and Discussion

A selective laser melting (SLM) build was completed with the camera system outside the front port of an EOS M290. Ideally the system would be housed within the build chamber

to provide the closest perspective which allowed for the entire build volume to be seen from both cameras; however, in this preliminary study, an external perspective provided benefits such as physical access to the cameras, etc. Future work will include integrating the camera system more closely to the powder bed in a final system which is planned to be installed in a 3D Systems ProX 320 where internal integration will be eased with the larger build volume. Some concern exists regarding the vacuum pulled temporarily at the beginning of the build and the impact that this may have on the health of the electronics. Eventually, data collected from both of the two systems (ProX 320 and M290) will allow for a comparison of spatter behavior across a diversity of processes.

3.1 Sequential versus single image spatter tracking

To validate the concept of using over-exposure to integrate the light and identify the speed and direction of the spatter from a single stereovision image, some spatter particles were tracked for multiple frames as an alternative method of measuring velocity and to determine how the velocity and direction changed over a larger time frame (3 mS rather than 0.5 mS). As the exposure was 500 μ s and the period of the imaging was 1 mS, the distance traveled from frame to frame was expected to be twice the distance of the length of the spatter line in any given frame - minus the effects of gravity or build chamber atmosphere. In **Figure 26**, three distinct spatter particles are tracked across three sequential frames as shown on the bottom of the figure. The top of the figure shows the three frames overlaid on each other with green (frame 1), blue (frame 2) and red (frame 3) coloring to distinguish the particles in time. As the period of the image acquisition (1000 fps frequency, 1000 μ s period) is twice as long as the exposure time (500 μ s), the smeared

images for each of the three cases should have similar lengths and the lines should be separated by the same length - as the camera exposure duty cycle is 50% (500 μ s exposure with 1000 μ s imaging). This is shown to be true not just for the two fast particles ejected to the right but also for the older and slower particle to the left (see **Figure 26**). The process emission is also shown as a nebulous form at the bottom of each frame and is in fact moving along the laser path as expected. Other noise is shown primarily in the third red frame. As the third frame has the faintest spatter signature due to the age of the particles, the threshold for detection was reduced and this introduced significant noise into this frame. By attempting to capture only one image per spatter and ignoring very new and very old spatter, the problem of uniform brightness is expected to be eliminated for the automated computer script by capturing only a narrow band of brightness which in turn results in only a certain age of spatter being captured in the computer vision.

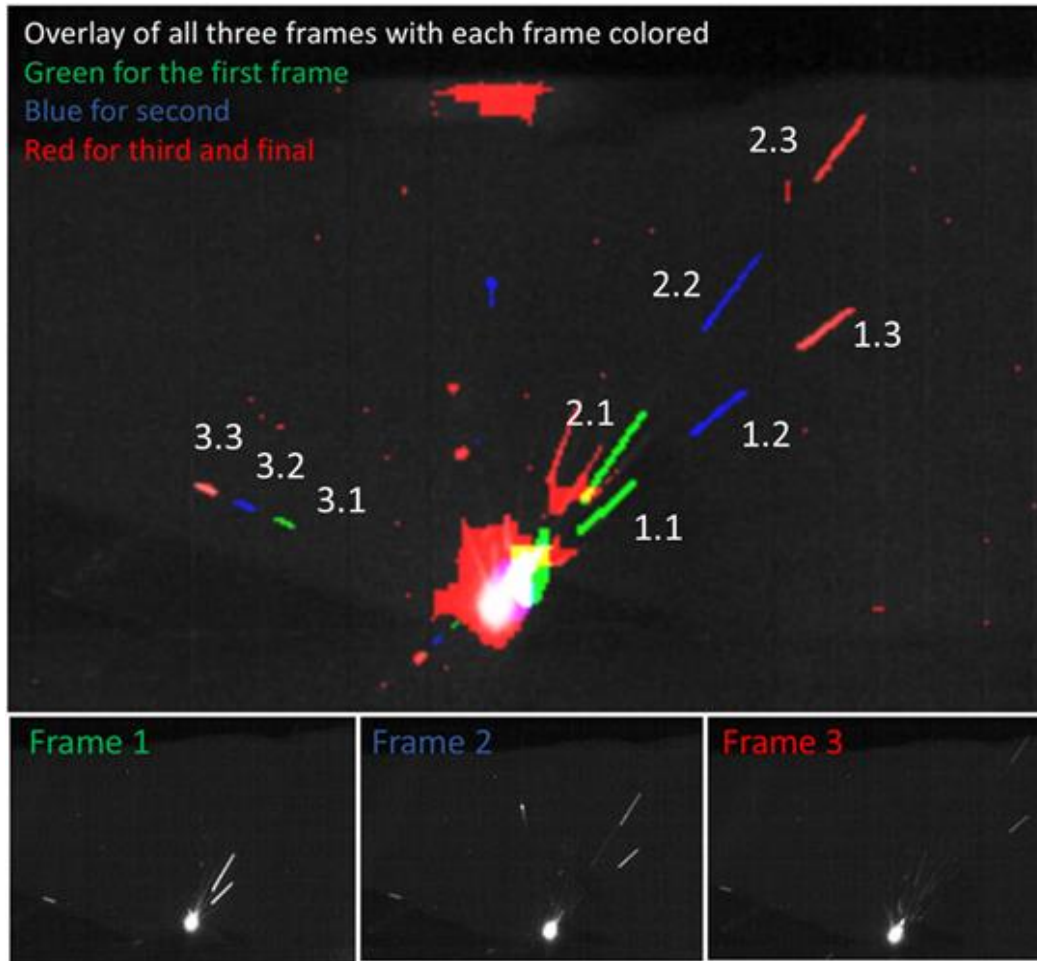


Figure 26: Sequential imaging of the right camera to demonstrate that tracked spatter measurements (frame to frame with an overlay) can be obtained in a single image.

3.2 Stereo imaging of spatter and determination of velocity and direction

To demonstrate the spatter monitoring approach, **Figure 27** shows a single dual-frame capture of an instance of significant spatter production ejected from the melt pool. In both cameras, three spatter particles are shown and easily matched between the two cameras. OpenCV computer vision identifies these regions as high intensity (white) and with a large aspect ratio forming a line that projects back to the melt pool as expected. In each spatter case, the length of the image artifact is an overexposure across $500 \mu\text{s}$ and thus provides the distance traveled over that time and consequently a velocity can be calculated. The

particles are expected to follow a normal ballistics trajectory and change their velocity with time and drag; however, this is assumed negligible over the short 500 μs time frame. Each spatter can be identified by two points: the beginning and the end. For each point in each image, a row and column can be determined. With the same feature (e.g. start or end of spatter streak) as seen in two images, four values (rows and columns) can be obtained and through epipolar geometry the location of the point in 3D space (X, Y, and Z coordinates) can be determined. With the 3D location of both the start and stop of the spatter, a direction vector can be generated and the magnitude of the vector (length in mm) can be divided by the 500 μs exposure time to calculate a velocity. Furthermore, if the beginning of the spatter and the melt pool are known in 3D space, a distance can be calculated from the origin (the melt pool) to the spatter streak beginning. By dividing the distance by the velocity, an age can be established for the particle. The older the particle, the less bright the emissions. This monotonically decreasing brightness is a characteristic that is leveraged to limit the image identification of the spatter to only one time and to avoid double or multiple counting in statistical evaluation. Spatter that are too bright (often in the process of formation or calving and therefore without a distinct start and stop), and conversely, those that are not sufficiently bright will be excluded. The intent is for the computer vision system to only identify the spatter once in its lifecycle to collect accurate statistical data on position and velocity and to avoid the challenging tracking of the particle between frames. Some particles are much faster than others so separation between the same particle on two sequential frames can vary significantly. Moreover, the brightness of the particle is ephemeral and identifying spatter on two frames may not always be possible. **Figure 27** shows both the left and right-side cameras of an active moment during selective

laser melting of powder with substantial generation of spatter. **Table 3** shows the X, Y, Z direction and velocity of each of the spatter shown in **Figure 27**.

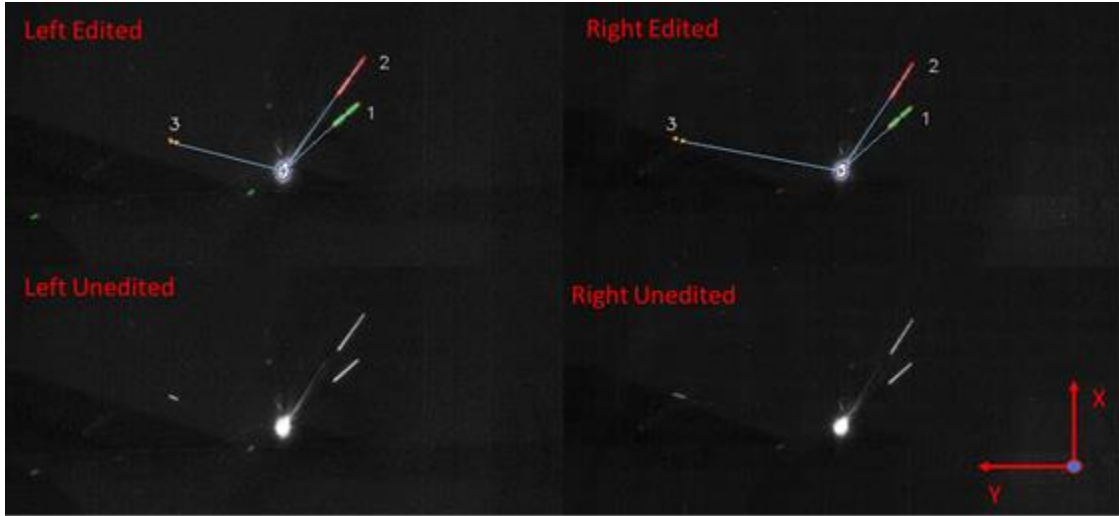


Figure 27: Stereovision imaging of spatter of varying directions and speeds (+Z into plane)

Table 3: Spatter from **Figure 27** described in direction and velocity

Particle	Start ([x,y,z], mm)	End ([x,y,z], mm)	Direction ([x,y,z], mm)	Velocity (m/s)
1.1	[0.6590, -7.590, 3.301]	[2.875, -10.20, 6.840]	[2.216, 2.610, 3.539]	9.85
1.2	[3.025, -10.40, 6.017]	[5.249, -12.80, 9.481]	[2.223, 2.392, 3.463]	9.52
1.3	[5.182, -13.21, 8.668]	[7.160, -15.17, 12.85]	[1.978, 1.960, 3.463]	10.05
Avg Particle 1				9.81
2.1	[2.415, -7.800, 3.881]	[6.730, -10.21, 8.902]	[4.315, 2.410, 5.021]	14.09
2.2	[6.730, -10.21, 8.902]	[10.62, -12.39, 13.70]	[3.893, 2.176, 4.802]	13.11
2.3	[10.62, -12.39, 13.70]	[14.49, -15.15, 16.85]	[3.866, 2.768, 3.141]	11.40
Avg Particle 2				12.87
3.1	[-0.650, 19.04, 19.16]	[-0.305, 20.65, 20.36]	[0.3452, 1.604, 1.198]	4.06
3.2	[-0.4195, 20.98, 21.06]	[0.1509, 22.43, 21.51]	[0.5704, 1.451, 0.4597]	3.25
3.3	[0.1509, 22.43, 21.52]	[0.1678, 24.66, 24.05]	[0.01691, 2.227, 2.535]	6.75
Avg Particle 3				4.69

Future work will investigate more accurately where in the melt pool each spatter originated and furthermore, if the melt pool motion (build path) has an impact on the quantity, speed and direction of the spatter. Preliminarily it can be noted that when the laser changes direction, the production of spatter dramatically increases, and the spatter tends to favor the direction opposite to the new laser scan path. The ultimate goal of this research effort is (1) to automate the one detection of each spatter and to collect statistical data over millions of frames (2) to verify that by determining the position and velocity of the spatter just after creation that this method can predict the final impact destination of the spatter in order to improve quality and yield.

3.3 Spatter calving and implications on melt pool location and contour determination

On a large fraction of the captured images, spatter was shown in the nascent stage - still connected with the melt pool. **Figure 28** shows the extreme case of a new particle which has yet to fully emerge from the melt pool and is being “calved”. Consequently, the velocity and age of the particle cannot be determined as there is no start point other than the melt pool which is large and provides an insufficient data as to the exact origination. These cases are therefore ignored with the understanding that as the spatter emerges completely, the particle will be captured and evaluated in a subsequent frame. An additional technique to avoid evaluating calving spatter is to identify and contour the melt pool. If excessive concavity exists (easily detectable in OpenCV), the contour can be ignored. Furthermore, if the centroid of the melt pool is calculated as required in order to determine the origin in an age calculation, the centroid can be adjusted to eliminate skewing of the location based on calving spatter influence.



Figure 28: Spatter calving where new spatter particles have been formed and are being ejected

These “half-baked” spatter do not have a distinct start and stop point which means that although the direction can be determined, the velocity cannot. Furthermore, the centroid of the melt pool is distorted and incorrectly pulled to the side of calving particle.

4.0 Conclusions

In conclusion, this paper details a low-cost method for spatter tracking and analysis for laser powder bed fusion. The key completed objectives are as follows:

- Stereovision demonstrates a reliable way to gather *in situ* statistical information about spatter particles.
- Spatter Age, Velocity, Direction, and Size have been reliably measured.
- Low cost (less than \$10,000 USD) and open source resources were successfully used to accomplish this work.
- The foundation for an automated system has been laid, which will allow for the gathering of statistical data for future analysis.

Future work will entail the automation and statistical identification of trends which can be used for defect analysis in laser powder bed fusion.

Acknowledgments

We would like to thank the Friedman Endowment for Manufacturing at Youngstown State University. This effort was performed in part through the National Center for Defense Manufacturing and Machining under the America Makes Program entitled “Maturation of Advanced Manufacturing for Low Cost Sustainment (MAMLS)” and is based on research sponsored by Air Force Research Laboratory under agreement number FA8650-16-2-5700. The U.S. Government is authorized to reproduce and distribute reprints for Governmental purposes notwithstanding any copyright notation thereon.

5.0 Publication Three: Statistical Analysis of Spatter Velocity

Statistical Analysis of Spatter Velocity with

High Speed Stereovision in Laser Powder Bed Fusion

Christopher Barrett¹, Carolyn Carradero¹, Evan Harris¹,

Kirk Rogers², Eric MacDonald¹, Brett Conner¹

¹Youngstown State University, Youngstown, OH 44555

²Youngstown Business Incubator, Youngstown, OH 44503

Abstract

As unprecedented design freedom is realized through additive manufacturing and simultaneously as the diversity of materials improves to include high performance metals, aerospace and biomedical applications demand improved quality control measures. In the context of additive manufacturing, new opportunities for *in situ* monitoring are now possible with a qualify-as-you-go layer-by-layer methodology. In this study, a pair of low-cost, high speed cameras recording the selective laser melting of maraging steel were synchronized to measure stereoscopic features of the resulting spatter. Through epipolar geometry, accurate measurements were calculated of the age, speed and direction of thousands of spatter events. Statistical analysis was performed focusing on spatter velocity with the driving hypothesis that velocity can be correlated to the weld quality and eventually leveraged in real-time process control. Opportunities, future work, and challenges are discussed.

1.0 Results and Discussion

The literature and experimental sections of this publication are similar to those presented in Section 4 (Publication 2) and have therefore been left out of this section.

A build of maraging steel was performed on an EOS M290, and a seven second video was taken at 1000 frames per second to determine bulk spatter statistics resulting in 7000 images. The cameras were mounted outside of the chamber window and utilized 18mm lenses.

1.1 Velocity Subset Validation of Stereovision Tracking

To gain insight and validate the algorithm, a subset of images was taken with the laser turning a corner and starting in the opposite direction with the hatch. Three subsequent images were taken after the turn to track the spatter and gain triplicate measurements, spatter were typically able to be tracked for three subsequent images before they faded and became too difficult to track. Although not all spatter were detected in the three images, 50 spatter were identified and direction was calculated (**Figure 29**). Spatter just after a change in laser hatching direction were chosen because it presented a clean set of data without the laser creating flash points when it ignited soot directly over the melt pool (false positive detections) and allowed for a manual check of the data to ensure all the spatter were appropriately detected to avoid false negative detections. This spatter was then analyzed via the developed algorithm and the start and end points of the spatter streak verified manual to determine the average population velocity and magnitude of the corresponding vectors and is shown in **Table 4**. This resulted in an average velocity of 9.38 m/s, with a minimum detection of 2.98 m/s and a maximum of 27.60 m/s which is consistent with the analysis of Ly *et al.* which listed their approximated range as 2-20 m/s [30]. This clean

and verified dataset average would then be used to compare to the full set of images to ensure similarity in results.

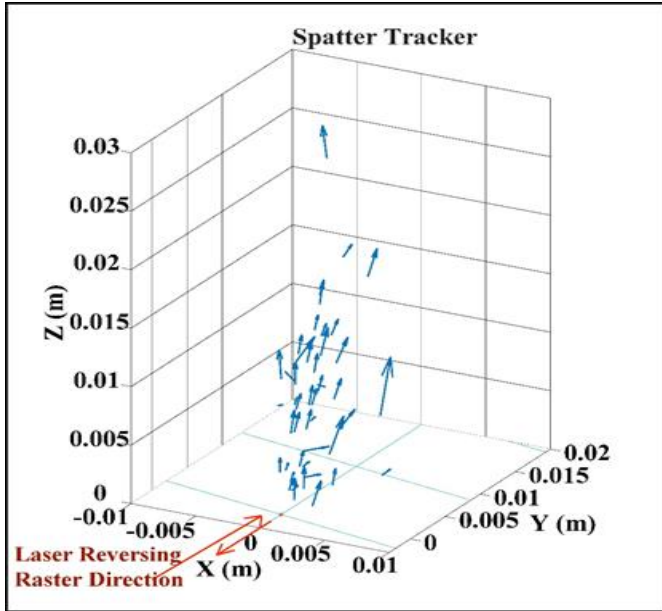


Figure 29: Spatter detected on edge of part as laser path is changing direction, laser direction indicated showing path during spatter formation

Table 4: Spatter detected on edge of part with laser turning to head in opposite direction, first ten results shown with bulk statistics below, exposure of 500 μ s

Particle #	Start ([x,y,z], mm)	End ([x,y,z], mm)	Magnitude (mm)	Velocity (m/s)
1	[-1.496, 4.867, 6.798]	[-1.553, 7.087, 10.83]	3.97	7.93
2	[-1.463, 7.379, 8.989]	[-1.877, 9.662, 12.96]	4.60	9.19
3	[-2.822, 10.69, 14.07]	[-2.903, 12.64, 17.27]	3.76	7.51
4	[-0.8661, 2.997, 1.628]	[-1.175, 4.841, 2.921]	2.27	4.55
5	[-0.5894, 4.635, 5.372]	[-0.724, 7.155, 9.521]	4.86	9.71
6	[-0.4848, 4.122, 0.4827]	[-2.188, 7.403, 4.562]	5.51	11.01
7	[-0.3990, 1.863, 1.249]	[-0.6433, 3.815, 3.573]	3.04	6.09
8	[0.2354, 2.790, 4.426]	[4.839, 5.104, 5.590]	5.28	10.56
9	[-1.895, 5.238, 10.37]	[0.6655, 9.580, 16.50]	7.94	15.88
10	[-0.8180, 4.122, 2.336]	[-1.135, 6.360, 5.510]	3.90	7.79
<i>Avg Velocity Population (n=50)</i>				9.38

<i>StDev.p Population (n=50)</i>			4.42
<i>Maximum</i>			27.60
<i>Minimum</i>			2.98

1.2 Stereo imaging of spatter and determination of bulk statistical velocity

The algorithm was then allowed to run over the entire seven seconds of video which at 1000 fps generated 7000 paired images. Autodetection of spatter was utilized and the magnitude and velocity of the spatter was found. The results were plotted in **Figure 30** with their vectors in three-dimensional space, relative to the centroid of the melt pool of the previous frame, this was set to the origin to allow for the visualization of the spatter's detected location in regard to the melt pool. 10,447 spatter were detected over the seven second video, which includes duplicate and triplicate detections as at 1000 fps most spatter could clearly be seen multiple times. It is believed that these multiple detections could be of benefit when working with the average velocity as they would increase the weight of valid detections. However, this will statistically make the average velocity slower as the faster particles are detected fewer times and so therefore have less weight on the overall average. Of note, false positives can be seen primarily in the central region directly above the melt pool. These are assumed to be soot that was irradiated by the laser and not spatter, this was verified by a manual check of various images were the results occurred and it was found that the particles were often directed down instead of up from a clear origin from the melt pool. Further work is currently underway to automatically ignore these detection results.

Table 5 shows the statistical results of the analysis with the first ten detections similarly to **Table 4**. The average velocity over the entire set was 9.73 m/s which had good agreement with the previous subset of data having only a 0.35 m/s or 3.66% difference. The maximum value detected, and the minimum value showed a dramatically increased range. The current algorithm does not allow for sorting of detected spatter and determination of which images correspond to which detection, so we are currently unable to examine the maximum and minimum values to determine their validity. This feature is currently being added and is expected to aid in the removal of false positives or negatives. **Figure 31** shows the histogram of the bulk results with the majority of the spatter being detected between 1.5 m/s and 14.5 m/s.

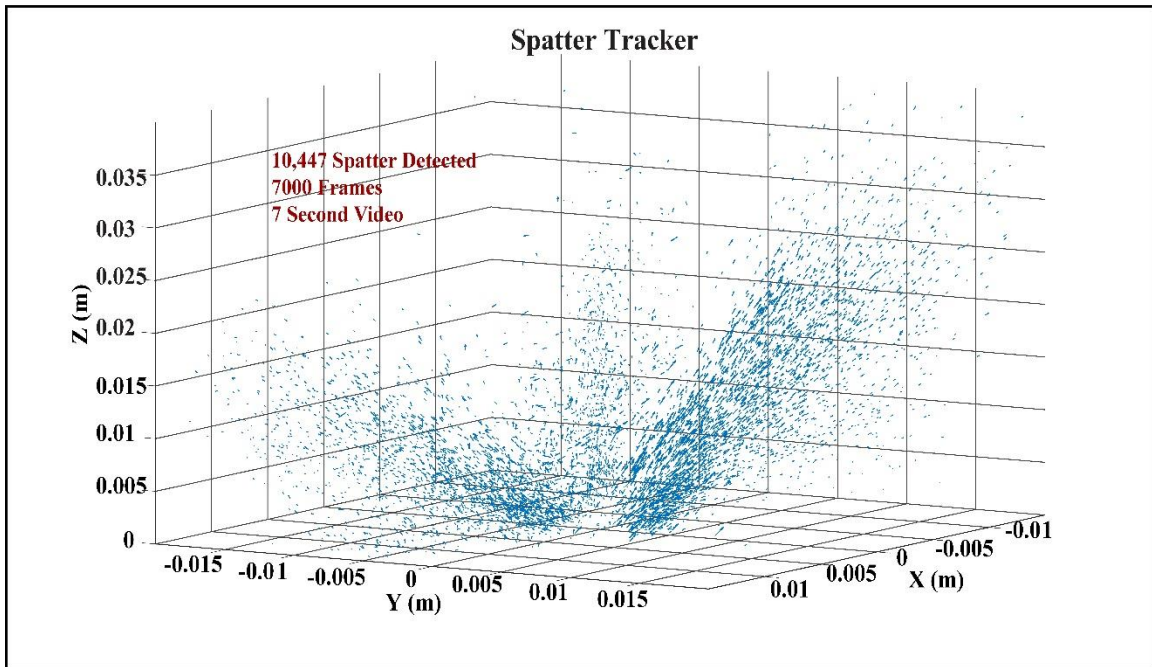


Figure 30: 10,447 Spatter magnitude vectors plotted centering each spatter to the same origin point, detected over a seven second imaging period

Table 5: Measured beginning and end points for first 10 spatter from **Figure 30**, their calculated magnitudes and velocities, and bulk statistical results.

Particle #	Start ([x,y,z], mm)	End ([x,y,z], mm)	Magnitude (mm)	Velocity (m/s)
1	[-1.496, 4.867, 6.798]	[-1.553, 7.087, 10.83]	1.61	3.23
2	[-1.463, 7.379, 8.989]	[-1.877, 9.662, 12.96]	4.18	8.35
3	[-2.822, 10.69, 14.07]	[-2.903, 12.64, 17.27]	2.28	4.55
4	[-0.8661, 2.997, 1.628]	[-1.175, 4.841, 2.921]	2.14	4.29
5	[-0.5894, 4.635, 5.372]	[-0.724, 7.155, 9.521]	10.13	20.25
6	[-0.4848, 4.122, 0.4827]	[-2.188, 7.403, 4.562]	2.11	4.21
7	[-0.3990, 1.863, 1.249]	[-0.6433, 3.815, 3.573]	1.30	2.60
8	[0.2354, 2.790, 4.426]	[4.839, 5.104, 5.590]	1.48	2.97
9	[-1.895, 5.238, 10.37]	[0.6655, 9.580, 16.50]	4.76	9.53
10	[-0.8180, 4.122, 2.336]	[-1.135, 6.360, 5.510]	1.84	3.68
Avg Velocity Population (n=10447)				9.73
Stdev.p Population (n=10447)				6.74
Maximum				79.64
Minimum				0.26

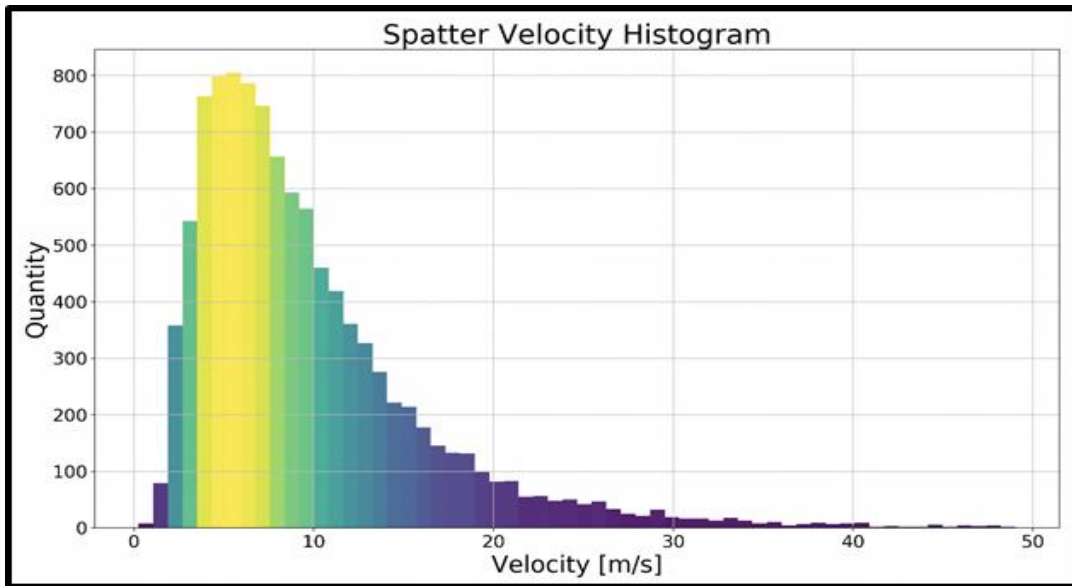


Figure 31: 10,447 Spatter detected graphed with velocity vs frequency

Future work is currently being performed to more accurately sort out false positive or negatives; however, it is believed that the average velocity of the group and bulk statistical results will not change substantially. Additionally, the algorithm is being modified to allow for the determination of which spatter has been detected multiple times so that appropriate weighting of the average can occur. Further analysis is also under way to compare the bulk spatter data under various laser parameters sets below and above recommended values, multiple printing platforms, and material types. The average velocity for these groups is posited to shift accordingly with the intention being that various platforms will have similar results with similar processing parameters and material types. Further work is also being performed to track the average direction based on the origin in the melt pool with respect to the melt pool centroid.

2.0 Conclusion

In conclusion, a low-cost spatter tracking method and analysis for laser powder bed fusion has been presented along with initial statistical results. The system can be used to collect real-time statistical data on the spatter behavior of a process and may have utility in terms of measuring the performance of the process. This paper demonstrates the tenets of the proposed *in situ* measurement system and the key completed objectives of this work are as follows:

- Reliable collection of demonstrated of statistics relating to spatter velocities gathered by stereovision over 1000s of frames.
- An open source and low-cost (less than \$10,000 USD) hardware and software system was successfully implemented.

- Initial results of collected statistical data are reported which demonstrate that the data are in-line with previous reports but now can be captured in a continuous and real time data collection system.
- Utilizing the stereovision setup enabled increased accuracy in the measurement for velocity and quantity.

Acknowledgments

We would like to thank the Friedman Endowment for Manufacturing at Youngstown State University. This effort was performed in part through the National Center for Defense Manufacturing and Machining under the America Makes Program entitled “Maturation of Advanced Manufacturing for Low Cost Sustainment (MAMLS)” and is based on research sponsored by Air Force Research Laboratory under agreement number FA8650-16-2-5700. The U.S. Government is authorized to reproduce and distribute reprints for Governmental purposes notwithstanding any copyright notation thereon.

6.0 Publication Four: Computer Vision for Spatter Motion Analysis

Computer Vision for Spatter Motion Analysis

in Relation to Process Parameters for Laser Powder Bed Fusion

Christopher Barrett, Evan Harris,

Eric MacDonald, Brett Conner

Youngstown State University, Youngstown, OH 44555

Publication: To be submitted to the Additive Manufacturing Journal

Abstract

As the number of safety-critical aerospace applications increases for additive manufacturing, process monitoring to ensure quality has become paramount. Economical and accurate sensors are required to evaluate unique aspects of the process, such as melt pool and spatter behavior. Additive manufacturing employs a layer-by-layer paradigm, which enables a qualify-as-you-go methodology that can be leveraged for the certification of fabricated structures. In this study, videos from two synchronized, low-cost, high-speed cameras were evaluated with epipolar geometry in order to track both the direction and velocity of individual spatter. With AlSi10Mg as the feedstock, laser power, scanning speed, and layer thickness were varied for the standard argon flow rate and direction. The velocity and direction of spatter were evaluated across the process space, in which the direction was relative to the X-Y plane (relative angle to the laser scan path on the powder bed surface) and X-Z plane (trajectory angle). Thousands of spatter were identified in each

process set to provide substantial statistical information. The direction and velocity histograms provide insights into both the process health (e.g. sufficient laser power) as well as the determination of the final destination of spatter in the build volume. These insights can inform scanning strategies to manage the trajectory of spatter to avoid inclusion in the fabricated structure.

1.0 Introduction

As the adoption of metal laser powder bed fusion (M-LPBF) in the aerospace industry continues to flourish, advancements in the understanding of the fabrication phenomena and metallurgy will be pivotal to the full realization of the manufacturing technology. To ensure the mechanical reliability of fabricated structures, a qualify-as-you-go methodology is necessary [70] and the unobstructed view of the build volume and the ease of identification and correspondence of spatter particles in stereovision can enable novel monitoring of this salient feature. In the context of the high expectations and requirements of the aerospace industry, the lack of flight heritage is leading to industrial demand for additional and effective advances in monitoring. Current methods for process monitoring in powder bed fusion vary widely and include visible imaging [22,84], high speed imaging [35,61], thermal imaging [88, 95], and X-ray imaging [96], among others [53].

Defects in M-LPBF include lack of fusion [19], spatter [27], keyholing [49], residual gas porosity [50], balling [25], hatching strategy defects and recoater defects [51]. Nondestructive evaluation and *in situ* monitoring was overviewed by [53] and demonstrates the necessity of further advances in these topics, specifically for eventual closed-loop control in LPBF. This article assumes that various laser parameters could lead to differing spatter velocities and therefore proposes an effective and financially feasible

way to record these velocities in real time. These velocities not only provide valuable insight to physics-based models such as those proposed by [25], but also will improve intuition for determining the optimal noble gas recirculation flow (often available on commercial systems) across the powder bed to redirect spatter from contaminating the build. Spatter landing on the melting section has been reported to negatively impact the subsequent layers, as the ejecta are often larger in size than the average powder and layer sizes, and could contain oxidation contamination [12,25,27,62–64].

Significant research, for both *in situ* monitoring and physics-based modeling, has focused on the melt pool and spatter behavior. Processing parameters and scanning strategies were examined to evaluate the effect on the melt pool [24,27,30]. Others noted that adjusting the three dimensional energy density by an identical amount through the increase of laser scanning speed did not have the same effect on the diminishing melt pool depth and width as the respective decrease in laser power, as the laser power decrease had a much larger effect on the melt pool [18,61]. Physics based modeling of the melt pool has also been explored and has been shown to predict pore formation and spatter creation [10,25,29,30,32]. Utilizing high speed digital videography to characterize spatter has been done in several studies. Frame rates have varied between 1000 frames per second (fps) to 6000 fps [66,67,78]. Thermal high speed cameras have been used as well [27]. High speed X-ray imaging was used to monitor the melt pool and spatter formation [97, 98]. These works provide experimental insight into the balance between the vapor driven entrainment and recoil pressure forces which combine for the creation of spatter and defects such as keyhole defects. Recent work on tracking spatter has shown the correlation to lack of fusion defects and has proposed mechanisms for this phenomenon [57]. This work showed

that multiple spatter can collide in flight to form a larger spatter particle which can negatively affect the build plate.

The ultimate goal of *in situ* monitoring is to provide feedback control. Behaviors of spatter in M-LPBF have been explored previously, but none have used high speed stereovision at the macro level to observe overall trends in optimal build conditions [65,66,78–80]. [71,72,81,82,85] investigated monitoring the process at the melt pool by measuring the melt pool shape and temperature, and although the origin of spatter is the melt pool, this is beyond the scope of the present work. The essence of M-LPBF is the melt pool, which is vital to understanding the quality of a fabrication; previous work has monitored and tracked the scan path which anecdotally has a significant impact on the amount and direction of spatter [84,86–89]. This work is intended to identify spatter behavior and thereby inform the process with the goal of eventually providing feedback for closed-loop control.

Previously, the authors had preliminarily laid the basis for this work without fully developing the algorithms to work on bulk data sets [94, 99]. This work focuses on showing that bulk statistical measurements of the spatter can be ascertained with minor financial investment and is feasible as a monitoring tool for build weld quality. It is believed that these results can further be used in the development and verification of physics-based models.

2.0 Methods and Materials

A 3D Systems ProX 320 with AlSi10Mg powder supplied by LPW with a 15 — 45 μm particle size distribution was used. A pattern of various laser parameters were analyzed with some being more nominal in energy density for comparison (**Figure 32**). Additionally,

the first contour was used for tracking spatter direction with a single line pass and had the parameters of 1750 mm/s and 296 Watts with a layer thickness of 60 μm. The energy density equation (eq. 1) was used to calculate the three dimensional energy density for the experiment, where Q is Energy Density (J/mm³), P is the laser power (Watts), V is scanning speed (mm/s), H is hatch spacing (mm), and T is the layer thickness (mm).

$$Q = \frac{P}{V * T * H} \quad (\text{repeat eq.1})$$

390 Watts	52.8 J/mm ³ 60 μm Layer	42.2 J/mm ³ 60 μm Layer	35.2 J/mm ³ 60 μm Layer
370 Watts	30 μm 100 J/mm ³ 40 μm 75.1 J/mm ³ 50 μm 60.1 J/mm ³ 50.1 J/mm ³ 60 μm	30 μm 80.1 J/mm ³ 40 μm 60.1 J/mm ³ 50 μm 48.1 J/mm ³ 40.0 J/mm ³ 60 μm	30 μm 66.7 J/mm ³ 40 μm 50.1 J/mm ³ 50 μm 40.0 J/mm ³ 33.4 J/mm ³ 60 μm
320 Watts	43.3 J/mm ³ 60 μm Layer	34.6 J/mm ³ 60 μm Layer	28.9 J/mm ³ 60 μm Layer
296 Watts	40.0 J/mm ³ 60 μm Layer	32.0 J/mm ³ 60 μm Layer	26.7 J/mm ³ 60 μm Layer
	1120 mm/s	1400 mm/s	1680 mm/s

Figure 32: Laser Parameter Design of Experiments shaded from white to black with calculated energy density

Spatter velocity and quantity were analyzed using previously developed technology [94, 99]. Thresholding of the images were done to allow for the greatest detection of spatter and were held uniform throughout the experiment. It is acknowledged that the manner of thresholding performed likely did block out spatter and clip their lengths thereby decreasing the true velocity of the spatter measurements. Great effort was taken to make this process as uniform as possible so the relative comparison between parameters would be valid and provide useful insight. Two cameras (FPS 1000HD, The Slow Motion Camera Company, United Kingdom) with 35 mm lenses set to an f-stop of f/4 and an iso of 100 were ran at 1000 fps with a shutter speed of 500 μ s. The cameras had a sensor size of $\frac{2}{3}$ " with 1280 x 720 pixels and were set up outside the build chamber window and video was taken axiomatically. A single 2 x 2 cm cube was printed, and in between each recording 5—10 layers were printed using nominal laser parameters to restore a good substrate for the next experiment.

Video was taken of the entire layer and then processed for the identification of the spatter utilizing a combination of modified OpenCV C++ software and Matlab. Due to the varying parameters different quantities were detected and matched by the algorithm for each parameter set. The minimum quantity detect for a parameter set was just over 1100 spatter, therefore for the velocity statistics each parameter set was normalized to a total population of 1100 spatter. For the quantification calculations, the spatter count was compared to the total number of images generated during the layer.

3.0 Results and Discussion

Spatter was analyzed with respect to its quantity, velocity, and angle versus laser parameters. These results are shown in various histograms and charts throughout this

section. For the quantitative analysis versus velocity, the population was normalized to a total of 1100 as the computer vision was able to identify and track differing quantities for differing laser parameters trials. **Figure 33** shows one of these histograms where the spatter quantity was normalized to 1100 spatter and the quantity was mapped for each velocity in 1.0 m/s increments. This data was taken using the laser parameters 370 watts, 1400 m/s scanning speed, 60 μm layer thickness, and a 110 μm hatch spacing. The average velocity was recorded at 2.02 m/s with a standard deviation of 1.96 m/s.

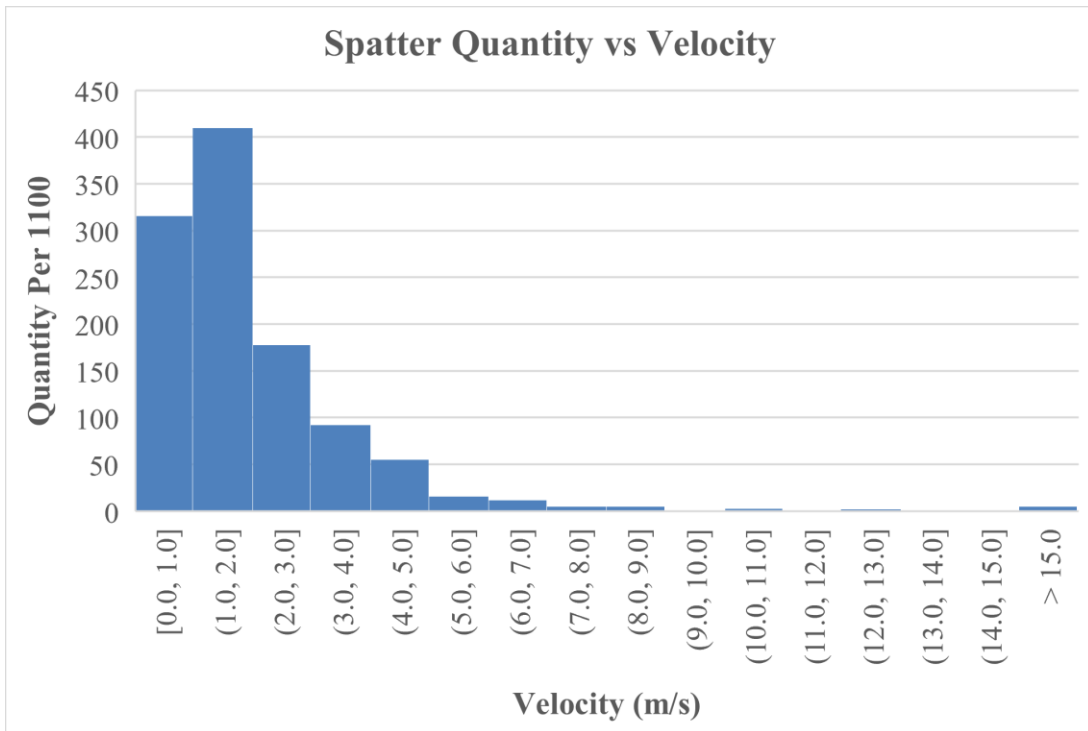


Figure 33: Quantity of spatter detected verse spatter velocity for the laser parameters 370 watts laser power, 1400 mm/s scanning speed, at 60 μm layer thickness

Multiple histograms were created for each of the laser parameters in this study with an identical histogram as shown in **Figure 33**, the results holding the layer thickness constant to 60 μm layers as in **Figure 32** and are shown in **Figure 34**.

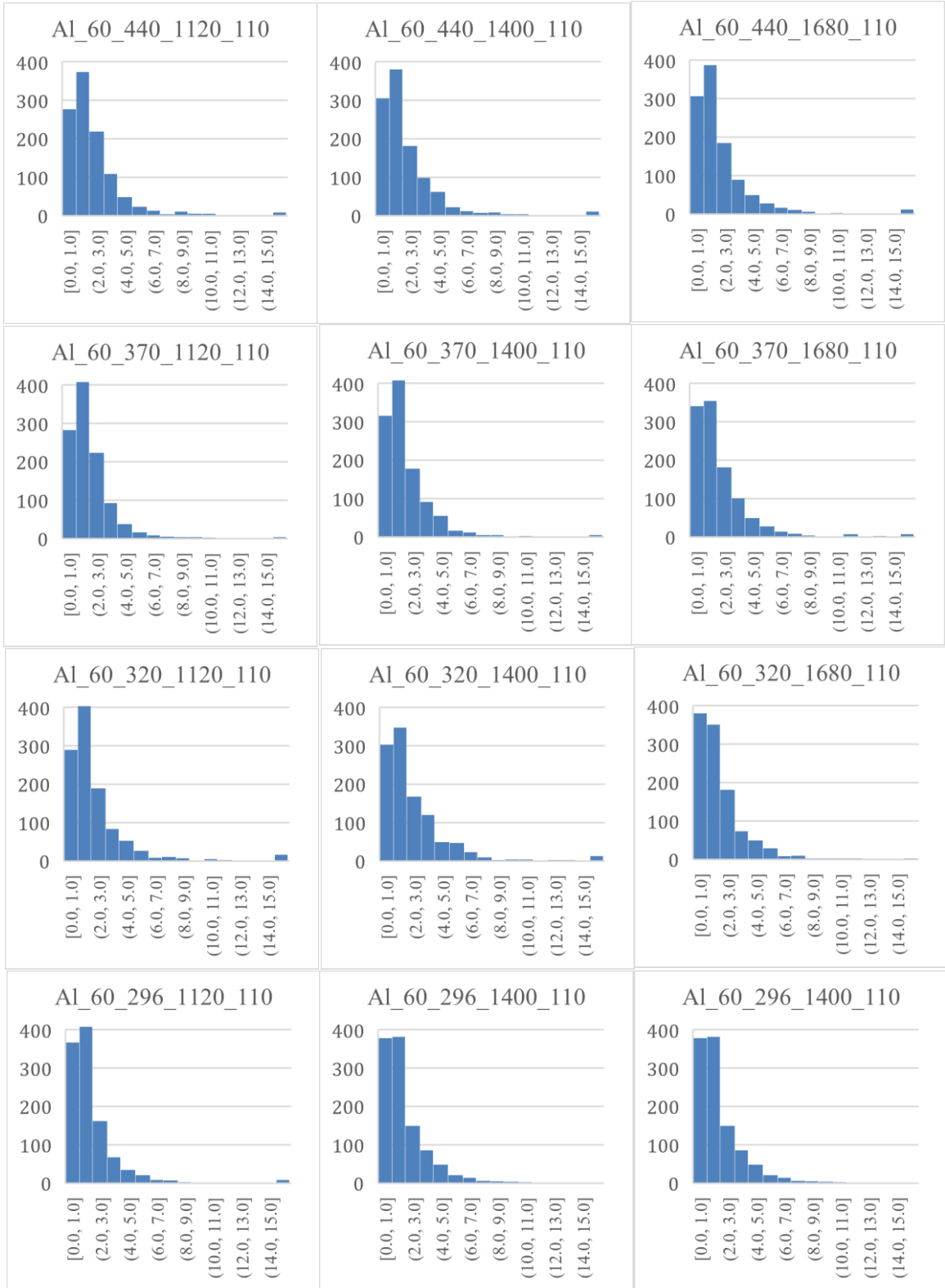


Figure 34: Histograms laid out as shown in **Figure 32** and **Figure 33**. All Populations normalized to 1100 spatter and analyzed verse spatter velocity in 1.0 m/s increments.

Based on the **Figure 34**, no clear trend emerged with showing a great impact on spatter velocity or scanning speed. Quantity was then graphed against three dimensional energy density equation and is shown in **Figure 35**. The results seemed to show a localized minimum of spatter produced for the middle region of energy density; however, trying to isolate if scanning speed or laser power had a greater impact gave random results that could not be quantified.

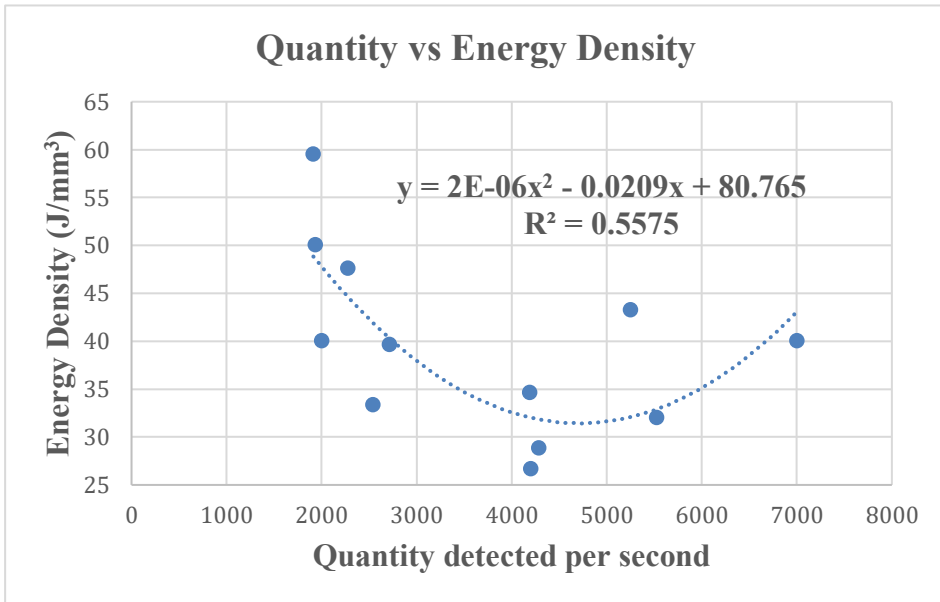


Figure 35: Quantity of spatter for the 60 μm layer series vs 3D Energy Density

Quantity was then graphed verse energy density for spatter less and greater than 1.0 m/s (**Figure 36** and **Figure 37**). These results show a general increase of spatter velocity with an increase of energy density. Upon further examination the trend seemed to flatten at the high velocities. Spatter quantity was then graphed against a velocity from 1.0 m/s to 4.0 m/s and is shown in **Figure 38**. This shows a much stronger trend with an R^2 value of 0.7819 instead of 0.5491.

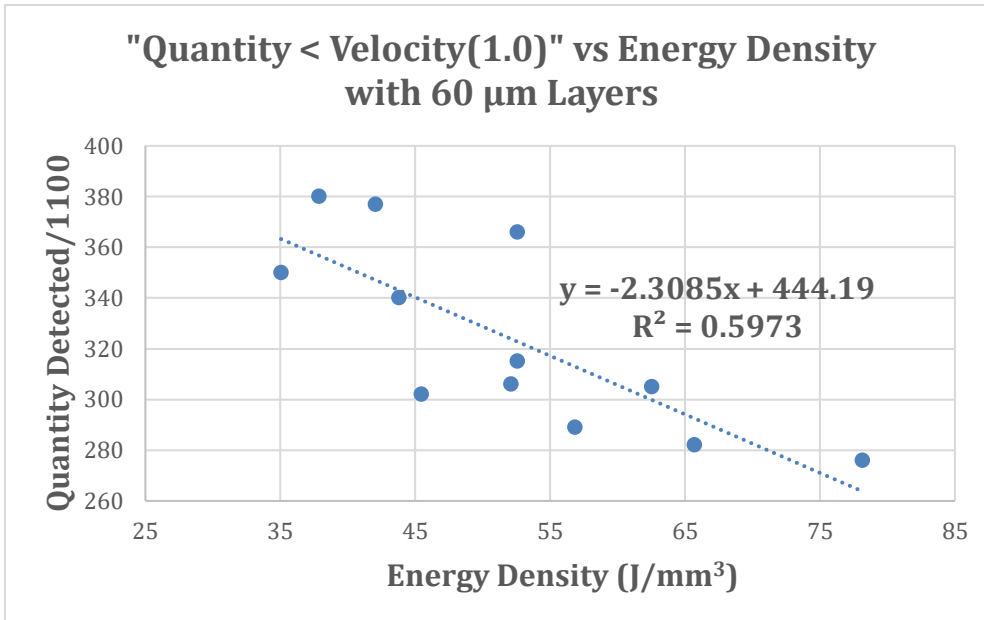


Figure 36: Quantity of spatter less than 1.0 m/s detected verse energy density with constant 60 μm layer thickness

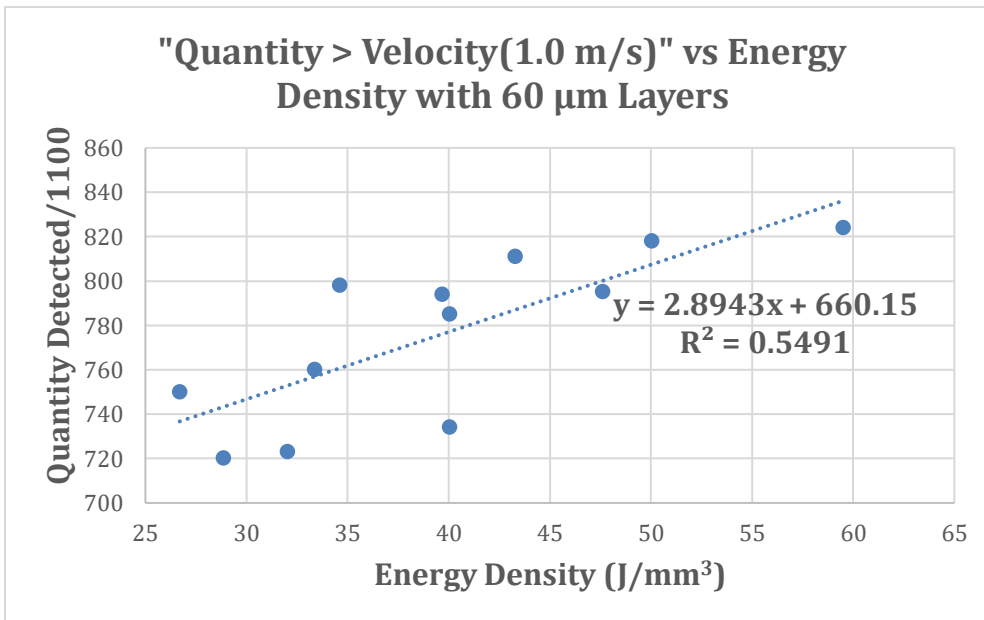


Figure 37: Quantity of spatter greater than 1.0 m/s detected verse energy density with constant 60 μm layer thickness

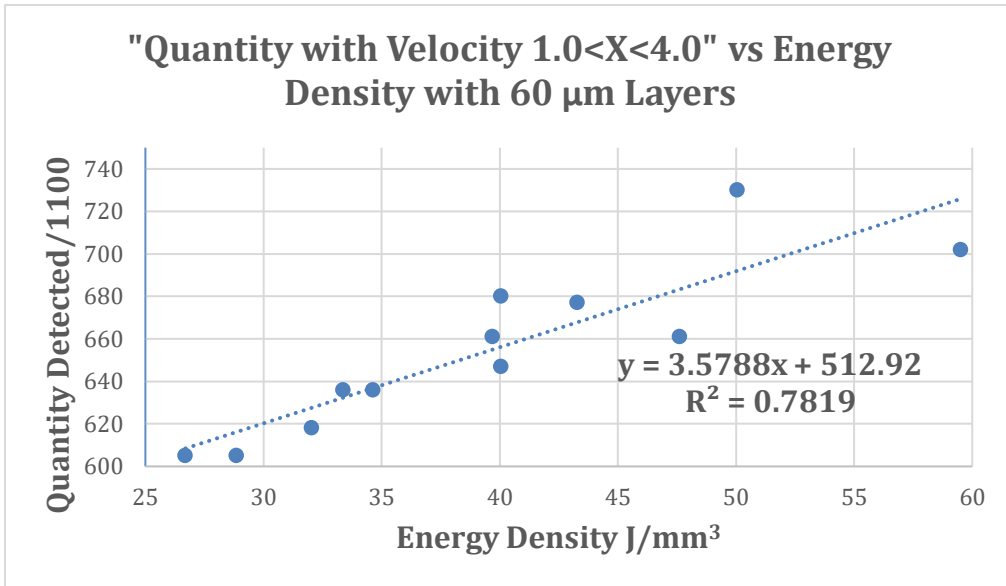


Figure 38: Energy Density vs Quantity detected above 1.0 m/s and below 4.0 m/s for 60 μm layers with the population normalized at 1100 total spatter

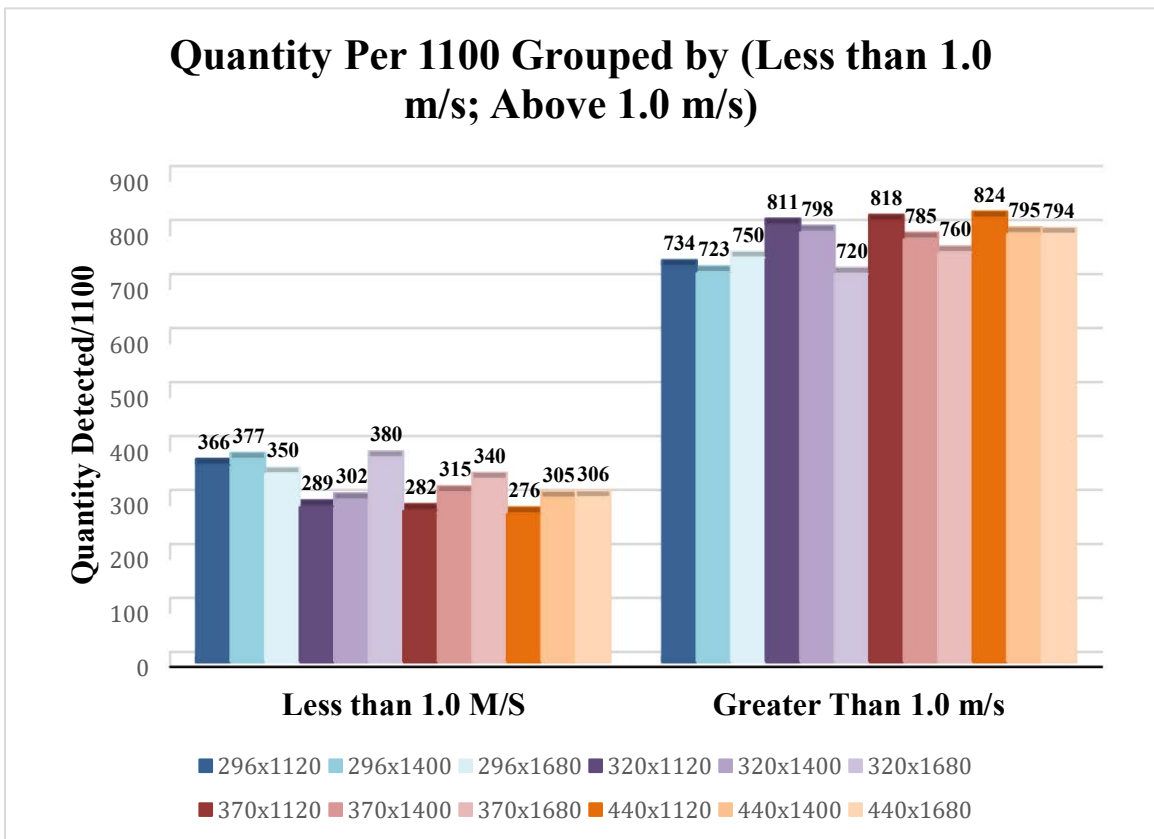


Figure 39: Histogram results showing spatter detected above and below 1.0 m/s for various laser parameter settings all at 60 μm layers

For ease in comparison a histogram was created showing the different laser power and scanning speeds (**Figure 39**). This was broken into two sections (less than 1.0 m/s and greater than 1.0 m/s). As mentioned before, no clear trend across laser power or scanning speed developed with a clear correlation to velocity.

Spatter vertical angle (θ) with a normalized x-y plane angle was analyzed and compared to laser energy density (**Figure 40**). The overall vertical angle average for each of the laser parameters is listed below in **Table 6**. Histograms were then taken with the spatter direction shown compared to the various laser parameters with the overall average listed first and then each velocity in 1.0 m/s increments and the corresponding vertical angles.

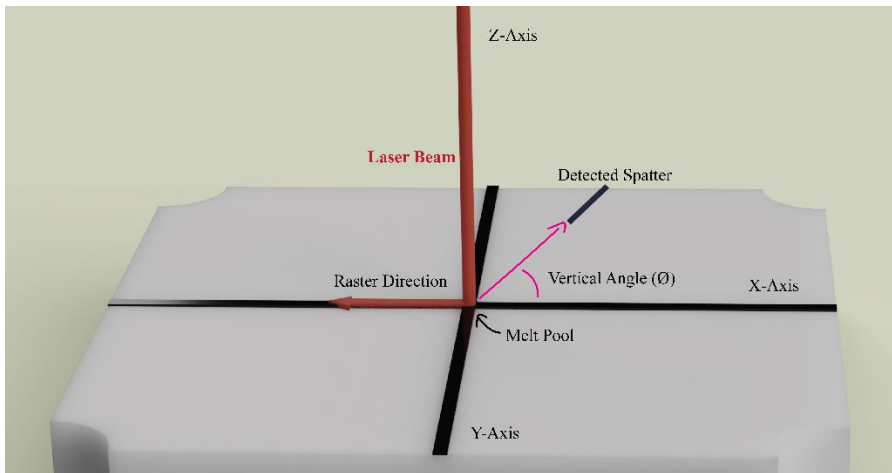


Figure 40: Diagram showing vertical angle with respect to raster direction and x, y, z coordinates

Table 6: Average Vertical Angle for various laser powers and scanning speeds

		Laser Power in Watts			
		296	320	370	440
Scanning Speed mm/s	1120	45.82589	45.37742	46.9687	39.47177
	1400	47.4874	45.11829	47.11037	43.94503
	1680	47.57302	44.97826	46.80041	44.39653

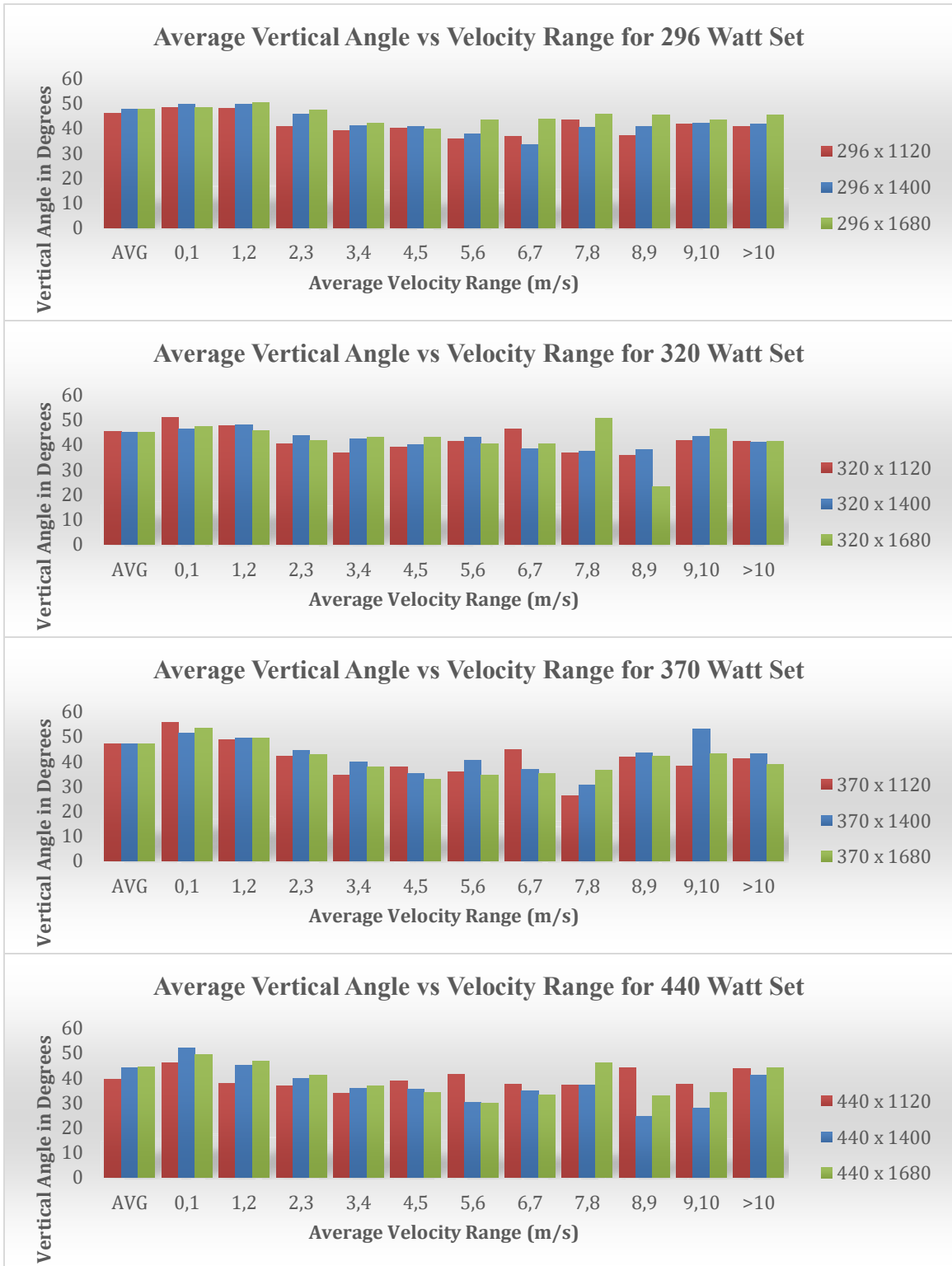


Figure 41: Average vertical angle compared to spatter velocity range for varying laser parameter sets all recorded at 60 μm layers

4.0 Conclusion

In conclusion, a low-cost spatter tracking method and analysis for laser powder bed fusion has been presented along with initial statistical results. These results show the following:

- Spatter velocity has a general trend of increasing with energy density; however, which energy density variables impact spatter creation and velocity more could not be determined.
- Results for velocity quantities for various laser parameters were presented.
- Spatter vertical angle was averaged to $45.4 \pm 2.14^\circ$ examining each average laser parameter population average compared to each other holding layer thickness constant.
- Results for various laser parameters and resulting average vertical angles were presented.

This work was limited based upon the low cost, high speed cameras used specifically with the inherent 1280x720 resolution and the inability to adjust the shutter speed to reduce the length of the streaks created by the spatter. It is believed that improving the resolution and decreasing the shutter speed will allow for more spatter to be tracked with a higher degree of accuracy, however, this is the first study to the authors knowledge to go into a thorough analysis of a statistical comparison between spatter velocity and quantity, and vertical angle versus a wide range of laser parameters.

Acknowledgments

We would like to thank the Friedman Endowment for Manufacturing at Youngstown State University. This effort was performed in part through the National Center for Defense Manufacturing and Machining under the America Makes Program entitled “Maturation of Advanced Manufacturing for Low Cost Sustainment (MAMLS)” and is based on research sponsored by Air Force Research Laboratory under agreement number FA8650-16-2-5700. The U.S. Government is authorized to reproduce and distribute reprints for Governmental purposes notwithstanding any copyright notation thereon.

7.0 Conclusion

This research has displayed the ability to track spatter created by M-LPBF in a novel approach using high speed stereovision. The velocity and direction of the spatter were able to be determined; thereby, allowing for various laser parameters to be tested for their effect on spatter quantity, velocity, and direction. From the work performed in this research it can be concluded:

- Spatter does negatively impact build creation and cause quality control/assurance issues.
- Low-cost high-speed stereovision can be used to effectively track spatter and was throughout this research.
- A novel code for computer vision was created by altering OpenCV stereovision software and was used for this work.
- Spatter quantity and velocity are directly correlated with three-dimensional energy density.
- It was not able to be determined if scanning speed or laser power had a greater effect on spatter creation or velocity outside of the normal three-dimensional energy equation.
- Spatter vertical angle was shown to not be impacted appreciably by laser power or scanning speed.
- Layer thickness was shown to impact the vertical angle of the spatter.

8.0 Future Work

Future work should focus on purchasing of cameras which have a slower frame per second speed, but more control over the shutter speed and the ability to control them outside the chamber. The improved cameras should also allow for a drastic increase in resolution which should additionally assist the spatter tracking endeavor. Based on the literature, experiments, and general observation, materials such as steel and Inconel produce much larger spatter streaks which can be analyzed far easier. It would be recommended that future work focus on these materials to fully develop this technique and verify the general results across multiple materials.

8.0 References

1. ISO/ASTM 52900:2015, <https://www.iso.org/obp/ui/>
2. Ralph, B.: Method of making decorative articles, <https://patentimages.storage.googleapis.com/83/25/a2/c6e506fcb62cf6/US1533300.pdf>, (1925)
3. du Plessis, A., Yadroitsava, I., Yadroitsev, I.: Ti6Al4V lightweight lattice structures manufactured by laser powder bed fusion for load-bearing applications. *Opt. Laser Technol.* 108, 521–528 (2018)
4. Orme, M., Gschweitl, M., Ferrari, M., Vernon, R., Yancey, R., Mouriaux, F., Madera, I.: A Holistic Process-Flow from Concept to Validation for Additive Manufacturing of Light-Weight, Optimized, Metallic Components Suitable for Space Flight. In: 58th AIAA/ASCE/AHS/ASC Structures, Structural Dynamics, and Materials Conference. American Institute of Aeronautics and Astronautics (2017)
5. Gu, D.D., Meiners, W., Wissenbach, K., Poprawe, R.: Laser additive manufacturing of metallic components: materials, processes and mechanisms. *Int. Mater. Rev.* 57, 133–164 (2012)
6. Murr, L.E., Gaytan, S.M., Ramirez, D.A., Martinez, E., Hernandez, J., Amato, K.N., Shindo, P.W., Medina, F.R., Wicker, R.B.: Metal Fabrication by Additive Manufacturing Using Laser and Electron Beam Melting Technologies. *J. Mater. Sci. Technol.* 28, 1–14 (2012)
7. Garcia-Gonzalez, D., Jayamohan, J., Sotiropoulos, S.N., -H. Yoon, S., Cook, J., Siviour, C.R., Arias, A., Jérusalem, A.: On the mechanical behaviour of PEEK and HA cranial implants under impact loading | Elsevier Enhanced Reader, <https://www.sciencedirect.com/science/article/pii/S1751616117300188/pdf?isDTMRedir=true&download=true>
8. Gayer, C., Ritter, J., Bullemer, M., Grom, S., Jauer, L., Meiners, W., Pfister, A., Reinauer, F., Vučak, M., Wissenbach, K., Fischer, H., Poprawe, R., Schleifenbaum, J.H.: Development of a solvent-free polylactide/calcium carbonate composite for selective laser sintering of bone tissue engineering scaffolds. *Mater. Sci. Eng. C Mater. Biol. Appl.* 101, 660–673 (2019)
9. Lambert, C.S., Jardini, A.L.: Improvement in Cranioplasty: Advanced Prosthesis Biomanufacturing | Elsevier Enhanced Reader, <https://www.sciencedirect.com/science/article/pii/S2212827116302499/pdf?isDTMRedir=true&download=true>
10. Heeling, T., Cloots, M., Wegener, K.: Melt pool simulation for the evaluation of process parameters in selective laser melting. *Additive Manufacturing.* 14, 116–125 (2017)
11. Gao, W., Zhang, Y., Ramanujan, D., Ramani, K., Chen, Y., Williams, C.B., Wang, C.C.L., Shin, Y.C., Zhang, S., Zavattieri, P.D.: The status, challenges, and future of additive manufacturing in engineering. *Comput. Aided Des. Appl.* 69, 65–89 (2015)
12. Mumtaz, K., Hopkinson, N.: Top surface and side roughness of Inconel 625 parts processed using selective laser melting. *Rapid Prototyping Journal.* 15, 96–103 (2009)
13. Choo, H., Sham, K.-L., Bohling, J., Ngo, A., Xiao, X., Ren, Y., Depond, P.J., Matthews, M.J., Garlea, E.: Effect of laser power on defect, texture, and microstructure of a laser powder bed fusion processed 316L stainless steel. *Mater. Des.* 164, 107534 (2019)
14. Spierings, A.B., Levy, G.: Comparison of density of stainless steel 316L parts produced with selective laser melting using different powder grades. In: Proceedings of the Annual International Solid Freeform Fabrication Symposium. pp. 342–353. Austin, TX (2009)
15. Foroozmehr, A., Badrossamay, M., Foroozmehr, E., Golabi, S.: Finite Element Simulation of Selective Laser Melting process considering Optical Penetration Depth of laser in powder

- bed. Mater. Des. 89, 255–263 (2016)
16. Zaeh, M.F., Branner, G.: Investigations on residual stresses and deformations in selective laser melting. *Prod. Eng. Res. Devel.* 4, 35–45 (2009)
 17. Akram, J., Farah, J., Ginn, J., Kumar, P., Misra, M., Teng, C.: Influence of laser processing parameters on porosity in Inconel 718 during additive manufacturing, https://journals.ohiolink.edu/pg_200?414272464282778::NO:200:P200_ARTICLEID,P200_LAST_PAGE,P200_LP_ITEMID:368346273,210,368346273
 18. Keshavarzkermani, A., Marzbanrad, E., Esmaeilzadeh, R., Mahmoodkhani, Y., Ali, U., Enrique, P.D., Zhou, N.Y., Bonakdar, A., Toyserkani, E.: An investigation into the effect of process parameters on melt pool geometry, cell spacing, and grain refinement during laser powder bed fusion. *Opt. Laser Technol.* 116, 83–91 (2019)
 19. Tang, M., Pistorius, P.C., Beuth, J.L.: Prediction of lack-of-fusion porosity for powder bed fusion. *Additive Manufacturing.* 14, 39–48 (2017)
 20. Cutolo, A., Neirinck, B., Lietaert, K., de Formanoir, C., Van Hooreweder, B.: Influence of layer thickness and post-process treatments on the fatigue properties of CoCr scaffolds produced by laser powder bed fusion. *Additive Manufacturing.* 23, 498–504 (2018)
 21. Green light-enabled SLM process to allow additive manufacturing of copper, <https://www.industrial-lasers.com/additive-manufacturing/article/16490235/green-light-enabled-slm-process-to-allow-additive-manufacturing-of-copper>
 22. Zheng, H., Li, H., Lang, L., Gong, S., Ge, Y.: Effects of scan speed on vapor plume behavior and spatter generation in laser powder bed fusion additive manufacturing. *J. Manuf. Process.* 36, 60–67 (2018)
 23. Malekipour, E., El-Mounayri, H.: Common defects and contributing parameters in powder bed fusion AM process and their classification for online monitoring and control: a review. *Int. J. Adv. Manuf. Technol.* 95, 527–550 (2018)
 24. Arisoy, Y.M., Criales, L.E., Özel, T., Lane, B., Moylan, S., Donmez, A.: Influence of scan strategy and process parameters on microstructure and its optimization in additively manufactured nickel alloy 625 via laser powder bed fusion. *Int. J. Adv. Manuf. Technol.* 90, 1393–1417 (2017)
 25. Khairallah, S.A., Anderson, A.T., Rubenchik, A., King, W.E.: Laser powder-bed fusion additive manufacturing: Physics of complex melt flow and formation mechanisms of pores, spatter, and denudation zones. *Acta Mater.* 108, 36–45 (2016)
 26. Esmaeilzadeh, R., Ali, U., Keshavarzkermani, A., Mahmoodkhani, Y., Marzbanrad, E., Toyserkani, E.: On the effect of spatter particles distribution on the quality of Hastelloy X parts made by laser powder-bed fusion additive manufacturing. *J. Manuf. Process.* 37, 11–20 (2019)
 27. Criales, L.E., Arisoy, Y.M., Lane, B., Moylan, S., Donmez, A., Özel, T.: Laser powder bed fusion of nickel alloy 625: Experimental investigations of effects of process parameters on melt pool size and shape with spatter analysis. *Int. J. Mach. Tools Manuf.* 121, 22–36 (2017)
 28. Hooper, P.A.: Melt pool temperature and cooling rates in laser powder bed fusion. *Additive Manufacturing.* 22, 548–559 (2018)
 29. Martin, A.A., Calta, N.P., Khairallah, S.A., Wang, J., Depond, P.J., Fong, A.Y., Thampy, V., Guss, G.M., Kiss, A.M., Stone, K.H., Tassone, C.J., Nelson Weker, J., Toney, M.F., van Buuren, T., Matthews, M.J.: Dynamics of pore formation during laser powder bed fusion additive manufacturing. *Nat. Commun.* 10, 1987 (2019)
 30. Ly, S., Rubenchik, A.M., Khairallah, S.A., Guss, G., Matthews, M.J.: Metal vapor micro-jet controls material redistribution in laser powder bed fusion additive manufacturing. *Sci. Rep.* 7, 4085 (2017)
 31. Matthews, M.J., Guss, G., Khairallah, S.A., Rubenchik, A.M., Depond, P.J., King, W.E.: Denudation of metal powder layers in laser powder bed fusion processes. *Acta Mater.* 114, 33–42 (2016)

32. Masoomi, M., Thompson, S.M., Shamsaei, N.: Laser powder bed fusion of Ti-6Al-4V parts: Thermal modeling and mechanical implications. *Int. J. Mach. Tools Manuf.* 118-119, 73–90 (2017)
33. Demir, A.G., Mazzoleni, L., Caprio, L., Pacher, M., Previtali, B.: Complementary use of pulsed and continuous wave emission modes to stabilize melt pool geometry in laser powder bed fusion. *Opt. Laser Technol.* 113, 15–26 (2019)
34. Bisht, M., Ray, N., Verbist, F., Coeck, S.: Correlation of selective laser melting-melt pool events with the tensile properties of Ti-6Al-4V ELI processed by laser powder bed fusion. *Additive Manufacturing.* 22, 302–306 (2018)
35. Scime, L., Beuth, J.: Using machine learning to identify in-situ melt pool signatures indicative of flaw formation in a laser powder bed fusion additive manufacturing process. *Additive Manufacturing.* 25, 151–165 (2019)
36. Li, W., Li, S., Liu, J., Zhang, A., Zhou, Y., Wei, Q., Yan, C., Shi, Y.: Effect of heat treatment on AlSi10Mg alloy fabricated by selective laser melting: Microstructure evolution, mechanical properties and fracture mechanism. *Materials Science and Engineering: A.* 663, 116–125 (2016)
37. Ammar, H.R., Samuel, A.M., Samuel, F.H.: Porosity and the fatigue behavior of hypoeutectic and hypereutectic aluminum–silicon casting alloys. *Int. J. Fatigue.* 30, 1024–1035 (2008)
38. How and why alloying elements are added to aluminum, <http://www.alcotec.com/us/en/education/knowledge/qa/How-and-why-alloying-elements-are-added-to-aluminum.cfm>
39. EOS GmbH: AlSi10Mg Material data sheet, https://cdn0.scrvt.com/eos/public/8837de942d78d3b3/4e099c3a857fdddca4be9d59fbb1cd74/EOS_Aluminium_AlSi10Mg_en.pdf, (05/2014)
40. Fathi, P., Mohammadi, M., Duan, X., Nasiri, A.M.: A comparative study on corrosion and microstructure of direct metal laser sintered AlSi10Mg_200C and die cast A360.1 aluminum. *J. Mater. Process. Technol.* 259, 1–14 (2018)
41. Zygula, K., Nosek, B., Pasiowiec, H., Szysiak, N.: Mechanical properties and microstructure of AlSi10Mg alloy obtained by casting and SLM technique. *World Scientific News.* 104, 462–472 (2018)
42. Aboulkhair, N.T., Maskery, I., Tuck, C., Ashcroft, I., Everitt, N.M.: The microstructure and mechanical properties of selectively laser melted AlSi10Mg: The effect of a conventional T6-like heat treatment. *Materials Science and Engineering: A.* 667, 139–146 (2016)
43. Zhou, W., Aung, N.N., Choudhary, A., Kanouni, M.: Heat-transfer corrosion behaviour of cast Al alloy. *Corros. Sci.* 50, 3308–3313 (2008)
44. Liu, X., Zhao, C., Zhou, X., ZhijianShen, Liu, W.: Microstructure of selective laser melted AlSi10Mg alloy | Elsevier Enhanced Reader, <https://www.sciencedirect.com/science/article/pii/S0264127519301145/pdf?isDTMRedir=true&download=true>
45. Wei, H.L., Elmer, J.W., DebRoy, T.: Origin of grain orientation during solidification of an aluminum alloy. *Acta Mater.* 115, 123–131 (2016)
46. Koepf, J.A., Gotterbarm, M.R., Markl, M.: 3D multi-layer grain structure simulation of powder bed fusion additive manufacturing | Elsevier Enhanced Reader, <https://www.sciencedirect.com/science/article/pii/S1359645418303070/pdf?isDTMRedir=true&download=true>
47. Thijs, L., Kempen, K., Kruth, J.-P., Van Humbeeck, J.: Fine-structured aluminium products with controllable texture by selective laser melting of pre-alloyed AlSi10Mg powder. *Acta Mater.* 61, 1809–1819 (2013)
48. Qin, H., Fallah, V., Dong, Q., Brochu, M., Daymond, M.R., Gallerneault, M.: Solidification pattern, microstructure and texture development in Laser Powder Bed Fusion (LPBF) of

- Al10SiMg alloy. *Mater. Charact.* 145, 29–38 (2018)
49. King, W.E., Barth, H.D., Castillo, V.M., Gallegos, G.F., Gibbs, J.W., Hahn, D.E., Kamath, C., Rubenchik, A.M.: Observation of keyhole-mode laser melting in laser powder-bed fusion additive manufacturing. *J. Mater. Process. Technol.* 214, 2915–2925 (2014)
 50. Cunningham, R., Narra, S.P., Montgomery, C., Beuth, J., Rollett, A.D.: Synchrotron-Based X-ray Microtomography Characterization of the Effect of Processing Variables on Porosity Formation in Laser Powder-Bed Additive Manufacturing of Ti-6Al-4V. *JOM.* 69, 479–484 (2017)
 51. Foster, B.K., Reutzel, E.W., Nassar, A.R., Hall, B.T., Brown, S.W., Dickman, C.J.: Optical, layerwise monitoring of powder bed fusion. In: *Solid Freedom Fabrication Symp. Proc.* (2015)
 52. Brown, A.: *Classification, Effects, and Prevention of Build Defects in Powder-bed Fusion Printed Inconel 718.* TMS. , San Diego, California (2017)
 53. Everton, S.K., Hirsch, M., Stravroulakis, P., Leach, R.K., Clare, A.T.: Review of in-situ process monitoring and in-situ metrology for metal additive manufacturing. *Mater. Des.* 95, 431–445 (2016)
 54. Gong, H., Rafi, K., Gu, H., Starr, T., Stucker, B.: Analysis of defect generation in Ti-6Al-4V parts made using powder bed fusion additive manufacturing processes. *Additive Manufacturing.* 1-4, 87–98 (2014)
 55. Gong, H.: Generation and detection of defects in metallic parts fabricated by selective laser melting and electron beam melting and their effects on mechanical properties, <https://ir.library.louisville.edu/etd/515/>, (2013)
 56. Qiu, C., Panwisawas, C., Ward, M., Basoalto, H.C., Brooks, J.W., Attallah, M.M.: On the role of melt flow into the surface structure and porosity development during selective laser melting. *Acta Mater.* 72 (2015)
 57. Nassar, A.R., Gundermann, M.A., Reutzel, E.W., Guerrier, P., Krane, M.H., Weldon, M.J.: Formation processes for large ejecta and interactions with melt pool formation in powder bed fusion additive manufacturing. *Sci. Rep.* 9, 5038 (2019)
 58. Definition of SPATTER, <https://www.merriam-webster.com/dictionary/spatter>
 59. Yadroitsev, I., Gusarov, A., Yadroitsava, I., Smurov, I.: Single track formation in selective laser melting of metal powders. *J. Mater. Process. Technol.* 210, 1624–1631 (2010)
 60. Wang, D., Wu, S., Fu, F., Mai, S., Yang, Y., Liu, Y., Song, C.: Mechanisms and characteristics of spatter generation in SLM processing and its effect on the properties. *Mater. Des.* 117, 121–130 (2017)
 61. Gunenthiram, V., Peyre, P., Schneider, M., Dal, M., Coste, F., Koutiri, I., Fabbro, R.: Experimental analysis of spatter generation and melt-pool behavior during the powder bed laser beam melting process. *J. Mater. Process. Technol.* 251, 376–386 (2018)
 62. Christopher Barrett, Jason Walker, Rodrigo Enriquez Gutierrez, Eric MacDonald, Brett Conner: *A Low Cost, High-speed Optical Monitoring System for Tracking Spatter During Laser Powder Bed Fusion.* TMS 2018. , Phoenix, AZ (2018)
 63. Kneen, T.J.: *Characterizing the High Strain Rate Mechanical Behavior of Stainless Steel 316L Processed by Selective Laser Melting,* (2016)
 64. Ladewig, A., Schlick, G., Fisser, M., Schulze, V., Glatzel, U.: Influence of the shielding gas flow on the removal of process by-products in the selective laser melting process. *Additive Manufacturing.* 10, 1–9 (2016)
 65. Taheri Andani, M., Dehghani, R., Karamooz-Ravari, M.R., Mirzaeifar, R., Ni, J.: Spatter formation in selective laser melting process using multi-laser technology. *Mater. Des.* 131, 460–469 (2017)
 66. Taheri Andani, M., Dehghani, R., Karamooz-Ravari, M.R., Mirzaeifar, R., Ni, J.: A study on the effect of energy input on spatter particles creation during selective laser melting process. *Additive Manufacturing.* 20, 33–43 (2018)

67. You, D., Gao, X., Katayama, S.: Monitoring of high-power laser welding using high-speed photographing and image processing. *Mech. Syst. Signal Process.* 49, 39–52 (2014)
68. Bi, G., Gasser, A., Wissenbach, K., Drenker, A., Poprawe, R.: Identification and qualification of temperature signal for monitoring and control in laser cladding. *Opt. Lasers Eng.* 44, 1348–1359 (2006)
69. Bardin, F., Cobo, A., Lopez-Higuera, J.M., Collin, O., Aubry, P., Dubois, T., Högström, M., Nylen, P., Jonsson, P., Jones, J.D.C., Hand, D.P.: Optical techniques for real-time penetration monitoring for laser welding. *Appl. Opt.* 44, 3869–3876 (2005)
70. Berumen, S., Bechmann, F., Lindner, S., Kruth, J.-P., Craeghs, T.: Quality control of laser- and powder bed-based Additive Manufacturing (AM) technologies. *Phys. Procedia.* 5, 617–622 (2010)
71. Clijsters, S., Craeghs, T., Buls, S., Kempen, K., Kruth, J.-P.: In situ quality control of the selective laser melting process using a high-speed, real-time melt pool monitoring system. *Int. J. Adv. Manuf. Technol.* 75, 1089–1101 (2014)
72. Lott, P., Schleifenbaum, H., Meiners, W., Wissenbach, K., Hinke, C., Bültmann, J.: Design of an Optical system for the In Situ Process Monitoring of Selective Laser Melting (SLM). *Phys. Procedia.* 12, Part A, 683–690 (2011)
73. Bidare, P., Bitharas, I., Ward, R.M., Attallah, M.M., Moore, A.J.: Fluid and particle dynamics in laser powder bed fusion. *Acta Mater.* 142, 107–120 (2018)
74. Scipioni Bertoli, U., Guss, G., Wu, S., Matthews, M.J., Schoenung, J.M.: In-situ characterization of laser-powder interaction and cooling rates through high-speed imaging of powder bed fusion additive manufacturing. *Mater. Des.* 135, 385–396 (2017)
75. Rao, P.K., Liu, J. (peter), Roberson, D., Kong, Z. (james), Williams, C.: Online Real-Time Quality Monitoring in Additive Manufacturing Processes Using Heterogeneous Sensors. *J. Manuf. Sci. Eng.* 137, 061007 (2015)
76. Zanini, F., Sbettega, E., Carmignato, S.: X-ray computed tomography for metal additive manufacturing: challenges and solutions for accuracy enhancement. *Procedia CIRP.* 75, 114–118 (2018)
77. Thompson, A., McNally, D., Maskery, I., Leach, R.K.: X-ray computed tomography and additive manufacturing in medicine: a review. *International Journal of Metrology & Quality Engineering.* 8, 1–15 (2017)
78. Repossini, G., Laguzza, V., Grasso, M., Colosimo, B.M.: On the use of spatter signature for in-situ monitoring of Laser Powder Bed Fusion. *Additive Manufacturing.* 16, 35–48 (2017)
79. Liu, Y., Yang, Y., Mai, S., Wang, D., Song, C.: Investigation into spatter behavior during selective laser melting of AISI 316L stainless steel powder. *Mater. Des.* 87, 797–806 (2015)
80. Simonelli, M., Tuck, C., Aboulkhair, N.T., Maskery, I., Ashcroft, I., Wildman, R.D., Hague, R.: A Study on the Laser Spatter and the Oxidation Reactions During Selective Laser Melting of 316L Stainless Steel, Al-Si10-Mg, and Ti-6Al-4V. *Metall. Mater. Trans. A.* 46, 3842–3851 (2015)
81. Craeghs, T., Bechmann, F., Berumen, S., Kruth, J.-P.: Feedback control of Layerwise Laser Melting using optical sensors. *Phys. Procedia.* 5, Part B, 505–514 (2010)
82. Doubenskaia, M., Pavlov, M., Grigoriev, S., Tikhonova, E., Smurov, I.: Comprehensive optical monitoring of selective laser melting. *Journal of Laser Micro Nanoengineering.* 7, 236–243 (2012)
83. Chivel, Y.: Optical In-Process Temperature Monitoring of Selective Laser Melting. *Phys. Procedia.* 41, 904–910 (2013)
84. Kanko, J.A., Sibley, A.P., Fraser, J.M.: In situ morphology-based defect detection of selective laser melting through inline coherent imaging. *J. Mater. Process. Technol.* 231, 488–500 (2016/5)
85. Yadroitsev, I., Krakhmalev, P., Yadroitsava, I.: Selective laser melting of Ti6Al4V alloy for biomedical applications: Temperature monitoring and microstructural evolution. *J. Alloys*

- Compd. 583, 404–409 (2014)
86. Krauss, H., Eschey, C., Zaeh, M.: Thermography for monitoring the selective laser melting process. In: Proceedings of the Solid Freeform Fabrication Symposium (2012)
 87. Lane, B., Moylan, S., Whitenon, E., Ma, L.: Thermographic Measurements of the Commercial Laser Powder Bed Fusion Process at NIST. *Rapid Prototyp J.* 22, 778–787 (2016)
 88. Bayle, F., Doubenskaia, M.: Selective laser melting process monitoring with high speed infra-red camera and pyrometer. In: Fundamentals of Laser Assisted Micro- and Nanotechnologies. pp. 698505–698505–8. International Society for Optics and Photonics (2008)
 89. Grasso, M., Laguzza, V., Semeraro, Q., Colosimo, B.M.: In-Process Monitoring of Selective Laser Melting: Spatial Detection of Defects Via Image Data Analysis. *J. Manuf. Sci. Eng.* 139, 051001 (2017)
 90. Alena Mudroch, Jose M. Azcue, Paul Mudroch ed: Manual of Physico-Chemical Analysis of Aquatic Sediments. CRC Press (1996)
 91. McCave, I.N., Bryant, R.J., Cook, H.F., Coughanowr, C.A.: Evaluation of a laser-diffraction-size analyzer for use with natural sediments. *J. Sediment. Res.* 56, 561–564 (1986)
 92. ASTM: ASTM E8/E8M - 16a. ASTM International, 100 Barr Harbor Drive, PO Box C700, West Conshohocken, PA 19428-2959, United States (2015)
 93. Land, W.S., Zhang, B., Ziegert, J., Davies, A.: In-Situ Metrology System for Laser Powder Bed Fusion Additive Process. *Procedia Manufacturing.* 1, 393–403 (2015)
 94. Barrett, C., Carradero-Santiago, C., Harris, E., Mc Knight, J., Walker, J., MacDonald, E., Conner, B.: Low Cost, High Speed Stereovision for Spatter Tracking in Laser Powder Bed Fusion. In: Solid Freeform Fabrication Symposium
 95. Dunbar, A.J., Denlinger, E.R., Heigel, J., Michaleris, P., Guerrier, P., Martukanitz, R., Simpson, T.W.: Development of experimental method for in situ distortion and temperature measurements during the laser powder bed fusion additive manufacturing process. *Additive Manufacturing.* 12, 25–30 (2016)
 96. Bobel, A., Hector, L.G., Chelladurai, I., Sachdev, A.K., Brown, T., Poling, W.A., Kubic, R., Gould, B., Zhao, C., Parab, N., Greco, A., Sun, T.: In situ synchrotron X-ray imaging of 4140 steel laser powder bed fusion. *Materialia.* 6, 100306 (2019)
 97. Guo, Q., Zhao, C., Escano, L.I., Young, Z., Xiong, L., Fezzaa, K., Everhart, W., Brown, B., Sun, T., Chen, L.: Transient dynamics of powder spattering in laser powder bed fusion additive manufacturing process revealed by in-situ high-speed high-energy x-ray imaging. *Acta Mater.* 151, 169–180 (2018)
 98. Zhao, C., Fezzaa, K., Cunningham, R.W., Wen, H., De Carlo, F., Chen, L., Rollett, A.D., Sun, T.: Real-time monitoring of laser powder bed fusion process using high-speed X-ray imaging and diffraction. *Sci. Rep.* 7, 3602 (2017)
 99. Barrett, C., Carradero, C., Harris, E., Rogers, K., MacDonald, E., Conner, B.: Statistical analysis of spatter velocity with high-speed stereovision in laser powder bed fusion. *Prog Addit Manuf.* 5, 617 (2019)

9.0 Publications & Conferences

I. Publications in Professional Journals

101. Barrett, C., Harris, E., MacDonald, E., Conner, B: Computer Vision for Spatter Motion Analysis in Relation to Process Parameters for Laser Powder Bed Fusion. Additive Manufacturing (To Be Submitted 12/2019)

99. Barrett, C., Carradero, C., Harris, E., Rogers, K., MacDonald, E., Conner, B.: Statistical analysis of spatter velocity with high-speed stereovision in laser powder bed fusion. Prog Addit Manuf. 4, 423–430 (2019)

100. Barrett, C., MacDonald, E., Conner, B., Persi, F.: Micron-Level Layer-Wise Surface Profilometry to Detect Porosity Defects in Powder Bed Fusion of Inconel 718. JOM. 70, 1844–1852 (2018)

94. Barrett, C., Carradero-Santiago, C., Harris, E., Mc Knight, J., Walker, J., MacDonald, E., Conner, B.: Low cost, high speed stereovision for spatter tracking in laser powder bed fusion. In: Solid freeform fabrication symposium (2018)

II. Contributions to International Conferences

1. Travis Kneen, Christopher Barrett, Brett Conner, Guha Manogharan: High Strain Rate Mechanical Behavior of Stainless Steel 316L Processed by Selective Laser Melting. TMS 2017. San Diego, CA (2017)

2. Christopher Barrett, Jason Walker, Rodrigo Enriquez Gutierrez, Brian Vuksanovich, Eric MacDonald, Brett Conner: High Speed, High Resolution In Situ Monitoring of Spatter during Laser Powder Bed Fusion. MS&T 2017. Pittsburgh, PA (2017)

3. Christopher Barrett, Jason Walker, Rodrigo Enriquez Gutierrez, Eric MacDonald, Brett Conner: A Low Cost, High-speed Optical Monitoring System for Tracking Spatter During Laser Powder Bed Fusion. TMS 2018. Phoenix, AZ (2018)
4. Christopher Barrett, Carolyn Carradero, Evan Harris, Jeremy McKnight, Eric MacDonald, Brett Conner: Low Cost, High Speed Stereovision for Spatter Tracking in Laser Powder Bed Fusion. MS&T 2018. Columbus, OH (2018)

Appendix A: Single Camera Rectification Code

camMatrix.cpp

```
#include <opencv2/core.hpp>
#include <opencv2/imgcodecs.hpp>
#include <opencv2/imgproc.hpp>
#include <opencv2/highgui.hpp>
#include <opencv2/calib3d.hpp>
#include <opencv2/dictionary.hpp>
#include <opencv2/charuco.hpp>
#include <sstream>
#include <iostream>
#include <fstream>

using namespace std;
using namespace cv;

void createBoard(Size board, float boardEdge, vector<Point3f>& corners);
void getChessBoardCorners( vector<Mat> images,vector<vector<Point2f>>&
allFoundCorners, bool ShowResults, Size board, Size imsize);
void camCalibration(vector<Mat> CallImages,Size board, float boardEdge, Mat& K, Mat&
D, Size imsize);
bool saveCamCalibration(string name, Mat K, Mat D);
void evaluateImages( vector<Mat>& CallImages, Size board, float boardEdge, Mat K, Mat
D, Size imsize);

const float calSquareDim = 0.015f;//meters
const Size ChessBoardDim = Size(10,7);

int main(int argc, char** argv)
{

    Mat Frame;
    Mat DrawToFrame;
    Mat K = Mat::eye(3,3,CV_64F);
    Mat D;
    vector<Mat> savedImages;
    vector<vector<Point2f>> MarkerCorners, rejectedCandidates;

    if (argc != 3)
```

```

    {

        cout << "./camCalbration [video.avi] [filename]"<< endl;
        return -1;

    }

VideoCapture vid;
vid.open(argv[1]);

if (!vid.isOpened())
{
    return -1;
}

cout << "Press 0 to save image."<<endl;
cout << "Press 1 to start calibration." << endl;
cout << "Press ESC to quit." << endl;
int count = 1;
Size imsize;
while(1)
{

    if (!vid.read(Frame))
    {
        break;
    }
    imsize = Frame.size();
    vector<Point2f> foundPoints;
    bool found = false;
    Mat temp;
    //int alpha = 1.5; //contrast control
    //int beta = 25.0; //brightness control
    //Frame.convertTo(Frame, -1, alpha, beta);

    found = findChessboardCorners(Frame, ChessBoardDim,
foundPoints, CALIB_CB_ADAPTIVE_THRESH | CALIB_CB_NORMALIZE_IMAGE);

    Frame.copyTo(DrawToFrame);

```

```

drawChessboardCorners(DrawToFrame, ChessBoardDim,foundPoints,found);

if (found)
    {
    Mat resized, temp;
    resize(DrawToFrame, resized, Size(640,480),0.0,0.0, INTER_LINEAR);
    Frame.copyTo(temp);
    savedImages.push_back(temp);
    }
else
    {
    Mat resized;
    resize(Frame, resized, Size(640,480),0.0,0.0, INTER_LINEAR);
    }

}
}

void createBoard(Size board, float boardEdge, vector<Point3f>& corners)
{
for(int i = 0; i < board.height;i++)
    {
for(int j = 0; j < board.width;j++)
    {
corners.push_back(Point3f(j* boardEdge, i*boardEdge, 0.0f)); //z = 0 because
planar
    }
}
}

void getChessBoardCorners( vector<Mat> images,vector<vector<Point2f>>&
allFoundCorners, bool ShowResults, Size board, Size imsize)
{

for(vector<Mat>::iterator iter= images.begin(); iter != images.end() ; iter++)
    {
vector<Point2f> pointBuf;
bool found = findChessboardCorners(*iter, board,
pointBuf,CALIB_CB_ADAPTIVE_THRESH | CALIB_CB_NORMALIZE_IMAGE);

```

```

    if (found)
    {
        allFoundCorners.push_back(pointBuf);
    }
    if (ShowResults)
    {
        drawChessboardCorners(*iter, board, pointBuf, found);
        imshow("Corners", *iter);
        waitKey(0);
    }
}
}

```

```

void evaluateImages( vector<Mat>& CalImages, Size board, float boardEdge, Mat K, Mat
D, Size imsize)

```

```

{

    vector<vector<Point2f>> CheckImageSpacePnts;
    getChessBoardCorners(CalImages, CheckImageSpacePnts, false, board, imsize);
    vector<vector<Point3f>> euclidSpaceCornerPoints(1);
    createBoard(board,boardEdge, euclidSpaceCornerPoints[0]);
    euclidSpaceCornerPoints.resize(CheckImageSpacePnts.size(),
euclidSpaceCornerPoints[0]);
    vector<Mat> goodIms;

    vector<Mat> RVecs,TVecs;
    D = Mat::zeros(8,1,CV_64F);

    cout << "Reprojection Errors: " << endl;
    int count = 0;

    double rpg_error;
    for (int i = 0; i < CheckImageSpacePnts.size(); i++)
    {
        Mat draw;
        CalImages[i].copyTo(draw);
        vector<vector<Point2f>> Points1, Points2;
        Points1.push_back(CheckImageSpacePnts[i]);
    }
}

```

```

vector<Vec2f> foundPoints;
bool found = findChessboardCorners(CallImages[i],ChessBoardDim,
foundPoints,CALIB_CB_ADAPTIVE_THRESH|CALIB_CB_NORMALIZE_IMAGE);

drawChessboardCorners(draw, ChessBoardDim,foundPoints,found);

vector<vector<Point3f>> buf_euclidPoints;
buf_euclidPoints.push_back(euclidSpaceCornerPoints[i]);
rpg_error = calibrateCamera(buf_euclidPoints, Points1, imsize, K, D, RVecs, TVecs,
0);

cout << "Image[" << i << "] = " << rpg_error << endl;

imshow("Image",draw);

char character = waitKey(0);
if (character==33) break;

switch (character)
{
case 48: //save image
if(found)
{
Mat temp;
CallImages[i].copyTo(temp);
goodIms.push_back(temp);
cout<<"Image" << count <<" saved!"<<endl;
count += 1;
}
break;
case 49: //start calibration
if(goodIms.size(>15)
{
cout << "Starting calibration..." << endl;
break;
}
else{cout<<"Pictures did not exceed 15"<<endl;}
break;
case 27: //exit

```

```

        break;
    }
}
CallImages = goodIms;
}

void camCalibration(vector<Mat> CallImages, Size board, float boardEdge, Mat& K, Mat&
D, Size imsize)
{

    vector<vector<Point2f>> CheckImageSpacePnts;
    getChessBoardCorners(CallImages, CheckImageSpacePnts, false, board, imsize);
    vector<vector<Point3f>> euclidSpaceCornerPoints(1);
    createBoard(board, boardEdge, euclidSpaceCornerPoints[0]);
    euclidSpaceCornerPoints.resize(CheckImageSpacePnts.size(),
euclidSpaceCornerPoints[0]);

    vector<Mat> RVecs, TVecs;
    D = Mat::zeros(8, 1, CV_64F);

    cout << imsize << endl;
    double rpgerror = calibrateCamera(euclidSpaceCornerPoints, CheckImageSpacePnts,
imsize, K, D, RVecs, TVecs, 0);

    cout << "Total Re-projection Error: " << rpgerror << endl;

}

bool saveCamCalibration(string name, Mat K, Mat D)
{
    ofstream outStream(name);
    if(outStream)
    {

        uint16_t rows = K.rows;
        uint16_t columns = K.cols;

        outStream << rows << endl;
        outStream << columns << endl;
    }
}

```

```

for(int r = 0; r < rows; r++)
{
    for(int c = 0; c < columns; c++)
    {
        double value = K.at<double>(r,c);
        outputStream << value << endl;
    }
}

rows = D.rows;
columns = D.cols;

outputStream << rows << endl;
outputStream << columns << endl;

for(int r = 0; r < rows; r++)
{
    for(int c = 0; c < columns; c++)
    {
        double value = D.at<double>(r,c);
        outputStream << value << endl;
    }
}

outputStream.close();
return true;
}

return false;
}

```


Appendix B: Stereo Calibration Code

stereoCalibration.cpp

```
#include <opencv2/core.hpp>
#include <opencv2/imgcodecs.hpp>
#include <opencv2/imgproc.hpp>
#include <opencv2/highgui.hpp>
#include <opencv2/aruco.hpp>
#include <opencv2/calib3d.hpp>
#include <opencv2/dictionary.hpp>
#include <opencv2/charuco.hpp>
#include <sstream>
#include <iostream>
#include <fstream>

using namespace std;
using namespace cv;
using namespace cv::aruco;

const float calSquareDim = 0.015f;//meters
const float aurSquareDim = 0.1325f; //meters
const Size ChessBoardDim = Size(10,7);

void rotateConcat(Mat img1, Mat img2, Mat& out, int scale, bool save);

void rotateConcat(Mat img1, Mat img2, Mat& out, int scale, bool save)
{
    CV_Assert(img1.size() == img2.size() && img1.type() == img2.type());

    Mat outImg(img1.cols,2*img1.rows, img1.type());
    Rect rect1(0,0, img1.rows, img1.cols);
    Rect rect2(img1.rows,0, img1.rows, img1.cols);

    transpose(img1, img1);
    transpose(img2, img2);
    flip(img1, img1,1);
    flip(img2, img2,1);

    img1.copyTo(outImg(rect1));
```

```

img2.copyTo(outImg(rect2));

if (save)
{
    imshow("Image",outImg);
    waitKey(0);
    imwrite("result.jpg",outImg);
}
resize(outImg,out,Size(outImg.cols/scale,outImg.rows/scale));
}

void createKnownBoardPositions(Size BoardSize, float SquareEdgeLength,
vector<Point3f>& corners)
{
    for(int i = 0; i < BoardSize.height;i++)
    {
        for(int j = 0; j < BoardSize.width;j++)
        {
            corners.push_back(Point3f(j* SquareEdgeLength, i*SquareEdgeLength, 0.0f)); //z
= 0 because planar
        }
    }
}

bool loadCameraCalibration(string name,Mat& CameraMatrix, Mat& DistanceCoe)
{
    ifstream instream(name);

    if(instream)
    {
        uint16_t rows;
        uint16_t columns;

        instream >> rows;
        instream >> columns;

        CameraMatrix = Mat::zeros(rows,columns, CV_64F);
    }
}

```

```

for(int r = 0; r< rows;r++)
{
    for(int c = 0; c< columns; c++)
    {
        double read = 0.0f;
        instream >> read;
        CameraMatrix.at<double>(r,c) = read;
        cout << CameraMatrix.at<double>(r,c) << "\n";
    }
}

instream >> rows;
instream >> columns;

DistanceCoe = Mat::zeros(rows,columns, CV_64F);

for(int r = 0; r< rows;r++)
{
    for(int c = 0; c< columns; c++)
    {
        double read = 0.0f;
        instream >> read;
        DistanceCoe.at<double>(r,c) = read;
        cout << DistanceCoe.at<double>(r,c) << "\n";
    }
}
instream.close();
return true;

}

return false;
}

void getChessBoardCorners( vector<Mat> images,vector<vector<Point2f>>&
allFoundCorners, bool ShowResults, Size BoardSize,Size imsize)
{
    for(vector<Mat>::iterator iter= images.begin(); iter != images.end() ; iter++)
    {

```

```

    vector<Point2f> pointBuf;
    Mat resized;
    bool found = findChessboardCorners(*iter, BoardSize, pointBuf,
CALIB_CB_ADAPTIVE_THRESH | CALIB_CB_NORMALIZE_IMAGE);

    if (found)
    {
        allFoundCorners.push_back(pointBuf);
    }
    if (ShowResults)
    {
        drawChessboardCorners(*iter, BoardSize, pointBuf, found);
        imshow("Corners", *iter);
        waitKey(0);
    }
}
}

```

```

void stereoCalibration(vector<Mat> CalImages1, vector<Mat> CalImages2, Size
BoardSize, float SquareEdgeLength, Mat& CameraMatrix1, Mat& distortionCoe1, Mat&
CameraMatrix2, Mat& distortionCoe2, Mat& RotationMatrix, Mat& TranslationVector,
Mat& EssentialMatrix, Mat& FundamentalMatrix, Size imsize)
{
    vector<vector<Point2f>> CheckImageSpacePnts1, CheckImageSpacePnts2;
    getChessBoardCorners(CalImages1, CheckImageSpacePnts1, false, BoardSize, imsize);
    getChessBoardCorners(CalImages2, CheckImageSpacePnts2, false, BoardSize, imsize);

    vector<vector<Point3f>> euclidSpaceCornerPoints(1);
    createKnownBoardPositions(BoardSize, SquareEdgeLength,
euclidSpaceCornerPoints[0]);
    euclidSpaceCornerPoints.resize(CheckImageSpacePnts1.size(),
euclidSpaceCornerPoints[0]);

    cout << "Reprojection Errors: " << endl;

    double rpg_error;
    for (int i = 0; i < CheckImageSpacePnts1.size(); i++)
    {
        Mat both, draw1, draw2;
    }
}

```

```

CallImages1[i].copyTo(draw1);
CallImages2[i].copyTo(draw2);

vector<vector<Point2f>> Points1, Points2;
Points1.push_back(CheckImageSpacePnts1[i]);
Points2.push_back(CheckImageSpacePnts2[i]);

vector<Vec2f> foundPoints1, foundPoints2;
bool found1 = findChessboardCorners(CallImages1[i],ChessBoardDim,
foundPoints1,CALIB_CB_ADAPTIVE_THRESH
CALIB_CB_NORMALIZE_IMAGE);
bool found2 = findChessboardCorners(CallImages2[i],ChessBoardDim,
foundPoints2,CALIB_CB_ADAPTIVE_THRESH
CALIB_CB_NORMALIZE_IMAGE);

drawChessboardCorners(draw1, ChessBoardDim,foundPoints1,found1);
drawChessboardCorners(draw2, ChessBoardDim,foundPoints2,found2);

vector<vector<Point3f>> buf_euclidPoints;
buf_euclidPoints.push_back(euclidSpaceCornerPoints[i]);

rpg_error = stereoCalibrate(buf_euclidPoints, Points1,Points2,CameraMatrix1,
distortionCoe1, CameraMatrix2, distortionCoe2, imsize, RotationMatrix,
TranslationVector, EssentialMatrix, FundamentalMatrix, CALIB_FIX_INTRINSIC);
cout << "Image[" << i << "] = " << rpg_error << endl;
rotateConcat(draw1,draw2,both,2,false);
imshow("Images",both);
waitKey(0);
if (rpg_error > 1.0)
{
    CallImages1.erase(CallImages1.begin() + i);
    CallImages2.erase(CallImages2.begin() + i);
    euclidSpaceCornerPoints.erase(euclidSpaceCornerPoints.begin() + i);
    CheckImageSpacePnts1.erase(CheckImageSpacePnts1.begin() + i);
    CheckImageSpacePnts2.erase(CheckImageSpacePnts2.begin() + i);
    i -= 1;
}
}

```

```

    rpg_error = stereoCalibrate(euclidSpaceCornerPoints, CheckImageSpacePnts1,
    CheckImageSpacePnts2, CameraMatrix1, distortionCoe1, CameraMatrix2,
    distortionCoe2, imsize, RotationMatrix, TranslationVector, EssentialMatrix,
    FundamentalMatrix, CALIB_FIX_INTRINSIC);
    cout << "Reprojection Error Mean(after removing bad images) = " << rpg_error << endl;
}

```

```

bool saveStereoCalibration(string name, Mat CameraMatrixL, Mat distortionCoeL,Mat
CameraMatrixR, Mat distortionCoeR,Mat TranslationVector,Mat EssentialMatrix, Mat
FundamentalMatrix, Mat RotationMatrix)

```

```

{
    ofstream outStream(name);
    if(outStream)
    {

        uint16_t rows = CameraMatrixL.rows;
        uint16_t columns = CameraMatrixL.cols;

        outStream << rows << endl;
        outStream << columns << endl;

        for(int r = 0; r< rows; r++)
        {
            for(int c = 0; c< columns; c++)
            {
                double value = CameraMatrixL.at<double>(r,c);
                outStream << value << endl;
            }
        }

        rows = distortionCoeL.rows;
        columns = distortionCoeL.cols;

        outStream << rows << endl;
        outStream << columns << endl;

        for(int r = 0; r< rows; r++)
        {
            for(int c = 0; c< columns; c++)

```

```

        {
            double value = distortionCoeL.at<double>(r,c);
            outStream << value << endl;
        }
    }

rows = CameraMatrixR.rows;
columns = CameraMatrixR.cols;

outStream << rows << endl;
outStream << columns << endl;

for(int r = 0; r< rows; r++)
    {
        for(int c = 0; c< columns; c++)
            {
                double value = CameraMatrixR.at<double>(r,c);
                outStream << value << endl;
            }
    }

rows = distortionCoeR.rows;
columns = distortionCoeR.cols;

outStream << rows << endl;
outStream << columns << endl;

for(int r = 0; r< rows; r++)
    {
        for(int c = 0; c< columns; c++)
            {
                double value = distortionCoeR.at<double>(r,c);
                outStream << value << endl;
            }
    }

rows = TranslationVector.rows;
columns = TranslationVector.cols;

outStream << rows << endl;

```

```

outStream << columns << endl;

for(int r = 0; r< rows; r++)
    {
        for(int c = 0; c< columns; c++)
            {
                double value = TranslationVector.at<double>(r,c);
                outStream << value << endl;
            }
    }

rows = EssentialMatrix.rows;
columns = EssentialMatrix.cols;

outStream << rows << endl;
outStream << columns << endl;

for(int r = 0; r< rows; r++)
    {
        for(int c = 0; c< columns; c++)
            {
                double value = EssentialMatrix.at<double>(r,c);
                outStream << value << endl;
            }
    }

rows = FundamentalMatrix.rows;
columns = FundamentalMatrix.cols;

outStream << rows << endl;
outStream << columns << endl;

for(int r = 0; r< rows; r++)
    {
        for(int c = 0; c< columns; c++)
            {
                double value = FundamentalMatrix.at<double>(r,c);
                outStream << value << endl;
            }
    }

```



```

    }

    rows = RotationMatrix.rows;
    columns = RotationMatrix.cols;

    outputStream << rows << endl;
    outputStream << columns << endl;

    for(int r = 0; r < rows; r++)
    {
        for(int c = 0; c < columns; c++)
        {
            double value = RotationMatrix.at<double>(r,c);
            outputStream << value << endl;
        }
    }

    outputStream.close();
    return true;

}
return false;
}

void printMat(Mat inputMatrix)
{

    uint16_t rows = inputMatrix.rows;
    uint16_t columns = inputMatrix.cols;

    for(int r = 0; r < rows; r++)
    {
        for(int c = 0; c < columns; c++)
        {
            double value = inputMatrix.at<double>(r,c);
            cout << "(" << r << ", " << c << ") = " << value << endl;
        }
    }
}

```

```

int main(int argc, char** argv)
{

    Mat FrameL, FrameR;
    Mat DrawToFrameL, DrawToFrameR;
    Mat KL = Mat::eye(3,3,CV_64F); //Camera Calibration matrix L
    Mat KR = Mat::eye(3,3,CV_64F); //Camera Calibration Matrix R
    Mat DL, DR = Mat::zeros(8,1,CV_64F); //Distortion Coefficients
    Mat E, T, F, R; //Essential, Translation, Fundamental, Rotation
    vector<Mat> savedImagesR, savedImagesL;
    VideoCapture videoL,videoR;
    Mat dummy, M1L,M2L,M1R,M2R; //Map vectors for remap --> Dummy is an empty
matrix

    videoL.open(argv[1]);///"/home/e5m9/Desktop/Programs/C++/stereoCalibrate/left.avi");

    videoR.open(argv[2]);///"/home/e5m9/Desktop/Programs/C++/stereoCalibrate/right.avi");

    double height = videoL.get(CAP_PROP_FRAME_HEIGHT);
    double width = videoL.get(CAP_PROP_FRAME_WIDTH);
    Size imsize = Size(width, height);

    if (argc != 3)
    {
        cout << "Not enough arguments: ";
        cout <<"/stereoCalib [left video] [right video]"<<endl;
        return -1;
    }

    loadCameraCalibration("L_camMatrix", KL, DL);
    loadCameraCalibration("R_camMatrix", KR, DR);

    //initUndistortRectifyMap(KR,DR, dummy, KR, imsize , CV_16SC2, M1R, M2R);
    //initUndistortRectifyMap(KL,DL, dummy, KL, imsize , CV_16SC2, M1L, M2L);

    if (!videoL.isOpened() | !videoR.isOpened())
    {
        return -1;
    }
}

```

```

}

namedWindow("Left Cam",WINDOW_AUTOSIZE);
namedWindow("Right Cam",WINDOW_AUTOSIZE);
int count = 0;

while(1)
{
    if (!videoL.read(FrameL) | !videoR.read(FrameR))
    {
        break;
    }
    Size imsize = FrameL.size();
    vector<Vec2f> foundPointsL, foundPointsR;
    bool foundL = false;
    bool foundR = false;

    //Find corners in image
    foundL = findChessboardCorners(FrameL,ChessBoardDim,
foundPointsL,CALIB_CB_ADAPTIVE_THRESH |
CALIB_CB_NORMALIZE_IMAGE); //CV_CALIB_CB_FAST_CHECK faster but
sometimes does not work as well
    foundR = findChessboardCorners(FrameR,ChessBoardDim,
foundPointsR,CALIB_CB_ADAPTIVE_THRESH |
CALIB_CB_NORMALIZE_IMAGE); //CV_CALIB_CB_FAST_CHECK faster but
sometimes does not work as well

    FrameL.copyTo(DrawToFrameL);
    FrameR.copyTo(DrawToFrameR);

    //Draw the corners to the image
    drawChessboardCorners(DrawToFrameL, ChessBoardDim,foundPointsL,foundL);
    drawChessboardCorners(DrawToFrameR, ChessBoardDim,foundPointsR,foundR);
    if (foundL & foundR)
    {
        Mat resizedL;
        Mat resizedR;
        resize(DrawToFrameL, resizedL, Size(640,480),0.0,0.0, INTER_LINEAR);
        resize(DrawToFrameR, resizedR, Size(640,480),0.0,0.0, INTER_LINEAR);
    }
}

```

```

    imshow("Left Cam", resizedL);
    imshow("Right Cam", resizedR);

    Mat tempR;
    Mat tempL;
    FrameL.copyTo(tempL);
    FrameR.copyTo(tempR);
    savedImagesL.push_back(tempL);
    savedImagesR.push_back(tempR);
    cout<<"Image "<< count <<" saved!"<<endl;
    count += 1;
}

else if (foundL & !foundR)
{
    Mat resizedL;
    Mat resizedR;
    resize(DrawToFrameL, resizedL, Size(640,480),0.0,0.0, INTER_LINEAR);
    resize(FrameR, resizedR, Size(640,480),0.0,0.0, INTER_LINEAR);

    imshow("Left Cam", resizedL);
    imshow("Right Cam", resizedR);
}

else if (foundR & !foundL)
{
    Mat resizedL;
    Mat resizedR;
    resize(FrameL, resizedL, Size(640,480),0.0,0.0, INTER_LINEAR);
    resize(DrawToFrameR, resizedR, Size(640,480),0.0,0.0, INTER_LINEAR);

    imshow("Left Cam", resizedL);
    imshow("Right Cam", resizedR);
}

else
{
    Mat resizedL;
    Mat resizedR;
    resize(FrameL, resizedL, Size(640,480),0.0,0.0, INTER_LINEAR);
    resize(FrameR, resizedR, Size(640,480),0.0,0.0, INTER_LINEAR);
}

```

```

        imshow("Left Cam",resizedL);
        imshow("Right Cam", resizedR);
    }

    char character = waitKey(100);
    if (character==33) break;

    switch (character)
    {
    case 48: //save image
        if(foundL & foundR)
        {
            Mat tempR;
            Mat tempL;
            FrameL.copyTo(tempL);
            FrameR.copyTo(tempR);
            savedImagesL.push_back(tempL);
            savedImagesR.push_back(tempR);
            cout<<"Image "<< count <<" saved!"<<endl;
            count += 1;
        }
        break;
    case 49: //start calibration
        if((savedImagesL.size()>5) & (savedImagesR.size()>5))
        {
            cout << "Starting calibration..." << endl;
            //stereoCalibration(savedImagesR,    savedImagesL,    ChessBoardDim,
calSquareDim,KR, DR, KL,DL, R, T, E,F, imsize);
            stereoCalibration(savedImagesL,    savedImagesR,    ChessBoardDim,
calSquareDim,KL, DL, KR,DR, R, T, E,F, imsize);

            saveStereoCalibration("stereoCalibMat", KL, DL, KR, DR, T, E, F, R);

            return 0;
            break;
        }
        else {cout<<"Pictures did not exceed 15"<<endl;}
        break;
    case 27: //exit

```

```

        return 0;
        break;
    }
}

cout << "Starting calibration..." << endl;
cout << savedImagesL.size() << " " << savedImagesR.size() << endl;
//stereoCalibration(savedImagesR, savedImagesL, ChessBoardDim, calSquareDim,KR,
DR, KL,DL, R, T, E,F, imsize);
stereoCalibration(savedImagesL, savedImagesR, ChessBoardDim, calSquareDim,KL,
DL, KR,DR, R, T, E,F, imsize);
saveStereoCalibration("stereoCalibMat", KL, DL, KR, DR, T, E, F, R);

return 0;
}

```

Appendix C: Spatter Tracking Code .cpp

spatterTrack.cpp

```
#include <iostream>
```

```
#include <cmath>
```

```
#include <opencv2/core/core.hpp>
```

```
#include <opencv2/imgproc.hpp>
```

```
#include "spatterTrack.hpp"
```

```
#include <opencv2/highgui.hpp>
```

```
#include <opencv2/imgcodecs.hpp>
```

```
#include <opencv2/calib3d.hpp>
```

```
#define PI 3.14159265
```

```
void spatter::cvtPoints(cv::Point2f ref)
```

```
{  
    start = cv::Point2f((start.x+ref.x),(start.y+ref.y));  
    end = cv::Point2f((end.x+ref.x),(end.y+ref.y));  
    leftW = cv::Point2f((leftW.x+ref.x),(leftW.y+ref.y));  
    rightW = cv::Point2f((rightW.x+ref.x),(rightW.y+ref.y));  
}
```

```
void spatter::drawPoints(cv::Mat& src,float size, bool showWidths)
```

```
{  
    //start points should be blue  
    //end points should be red  
    //leftmost width point should be cyan  
    //rightmost width point should be purple
```

```
    /* Note that the image may be rotated when displayed and width points colors may not  
    match this
```

```
    this color scheme. The colors should be consistant */
```

```
    cv::circle(src,start,size, cv::Scalar(255,0,0),-1);  
    cv::circle(src,end,size, cv::Scalar(0,0,255),-1);  
    if(showWidths)  
    {  
        cv::circle(src,rightW,size, cv::Scalar(255,0,255),-1);  
        cv::circle(src,leftW,size, cv::Scalar(255,255,0),-1);  
    }  
}
```

```

void spatter::computeEpipoles ( cv::Mat F, cv::Mat& startLine, cv::Mat& endLine)
{
    F.convertTo(F,CV_32FC1);
    bool print = false;

    if (print) std::cout << "Image Epilines: " << std::endl;

    cv::Mat H1,H2;
    std::vector<cv::Point2f> pnts;
    pnts.push_back(start);
    pnts.push_back(end);

    cv::Mat new_pnts[2] = {cv::Mat(pnts,CV_32FC1).reshape(1),
                          cv::Mat::ones(pnts.size(),1,CV_32FC1)};
    hconcat(new_pnts,2,H1);

    startLine = F * H1.row(0).t();
    endLine = F * H1.row(1).t();

    //These lines translate the epipoles to the correct location
    //If the cameras are not level or perhaps error in the fundamental matrix calculation
    //causes the lines to be translated from the actual position
    //the scalar multiplier is the average pixel difference between the calculated line and
    //the corresponding point

    /**/Will simply offset the lines to line up for auto matching. This will need to be fine
    tuned depending on the calibration and which image you are drawing to ***/
    startLine.at<float>(2) -= 12*startLine.at<float>(0);
    endLine.at<float>(2) -= 12*endLine.at<float>(0);

    startLine.push_back(startLine);
    endLine.push_back(endLine);

    if (print)
    {
        std::cout << "Start Line: " << std::to_string(startLine.at<float>(0))+ "x +
        "+std::to_string(startLine.at<float>(1))+ "y  "+"+std::to_string(startLine.at<float>(2))+ " =

```



```

0" << std::endl;
    std::cout << "End Line: " << std::to_string(endLine.at<float>(0))+ "x +
"+std::to_string(endLine.at<float>(1))+ "y "+std::to_string(endLine.at<float>(2))+ " = 0"
<< std::endl;
    }
}

```

```

void spatter::undistortPnts(cv::Mat K, cv::Mat D, cv::Mat Rect, cv::Mat KN, bool
printPnts)
{
    cv::Mat und, I;
    std::vector<cv::Point2f> buf;
    buf.push_back(start);
    buf.push_back(end);

    if(printPnts) std::cout << "BEFORE: " << buf << std::endl;

    cv::Mat list = cv::Mat(buf.size(),1,CV_32FC2,buf.data());
    Rect = cv::Mat::eye(Rect.rows, Rect.cols, CV_64F);
    cv::undistortPoints(list,list,K,D,Rect,KN);

    if(printPnts) std::cout << "UNDISTORTED: " << list << std::endl;

    start= cv::Point2f(list.at<float>(0,0),list.at<float>(0,1));
    end = cv::Point2f(list.at<float>(1,0),list.at<float>(1,1));

}

```

```

void meltpool::undistortMelt(cv::Mat K, cv::Mat D, cv::Mat Rect, cv::Mat KN, bool
printPnts)
{
    std::vector<cv::Point2f> melt;
    melt.push_back(loc);
    cv::Mat uMelt(melt,CV_64FC2);
    if(printPnts) std::cout << "MELTPOOL BEFORE: " << uMelt << std::endl;

    //Rect = cv::Mat::eye(Rect.rows, Rect.cols, CV_64F);
    cv::undistortPoints(uMelt,uMelt,K,D,Rect,KN);

```

```

if(printPnts) std::cout << "MELTPOOL UDISTORTED: " << uMelt << std::endl;
loc = cv::Point2f(uMelt.at<float>(0,0), uMelt.at<float>(0,1));

}

void spatter::setMagnitude()
{
    double ret;
    ret = sqrt((start.x - end.x)*(start.x-end.x) + (start.y-end.y)*(start.y-end.y));
    mag = ret;
}

void spatter::setAngle(cv::Point2f melt)
{
    cv::Point2f bufPnt = cv::Point2f(start.x-melt.x, (start.y-melt.y)*-1.0);
    //cout << "Origin: " << origin << " Original Pnt: " << pnt << " Pnt: " << bufPnt << endl;
    if (start.x == 0)
    {
        if (bufPnt.y < 0)
        {
            angle = -90;
        }
        else { angle = 90;}
    }
    if(bufPnt.y == 0)
    if (bufPnt.x < 0 )
    {
        angle = -180;
    }
    else { angle = 0;}
    else
    {

        if (bufPnt.x > 0 && bufPnt.y > 0)
            angle = atan(bufPnt.y/bufPnt.x) * 180/ PI;
        else if (bufPnt.x < 0 && bufPnt.y > 0)
            angle = (PI + atan(bufPnt.y/bufPnt.x)) * 180/ PI;
        else if (bufPnt.x < 0 && bufPnt.y < 0)
            angle = (PI + atan(bufPnt.y/bufPnt.x)) * 180/ PI;
    }
}

```

```

    else
        angle = (2*PI + atan(bufPnt.y/bufPnt.x)) * 180/ PI;
    }
}

float meltpool3D::velocity()
{
    float vel;
    vel = sqrt((x - lastx)*(x-lastx) + (y - lasty)*(y - lasty) + (z - lastz)*(z - lastz));
    return vel;
}

void meltpool3D::setLastLocation()
{
    lastx = x;
    lasty = y;
    lastz = z;
}

float spatter3D::Age(meltpool3D melt)
{
    float age;
    age = sqrt((sx - melt.x)*(sx-melt.x) + (sy - melt.y)*(sy - melt.y) + (sz - melt.z)*(sz -
melt.z));
    return age;
}

float spatter3D::Magnitude()
{
    float mag;
    mag = sqrt((sx - ex)*(sx-ex) + (sy - ey)*(sy - ey) + (sz - ez)*(sz - ez));
    return mag;
}

```

Appendix D: Spatter Tracking Code .hpp

spatterTrack.hpp

```
#ifndef SPATTERTRACK_HPP
```

```
#define SPATTERTRACK_HPP
```

```
#include <iostream>
```

```
#include <opencv2/core/core.hpp>
```

```
class spatter;
```

```
class meltpool;
```

```
void cvtPoints(cv::Point2f ref);
```

```
void drawPoints(cv::Mat& src,float size, bool showWidths);
```

```
class meltpool
```

```
{
```

```
public:
```

```
    cv::Point2f loc;
```

```
    std::vector<cv::Point> contour;
```

```
    cv::Point2f temp;
```

```
    meltpool()
```

```
    {}
```

```
    meltpool(cv::Point2f loc):
```

```
        loc(loc)
```

```
    {
```

```
    }
```

```
    void undistortMelt(cv::Mat K, cv::Mat D, cv::Mat Rect, cv::Mat KN, bool printPnts);
```

```
    meltpool(cv::Point2f loc, std::vector<cv::Point> contour):
```

```
        loc(loc),contour(contour)
```

```
    {
```

```
    }
```

```
};
```

```
class spatter
```

```

{

public:
    void cvtPoints(cv::Point2f ref);
    void drawPoints(cv::Mat& src, float size, bool showWidths);
    void computeEpipoles ( cv::Mat F, cv::Mat& start_lines, cv::Mat& end_lines);
    void undistortPnts(cv::Mat K, cv::Mat D, cv::Mat Rect, cv::Mat KN, bool printPnts);
    void setAngle(cv::Point2f melt); //sets the angle of the start point with row containing
    meltpool as x axis
    void setMagnitude();//sets the 2D magnitude

    cv::Point2f start;
    cv::Point2f end;
    cv::Point2f leftW;
    cv::Point2f rightW;
    double mag;
    float angle;
    std::vector<cv::Point> contour;

    spatter(cv::Point2f start, cv::Point2f end, std::vector<cv::Point> contour):
    start(start), end(end), contour(contour)
    {
    }

    spatter(cv::Point2f start, cv::Point2f end, cv::Point2f leftW, cv::Point2f rightW ):
    start(start), end(end), leftW(leftW), rightW(rightW)
    {
    }

};

class meltpool3D
{
public:

    void setLastLocation();
    float velocity();

    float x;
    float y;

```

```

float z;
float lastx;
float lasty;
float lastz;

melpool3D()
{
}
melpool3D(float x, float y, float z):
    x(x), y(y), z(z)
{
}

};

class spatter3D
{
public:

    float Age(melpool3D melt);
    float Magnitude();

    //start and end points in 3D space
    float sx, ex;
    float sy, ey;
    float sz, ez;

    spatter3D()
    {
    }

    spatter3D(float sx, float sy, float sz, float ex, float ey, float ez):
        sx(sx), sy(sy), sz(sz), ex(ex), ey(ey), ez(ez)
    {
    }

};

#endif

```


Appendix E: Matlab Code For Analyzing .cpp Output

plotframes.m

```
clear;
clc;
format long

frame_numba = []; %frame numbers
centroid_loc = []; %centroid location ~ len(centroid) = len(frameNumba) ~
cntsPfrme = [];
starts = []; %start points for selected spatter
ends = []; %end points for selected spatter
widths = []; %width points for selected spatter
p = 100;
ages = [];
widths_mag = [];
lengths_mag = [];

infile = fopen('Al_60_370_1120_110.txt','r');
text = textscan(infile,'%s','Delimiter','\n');
n = length(text{1});

%Load data from txt file
for n = [1:1:n]

    buf = cell2mat(text{1}(n));
    buf = strsplit(buf,':');

    if length(buf) == 2
        p = 0;
        frme = cell2mat(buf(2));
        frme = strsplit(frme,',' );
        frame_numba = [frame_numba; str2num(frme{1})];
        cnts = str2num(frme{2});
        cntsPfrme = [cntsPfrme; cnts];
        continue;
    else
        buffer = strsplit(cell2mat(text{1}(n)),',');
        buf=zeros(size(buffer));
        buf=str2double(buffer);
    end
end
```



```

if p == 0
    centroid_loc = [centroid_loc; [buf]];
    p = p + 1;
    continue;
end

if p == 1
    track = str2num(cell2mat(text{1}(n)));
    p = p + 1;
    continue;
end

if (p == 2 | p == 3)
    widths = [widths; buf];
    p = p + 1;
    continue;
end

if (p == 4)
    starts = [starts; [buf]];
    p = p + 1;
    continue;
end

if (p == 5)
    ends = [ends; [buf]];
    p = p + 1;
    continue;
end

if (p == 6)
    ages = [ages; buf(1)];
    %widths_mag = [widths_mag; buf(2)];
    %lengths_mag = [lengths_mag; buf(3)];
    p = p+1;
end

if (p == 7)
    track = str2num(cell2mat(text{1}(n)));
end

```

```

if (track <= cnts)
    p = 2;
    n = n + 1;
end

end

Origin = [mean(centroid_loc(:,1)) mean(centroid_loc(:,2)) mean(centroid_loc(:,3))];
%%Average centroid location
vecs = ends - starts;
mags_old = [];

%Check Magnitudes
for i = 1:1:length(vecs)
    mags_old(i) = sqrt((vecs(i,1)^2) + (vecs(i,2)^2) + (vecs(i,3)^2));
    %fprintf('Imported Magnitudes of Vector(%d): %0.6f\n',i,mags_old(i));
end

% Shift average of centroids to origin for plane fitting at z = 0
%New variable is not used in plotting ~ only plane fitting
centroids = [];
for i = 1:1:length(centroid_loc(:,1))
    centroids(i,:) = centroid_loc(i,:) - Origin;
end

%Change vector of centroids the same size as starts & ends
cents = [];
for i = 1:1:length(centroids)
    for p = 1:1:cntsPfrme(i)
        cents = [cents; centroids(i,:)];
    end
end

%Translate each vector according to new origin
for i = 1:1:length(starts)
    starts(i,:) = starts(i,:) - Origin;
    ends(i,:) = ends(i,:) - Origin;
end

```

```

%Fit Plane to centroid locations
A = [centroids(:,1),centroids(:,2),ones(size(centroids(:,1)))];
res = A\centroids(:,3);
a = res(1);
b = res(2);
c = res(3);
[X, Y] = meshgrid(-0.10:0.01:0.10);
Z = a.*X + b.*Y + c;

%Find gravity~normal to plane
v1 = [X(1) Y(1) Z(1)];
v2 = [X(100) Y(100) Z(100)];
grav = cross(v1,v2);
g = -1.*[grav(1) grav(2) grav(3)] ./ (sqrt(grav(1)^2 + grav(2)^2 + grav(3)^2)); %%Gravity
Unit vector
x = [v1(1) v1(2) v1(3)]./ sqrt(v1(1)^2 + v1(2)^2 + v1(3)^2);
y = cross(g,x);
y = [y(1) y(2) y(3)]./ sqrt(y(1)^2 + y(2)^2 + y(3)^2);
theta = -asin(g(2)/sqrt(g(3)^2 + g(2)^2))
rotation_1 = [1 0 0; 0 cos(theta) sin(theta); 0 -sin(theta) cos(theta)];
g = rotation_1*g';
x = rotation_1*x';
y = rotation_1*y';
theta2 = -asin(g(1)/sqrt(g(1)^2 + g(3)^2));
rotation_2 = [cos(theta2) 0 sin(theta2); 0 1 0; -sin(theta2) 0 cos(theta2)];
g = rotation_2*g';
x = rotation_2*x';
y = rotation_2*y';
rot = rotation_2*rotation_1;
rot = [-1 0 0; 0 1 0; 0 0 -1]*rot;

Xp = ones(size(X));
Yp = ones(size(Y));
Zp = ones(size(Z));

% Calculate rotated plane point coordinates (All should have Z=0)
for q = 1:1:length(X(:,1))
    for p = 1:1:length(X(1,:))
        X_buf = X(q,p);
        Y_buf = Y(q,p);

```

```

    z_buf = Z(q,p);
    Xp(q,p) = (rot(1,:)*[X_buf Y_buf z_buf]);
    Yp(q,p) = (rot(2,:)*[X_buf Y_buf z_buf]);
    Zp(q,p) = (rot(3,:)*[X_buf Y_buf z_buf]);
end
end

%Rotate centroids and start and end points
mags_new = [];
for i = 1:1:length(cents(:,1))
    cents(i,:) = transpose(rot*transpose(cents(i,:)));
end

for i = 1:1:length(ends(:,1))
    ends(i,:) = transpose(rot*transpose(ends(i,:)));
    starts(i,:) = transpose(rot*transpose(starts(i,:)));
end

prop = input('Plot all frames (y/n)','s')

if prop == 'y'

    %Shift each vector according to appropriate centroid location
    starts = starts - cents;
    ends = ends - cents;
    vecs = ends - starts;
    cents = cents - cents;

    %Just checking that the vectors aren't scaled during rotation
    for i = 1:1:length(vecs)
        mags_new(i) = sqrt((vecs(i,1)^2) + (vecs(i,2)^2) + (vecs(i,3)^2));
        %fprintf('Rotated Magnitude of Vector(%d): %0.6f\n',i,mags_new(i));
    end

    ages = starts - cents;

    for i = 1:1:length(ages)
        mags_ages(i) = sqrt((vecs(i,1)^2) + (vecs(i,2)^2) + (vecs(i,3)^2));
    end
end
else

```

```

fprintf('Melpool centroid of first frame will be used as origin \n')
startFrame = input('Enter first frame to plot: \n')
endFrame = input('Enter last frame to plot: \n')
startCnt = sum(cntsPfrme(1:startFrame));
endCnt = startCnt+sum(cntsPfrme(startFrame:endFrame));

%Shift each vector according to appropriate centroid location
for q = startCnt:1:endCnt
    starts(q,:) = starts(q,:) - cents(startCnt,:);
    ends(q,:) = ends(q,:) - cents(startCnt,:);
    vecs(q,:) = ends(q,:) - starts(q,:);
    cents(q,:) = cents(q,:) - cents(q,:);
end
for i = 1:1:length(vecs)
    mags_new(i) = sqrt((vecs(i,1)^2) + (vecs(i,2)^2) + (vecs(i,3)^2));
    %fprintf('Rotated Magnitude of Vector(%d): %0.6f\n',i,mags_new(i));
end

ages = starts - cents;

for i = 1:1:length(ages)
    mags_ages(i) = sqrt((vecs(i,1)^2) + (vecs(i,2)^2) + (vecs(i,3)^2));
    %fprintf('Rotated Magnitude of Vector(%d): %0.6f\n',i,mags_new(i));
end
end
if prop == 'y'

new_cents = [];
new_vecs = [];
new_ages = [];
new_starts = [];

for i = 1:1:length(cents)
    if starts(i,3) >=0 && ends(i,3) >=0
        new_cents = [new_cents; cents(i,:)];
        new_vecs = [new_vecs; vecs(i,:)];
        new_ages = [new_ages; ages(i,:)];
        new_starts = [new_starts; starts(i,:)];
    end
end
end

```

```

else
    %When true this condition plots a few selected frames selecting the
    %first centroid location as the origin

    new_cents = [];
    new_vecs = [];
    new_ages = [];
    new_starts = [];

    for i = 1:length(cents(startCnt:endCnt,1))
        if starts(i,3) >=0 && ends(i,3) >=0
            new_cents = [new_cents; cents(startCnt,:)];
            new_vecs = [new_vecs; vecs(startCnt:endCnt,:)];
            new_ages = [new_ages; ages(startCnt:endCnt,:)];
            new_starts = [new_starts; starts(startCnt:endCnt,:)];
        end
    end

    %Just trying to pair vectors with likely the same vector in the subsequent
    %frames
    %unitVecs = [];
    %initialVectors = [];
    %for v = 0:1:cntsPfrme(startFrame)-1
    %    initialVectors = [initialVectors;[vecs(startCnt+v,:)]];
    %    unitVecs = [unitVecs;[vecs(startCnt+v,:).*(1/mags_new(startCnt+v))]];
    %end

end

figure(1)
clf
%plot3(X,Y,Z,'k+','markersize',5)
%hold on
%mesh(X,Y,Z)
%hold on
datacursormode on

```

```

plot3(new_cents(:,1),new_cents(:,2),new_cents(:,3),'r+','markersize',5)
hold on
plot3(new_cents(:,1),new_cents(:,2),new_cents(:,3),'r.','markersize',5)
hold on
%plot3(0,0,0,'r+','markersize',5)
%hold on
%plot3(0,0,0,'r.','markersize',5)
hold on
axis equal
mesh(Xp,Yp,Zp)
hold on
%quiver3(Xp ,Yp ,Zp ,U ,V ,W);
%hold on
zzz =
quiver3(new_starts(:,1),new_starts(:,2),new_starts(:,3),new_vecs(:,1),new_vecs(:,2),new_
vecs(:,3));
title('Spatter Tracker', 'FontSize',14,'FontWeight','bold')
set(zzz,'LineWidth',1)
xlabel('X (m)', 'FontSize',14,'FontWeight','bold')
ylabel('Y (m)', 'FontSize',14,'FontWeight','bold')
zlabel('Z (m)', 'FontSize',14,'FontWeight','bold')
xlim([-0.02 0.01])
set(gca,'FontSize',14,'FontWeight','bold')
ylim([-0.01 0.02])
zlim([-0.00 0.015])
grid on

```